

# Portable Low-Cost Magnetic Resonance Imaging

by

Clarissa Zimmerman Cooley

Submitted to the Department of Electrical Engineering and Computer  
Science

in partial fulfillment of the requirements for the degree of

Doctor of Philosophy

at the

MASSACHUSETTS INSTITUTE OF TECHNOLOGY

September 2014

© Massachusetts Institute of Technology 2014. All rights reserved.

Author .....  
Department of Electrical Engineering and Computer Science  
August 29, 2014

Certified by.....  
Lawrence L. Wald  
Associate Professor of Radiology, Harvard Medical School  
Thesis Supervisor

Accepted by.....  
Leslie A. Kolodziej  
Chairman, Department Committee on Graduate Theses



# Portable Low-Cost Magnetic Resonance Imaging

by

Clarissa Zimmerman Cooley

Submitted to the Department of Electrical Engineering and Computer Science  
on August 29, 2014, in partial fulfillment of the  
requirements for the degree of  
Doctor of Philosophy

## Abstract

**Purpose:** As the premiere modality for brain imaging, MRI could find wider applicability if lightweight, portable systems were available for siting in unconventional locations such as intensive care units (ICUs), physician offices, surgical suites, ambulances, emergency rooms, sports facilities, or rural healthcare sites.

**Methods:** A truly portable (<100kg) proof-of-concept MRI scanner has been constructed and validated, which replaces conventional gradient encoding with a rotating lightweight, cryogen-free, low-field magnet. When rotated about the object, an inhomogeneous magnetic field pattern is used as a rotating Spatial Encoding Magnetic field (rSEM) to create generalized projections and encode the iteratively reconstructed 2D images. Multiple receive channels are used to disambiguate the non-bijective encoding field.

**Results:** The system is validated with experimental images of 2D test phantoms. Similar to other non-linear field encoding schemes, the spatial resolution is position dependent with blurring in the center, but this will be improved with modifications to the magnet design.

**Conclusion:** This novel MRI scanner demonstrates the potential for portability by simultaneously relaxing the magnet homogeneity criteria and eliminating gradient coils. This new architecture and encoding scheme shows convincing proof of concept images that are expected to be further improved with refinement of the calibration and methodology.

Thesis Supervisor: Lawrence L. Wald

Title: Associate Professor of Radiology, Harvard Medical School



# Acknowledgments

The work presented here was made possible with the help and support of many.

I would like to acknowledge the support of this project from the DOD (W81XWH-11-2-0076 (DM09094)), and my personal support through the NIH Advanced Multimodal Neuroimaging Training Program and NIH Speech & Hearing Bioscience and Technology Training Program.

I want to thank my thesis adviser, Prof. Lawrence Wald, for envisioning such a great project, and giving me the opportunity to work on it. I am grateful to have an adviser who cares so much about my work, and is always available to give advice.

I was fortunate to have an extremely supportive and enthusiastic thesis committee. I want to thank Prof. Matthew Rosen for always being so positive and encouraging, and for all his contributions to this work. I want to thank Prof. Elfar Adalsteinsson for connecting me with the Martinos center, and providing me with great advice on navigating the course of my PhD. I also want to thank Prof. Jacob White for his valuable input and genuine interest in the Halbach scanner and in the educational MRI scanners. I look forward to collaborating more in the future.

I thank the staff of 6.S02 for giving me the chance to TA and contribute to the formation of the course. The development and construction of the educational MRI scanners was an enriching side-project that allowed me to extend the breadth of my PhD work.

I want to thank all of my colleagues at the Martinos Center, many of whom contributed to this work in some way. I specifically want to acknowledge Dr. Jason Stockmann, who has made significant contributions to this work and has become a great friend. To all of my friends in the Wald Lab and the Low-Field Lab, our time spent together has been such an enjoyable and important part of my graduate experience.

I want to thank my family, for supporting my journey to MIT from South Texas 10 years ago. Without your love and encouragement, I would not be here. Finally, I want thank my husband and best friend, John, for everything.

Clarissa Zimmerman Cooley

Massachusetts Institute of Technology

August, 2014



# Contents

<b>1</b>	<b>Introduction</b>	<b>17</b>
1.1	Portable MRI for clinical applications . . . . .	17
1.2	Outline and Bibliographical notes . . . . .	20
1.2.1	Chapter 2 . . . . .	20
1.2.2	Chapter 3 . . . . .	20
1.2.3	Chapter 4 . . . . .	21
1.2.4	Chapter 5 . . . . .	21
1.2.5	Chapter 6 . . . . .	21
1.2.6	Chapter 7 . . . . .	22
1.2.7	Chapter 8 . . . . .	22
1.2.8	Chapter 9 . . . . .	22
<b>2</b>	<b>Background</b>	<b>23</b>
2.1	General MRI background . . . . .	23
2.1.1	Excitation . . . . .	24
2.1.2	Acquisition . . . . .	24
2.1.3	Image Encoding . . . . .	25
2.2	Conventional MRI . . . . .	25
2.2.1	Basic Hardware Components . . . . .	25
2.2.2	Fourier Imaging: non-ideal for portable human scanning . . . . .	27
2.3	Previous Work in Portable NMR/MRI . . . . .	28
2.4	Introduction to the rSEM encoding method . . . . .	30

<b>3</b>	<b>Magnet - Polarizing and Encoding fields</b>	<b>33</b>
3.1	Magnet Design Considerations . . . . .	33
3.2	Background - Permanent Magnets in MR . . . . .	37
3.2.1	Halbach magnets for portable NMR . . . . .	41
3.3	Magnet Design (version 1) . . . . .	42
3.3.1	$y - z$ plane . . . . .	43
3.3.2	$x$ profile . . . . .	43
3.4	Magnet Hardware and Construction . . . . .	48
3.4.1	Force simulations . . . . .	49
3.4.2	Magnet Housing . . . . .	50
3.4.3	Magnet Population . . . . .	50
3.4.4	Rotation Hardware . . . . .	51
3.4.5	Results . . . . .	51
3.5	Gaussmeter Map and Shimming . . . . .	51
3.6	Field Mapping - Field Probe Arrays . . . . .	53
3.6.1	Background . . . . .	53
3.6.2	2D Field Probe Array . . . . .	55
3.6.3	3D Field Probe Array . . . . .	56
3.6.4	Field Drift Tracking . . . . .	58
<b>4</b>	<b>2D Data Acquisition and RF Coils</b>	<b>61</b>
4.1	Overview . . . . .	61
4.2	Pulse Sequences . . . . .	62
4.3	Excitation Method . . . . .	65
4.3.1	Broadband Excitation . . . . .	65
4.3.2	Excitation Coil . . . . .	66
4.4	Rx Coil Array . . . . .	67
4.4.1	Coil sensitivity profiles . . . . .	68
4.4.2	Rotating Rx coils . . . . .	70
4.5	RF Coil Decoupling and Switching . . . . .	72

4.5.1	Theory . . . . .	72
4.5.2	Implementation . . . . .	73
<b>5</b>	<b>Image Reconstruction</b>	<b>75</b>
5.1	Signal Equation . . . . .	75
5.2	Encoding Matrix Calibration . . . . .	78
5.2.1	Coil sensitivity weighting . . . . .	78
5.2.2	SEM induced phase . . . . .	78
5.3	Iterative Reconstruction Methods . . . . .	80
5.3.1	Conjugate Gradients . . . . .	81
5.3.2	Algebraic Reconstruction Technique - Kaczmarz method . . . . .	82
5.4	Results: 2D Images . . . . .	83
5.4.1	Single Coil Image . . . . .	84
5.4.2	Multi-coil Images . . . . .	84
5.4.3	Discussion . . . . .	87
<b>6</b>	<b>Spatial Resolution in rSEM</b>	<b>91</b>
6.1	Simulation Method . . . . .	91
6.2	Simulation Results . . . . .	94
6.3	Discussion . . . . .	96
6.4	Conclusion . . . . .	100
<b>7</b>	<b>Potential 3rd Dimension Encoding Methods</b>	<b>103</b>
7.1	Bloch Siegert Spatial Encoding Technique - BS-SET . . . . .	104
7.1.1	Theory . . . . .	104
7.1.2	Pulse Sequence . . . . .	106
7.1.3	Experiment . . . . .	107
7.1.4	Future Direction . . . . .	109
7.2	TRansmit Array Spatial Encoding - TRASE . . . . .	111
7.2.1	Theory . . . . .	111
7.2.2	Pulse sequence . . . . .	112

7.2.3	TRASE coils . . . . .	113
7.2.4	Future Direction . . . . .	114
7.3	Conclusion . . . . .	115
<b>8</b>	<b>Future Directions and Conclusion</b>	<b>117</b>
8.1	Summary of Work . . . . .	117
8.2	Future Directions . . . . .	119
8.2.1	3D encoding . . . . .	119
8.2.2	Halbach Magnet - version 2 . . . . .	119
8.2.3	Patient table design . . . . .	122
8.2.4	Parallel imaging . . . . .	123
8.3	Conclusion . . . . .	123
<b>9</b>	<b>Implementation of low-cost, instructional tabletop MRI scanners</b>	<b>125</b>
9.1	Introduction . . . . .	125
9.1.1	Overview of Scanner . . . . .	126
9.2	Magnet - $B_0$ field . . . . .	127
9.3	Console . . . . .	127
9.4	Gradients - $G_x, G_y, G_z$ . . . . .	129
9.4.1	Gradient Power Amplifiers . . . . .	130
9.4.2	Gradient Filters . . . . .	131
9.4.3	Gradient coils . . . . .	132
9.5	RF Subsystems . . . . .	133
9.5.1	RF coil . . . . .	134
9.5.2	Transmit pulses . . . . .	134
9.5.3	T/R switch and Pre-amplifier . . . . .	135
9.6	Graphical User Interfaces (GUIs) and Lab Exercises . . . . .	136
9.7	Alternative Magnet Design . . . . .	141

# List of Figures

2-1	NMR precession and relaxation . . . . .	24
2-2	Lauterbur's projection imaging figure from Ref. [1] . . . . .	30
3-1	Anatomical benchmarks for human brain imaging. . . . .	37
3-2	Summary of popular yoked permanent magnet design from Ref. [2] . . . . .	38
3-3	Drawing of a dipolar Halbach cylinder showing polarization orientations. . . . .	39
3-4	Magnetic flux density simulations for three sparse dipolar Halbach cylinder designs with different array diameters. . . . .	44
3-5	Magnetic flux density simulations for three Halbach cylinders with the same diameter but different designs along the length of the cylinder. . . . .	46
3-6	Magnetic field profile along the axis of the cylinder for five designs. . . . .	47
3-7	CAD drawing of Halbach magnet design, field simulations, and photo of the constructed magnet. . . . .	48
3-8	Simulated radial forces on the magnet rungs in the Halbach cylinder and photo of magnet construction process. . . . .	49
3-9	Initial magnet field mapping process and resulting field maps. . . . .	52
3-10	Illustration of the magnet shimming method . . . . .	54
3-11	Shimmed field maps in three planes. . . . .	55
3-12	NMR field probe array for quickly acquiring 2D field maps and resulting field map. . . . .	56
3-13	Field probe array for 3D field mapping and resulting field maps. . . . .	57
3-14	Larmour frequency drift with temperature plotted over 12 hrs. . . . .	59

4-1	Schematic depiction of the generalized projections acquired with the rotating Spatial Encoding Magnetic field (rSEM) method. . . . .	62
4-2	Tecmag Apollo console, Tomco RF power amplifier, and TNMR software screenshot. . . . .	64
4-3	Basic pulse sequence for the rSEM imaging method. . . . .	64
4-4	Photos of the Tx solenoid coil and the Rx coil array. . . . .	67
4-5	Calculated receive coil sensitivity maps. . . . .	69
4-6	Simulated images comparing the performance of rotating and stationary receiver coil arrays in the rotating Halbach magnet. . . . .	71
4-7	Schematic of the surface coil circuit. . . . .	73
5-1	Visual representation of the matrix form of the signal equation. . . .	77
5-2	Experimental offset frequencies tracked with the “field tracking” NMR probe. . . . .	79
5-3	Conjugate gradient reconstruction of a lemon slice. . . . .	82
5-4	Experimental 2D image of an “MGH” water-filled phantom, acquired with a solenoid in Tx/Rx mode. . . . .	85
5-5	Experimental 2D image of an “MIT-MGH” phantom acquired with the Rx coil array. . . . .	86
5-6	Experimental 2D image of 1 cm lemon slice acquired with the Rx coil array. . . . .	87
6-1	Rotating Spatial Encoding Magnetic Fields (rSEMs) used in simulations.	92
6-2	Simulation objects: 1) line of point sources, 2) brain image. . . . .	93
6-3	Simulated 2D image of a line of points starting at center of FOV (spaced 5 mm apart) using multiple rotating SEMs. . . . .	94
6-4	Simulated 1D image of a line of points starting at center of FOV (spaced 5 mm apart) using multiple rotating SEMs. . . . .	95

6-5	Simulated 1D image of a line of points starting at center of FOV (spaced 5 mm apart) using the measure Halbach SEM for rSEM encoding, and the coil sensitivities of the solenoid (assumed to be uniform) and 8 channel receive array. . . . .	96
6-6	FWHM of simulated point spread functions. . . . .	97
6-7	Simulated brain images from the four SEM shapes. . . . .	98
6-8	Plot of the average gradient field seen throughout the 2D FOV for the typical pulse sequence. . . . .	99
6-9	The spatially varying voxel size was estimated using the average gradient fields in Figure 6-8. . . . .	100
7-1	2D and 3D encoding in Halbach magnet. . . . .	103
7-2	Illustration of the Bloch Siegert Encoding technique (BS-SET). . . . .	106
7-3	Schematic of BS-SET experiment and resulting 1D images. . . . .	108
7-4	Calibration data for the Bloch-Siegert coil. . . . .	109
7-5	Proposed RARE-type BS-SET pulse sequence. . . . .	110
7-6	The Transmit Array Spatial Encoding (TRASE) method is illustrated . . . . .	112
7-7	Field simulations and photo of constructed TRASE coils. . . . .	114
8-1	Halbach magnet designs with larger bores. . . . .	121
8-2	CAD drawing of a prototype scanner assembly with separate scanner cart and patient table. . . . .	122
8-3	CAD drawing of initial receive array helmet design. . . . .	124
9-1	Complete instructional MRI scanner. . . . .	126
9-2	$B_0$ magnet for instructional scanners. . . . .	128
9-3	Medusa console. . . . .	129
9-4	Gradient power amplifier (GPA) schematic. . . . .	130
9-5	Gradient power amplifier (GPA) chassis. . . . .	131
9-6	Gradient filters. . . . .	132
9-7	Shielded planar gradient coils. . . . .	133

9-8	Block diagram of RF subsystem. . . . .	133
9-9	Photo of RF coil and samples. . . . .	134
9-10	Power-blanking circuit for the RF power amplifier. . . . .	135
9-11	Schematic and board layout of combined T/R switch and pre-amplifier circuit. . . . .	137
9-12	Free induction decay (FID) GUI. . . . .	138
9-13	Spin-echo GUI. . . . .	139
9-14	Spin-echo GUI in projection imaging mode. . . . .	140
9-15	3D spin echo pulse sequence. . . . .	140
9-16	3D imaging GUI . . . . .	141
9-17	Experimental 3D images of “M-I-T” phantom and a mouse brain. . .	142
9-18	Alternative Halbach magnet design. . . . .	142

# List of Tables

3.1	Calculated polynomial coefficients composing the $z-y$ plane (2D imaging plane) of the Halbach spatial encoding field in Hz/cm $^{m+n}$ . Measured points from the linear array of field probes (Figure 3-12) were used for this sixth order polynomial fit. . . . .	57
-----	--	----



# Chapter 1

## Introduction

### 1.1 Portable MRI for clinical applications

The accessibility and benefits of Magnetic Resonance Imaging (MRI) are severely limited by the infrastructure requirements and cost of MRI scanners. Conventional high field MRI scanners have found a stable clinical neuroimaging market for diagnostic imaging related to headaches, tumors, stroke, seizures, etc., but the use of MRI could be greatly expanded if low-cost portable scanners were available. Specialized, portable MRI systems have the potential to make MR imaging possible at sites where it is currently unavailable and enable immediate, “point-of-care” detection and diagnosis of acute, subacute, and chronic intracranial pathology which can be critical in patient management.

The use of Computed Tomography (CT) scanners has increased dramatically in the last 15 years [3], [4] due to their relatively low-cost and short scan time. In recent years, portable CT scanners have been gaining popularity [5]. Neurologica Corp. has developed several portable CT models which are battery powered and can easily be transported room to room in hospitals and can be used in operating rooms, emergency departments, neurology offices, or patient’s rooms. They have also been integrated into specialized ambulances for mobile stroke treatment that are currently in use in Berlin, Cleveland, and Houston. The growing popularity of these portable CT scanners indicates the demand for mobile, low-cost imaging.

The increase in CT imaging has led to heightened awareness about the associated risks from the radiation dosage [6]. There is convincing evidence that radiation doses from CT scans increase the risk of cancer [7]. These risks are elevated in children because of the higher proportion of dividing cells lead to a higher risk of DNA damage, making children up to 10 times more radiosensitive [8]. Additionally, for children exposed to CT radiation there are more potential years of life to develop cancer. A recent retrospective study [9], reports that multiple CT scans in children tripled the risk of brain tumors and almost quadrupled the risk of leukemia [9]<sup>1</sup>. Repeated CT scanning is only cautiously done on children when it is determined that the benefit outweighs the risk. In most cases MRI scanning could be done instead and is usually more sensitive, but it often not possible because of the lack of availability. The availability of low-cost, easy-to-site MRI scanners could disrupt this paradigm.

Portable, low-cost scanners are compelling for applications where power, siting and cost constraints have limited conventional scanners. Examples include clinics in rural or underdeveloped areas, military field hospitals, sports arenas, and ambulances. Specialized low-cost scanners could impact global health. For example, hydrocephalus is a condition in which cerebrospinal fluid (CSF) builds up in the skull and causes pressure on the brain. The CURE organization estimates that 79% of infants born with hydrocephalus are in the developing world, where it is much more prominent due to the increased prevalence of infections. Hydrocephalus is easily detectable with even crude non-invasive imaging, but MRI scanners are typically unavailable in the developing world. The CURE children's hospital in Uganda specializes in the detection and treatment of Hydrocephalus in children, but there are currently no MRI scanners in Uganda so CT brain imaging is performed. As described previously, the use of CT imaging in children is undesirable, and the CURE children's hospital is eager to obtain a low-cost, easy to cite MRI alternative. A low-cost portable MR-based neuroimaging scanner would be valuable for characterizing acute hydrocephalus cases and monitoring treatment methods, e.g. shunt-placement.

The largest application space for a low-cost portable neuroimaging scanner could

---

<sup>1</sup>Even though the risk is significantly increased, it is still very low

be traumatic brain injury (TBI) imaging. TBI from explosions have become known as the signature wound from wars in Iraq and Afghanistan [10] in recent years, and there is an obvious interest for easy-to-site brain scanners in military field hospitals. There is also a need for low-cost TBI imaging tools in rural clinics throughout the United States as there are approximately 50,000 TBI-related deaths per year in the U.S. [8]. Among children, there are an estimated 435,000 TBI related emergency department visits per year. Imaging may allow early diagnosis and determine the severity and operability of the problem [11]. Imaging is also essential for surgical planning. MRI is generally more sensitive and a more accurate means of identifying TBI pathology such as contusions, shearing, and subdural/epidural hematomas. Unfortunately, CT imaging is usually chosen over MRI in the acute setting for adults and children because CT is more available, convenient, and cost-effective [12].

Determining the presence of a brain hemorrhage following a stroke is an extremely time-sensitive matter which determines the flow of treatment. The first question that must be answered for a stroke is: is there a bleed or not? If the answer is no, a thrombolytic drug, tissue plasminogen activator (tPA), is immediately mixed and administered, which breaks down clots and restores the blood flow in the brain. This question is typically answered with a non-contrast CT image, and then a series of other test are performed to determine further action including a CT angiogram or MR angiogram and an MRI diffusion weighted image (DWI) [13]. Although it is questionable if the low-field MRI system described in this thesis will be capable of DWI, the determination of a hemorrhage should be obtainable.

Patients in intensive care units (ICUs) could often benefit from follow-up imaging. For example, following a neurosurgical procedure, non-invasive imaging could be used to monitor for postoperative complications such as cerebral edema, cerebral infarction, pneumocephalus, and hematomas (which occur in 2% of patients undergoing cranial procedures) [14]. In these intensive care settings, MRI scanners are generally nearby, but they are difficult to utilize because of the dangers associated with transporting critical care patients. In these case, a low-field bed-side MRI scanner could offer major benefits.

Finally, analogous to the current use of ultra-sound, a low-cost and easy-to-use scanner could find uses in neurology, neurosurgery or neuro-oncology examination rooms for routine disease monitoring (e.g. monitoring ventricle size after shunt placement). This would allow rapid “point-of-care” assessment instead of scheduling an MRI scan in a conventional scanner and waiting for results.

The development of a low-cost portable MRI scanner for human brain imaging relies on the co-design of a new image encoding method and simplified hardware. This approach is the focus of this thesis work.

## **1.2 Outline and Bibliographical notes**

The structure of this dissertation along with an associated publication is as follows:

### **1.2.1 Chapter 2**

Chapter 2 provides background information on conventional MRI hardware and Fourier imaging to motivate the re-envisioning of the hardware and encoding method presented in this thesis. Background is presented on previous work towards portable MRI in the literature. The basic encoding method used for our scanner is then introduced and background on previous relevant work that inspired the encoding method is presented.

### **1.2.2 Chapter 3**

Chapter 3 focuses on the portable scanner’s magnet, a sparse dipolar Halbach cylinder. A 45 kg rotating permanent magnet with a built-in image encoding field is used for projection imaging. The design and construction process is detailed in this chapter. Additionally, the field mapping and field tracking methods are described, which are both critical to image reconstruction.

The work was initially presented in Ref. [15]

### 1.2.3 Chapter 4

Chapter 4 details our 2D image acquisition method, a generalization of the classic projection imaging method introduced by Lauterbraur in 1973 [1]. The encoding field is rotated in relation to the object, and projections of the object onto the encoding field are acquired. The encoding field of our magnet is always on and is non-linear (predominately multipolar), which has special implications on the pulse sequences, excitation hardware, and acquisition hardware. In this chapter, the pulse sequence is described along with the broadband excitation method needed to excite the wide bandwidth of the static encoding field. The RF coils are also described, as well as the receive array sensitivity profile.

### 1.2.4 Chapter 5

Traditional Fourier image reconstruction methods are not useful for our scanner because the encoding field is non-linear. The field cannot be easily be described analytically and there is no analytic inverse solution. Chapter 5 details the alternative generalized encoding matrix inversion reconstruction method. The encoding matrix calculation is described through the use of the field maps and coil sensitivity profiles. Two iterative matrix inversion methods for imaging reconstruction are described, the Karmarz method and Conjugate Gradients method. Finally, the resulting 2D images of phantoms and fruit are presented.

The contents of chapter 4 and 5 were both presented in Ref. [16] and Ref. [17].

### 1.2.5 Chapter 6

In Chapter 6, the ill-defined resolution of “rotating spatial encoding magnetic field” (rSEM) images are evaluated. Image encoding with non-linear magnetic fields results in a spatial resolution that varies over the field of view (FOV). This is because image resolution is directly related to the gradient of the SEM, and when the SEM is non-linear, the gradient is spatially non-uniform. This can be problematic if the SEM shape is dominated by high-order polynomials because this implies a gradient null,

which translates to an encoding hole. In this chapter images from multiple rSEMs are simulated, and the resolution of the resulting images is analyzed. These results inform the design of future magnets for the rSEM method.

This work was presented in Ref. [18].

### **1.2.6 Chapter 7**

Chapter 7 describes potential methods for encoding along the 3rd dimension of the scanner. Two  $B_1$  encoding methods are described, the Bloch Siegert encoding method (BS-set) and TRansmit Array Spatial Encoding (TRASE) method ([19], [20]). BS-set uses a varying magnitude off-resonance excitation pulse to apply a controlled variable phase to the spins along the encoding axis. TRASE uses an array of coils to create a  $B_1$  field that has a uniform magnitude, but linear phase along the encoding axis.

### **1.2.7 Chapter 8**

Chapter 8 concludes the discussion of the portable brain MRI project. Future directions of the scanner development are discussed including second iteration magnet simulations and design plans for a patient table. The contributions of this work are summarized.

### **1.2.8 Chapter 9**

Chapter 9 describes a separate, but related project: the implementation of low-cost, educational tabletop scanners. A series of 20 educational tabletop MRI scanners were developed with a 1 cm<sup>3</sup> imaging volume. These educational scanners, were built with all the elements present in clinical MRI scanners, but scaled down so they can be easily moved about a teaching lab. The budget for each of these scanners was \$10,000.

This work was presented in Ref. [21].

# Chapter 2

## Background

### 2.1 General MRI background

Magnetic Resonance Imaging (MRI) scanners use a combination of static and alternating magnetic fields to manipulate the hydrogen nuclear spins present in the body. A static polarizing magnetic field,  $B_0$ , creates a net alignment of the spins' magnetic moments in the  $B_0$  direction,  $z$ . When a sufficient proportion of spins are aligned, the net magnetization,  $\vec{M}$ , is detectable. The spin's have an intrinsic resonant frequency that is proportional to the  $B_0$  field strength - the Larmor frequency:  $f_0$ .

$$f_0 = \frac{\gamma}{2\pi}|B_0|, \quad (2.1)$$

where  $\gamma$  is the gyromagnetic ratio, a constant that is specific to the type of atomic nuclei. For hydrogen,  $\frac{\gamma}{2\pi} = 42.58$  MHz/T.

When  $\vec{M}$  is perturbed from alignment with  $B_0$ , it exhibits precessional motion <sup>1</sup> about the  $B_0$  direction ( $z$ ) at the Larmor frequency. In conventional scanners  $f_0$  is in the radiofrequency range. MRI sequences are made up of an excitation stage and acquisition stage.

---

<sup>1</sup>Precession is the same motion that a spinning top exhibits when it starts to fall out of vertical alignment.

### 2.1.1 Excitation

During the excitation stage, a magnetic field,  $B_1$ , alternating at the Larmor frequency is imposed. This excitation field, perturbs the  $\vec{M}$  alignment with the  $z$  axis, causing the spins to precess.  $B_1$  is applied orthogonally to  $B_0$ , and causes  $\vec{M}$  to rotate about the  $B_1$  direction by some “tip angle”,  $\theta$ , which depends on the duration and amplitude of the  $B_1$  pulse.

The precession of the spins eventually decays at time constants that depend on the properties of the the surrounding tissue (T1 and T2). This process is called relaxation. Figure 2-1 illustrates precession following an  $\theta = 90^\circ$  excitation pulse, and also the decay of the precession during relaxation.

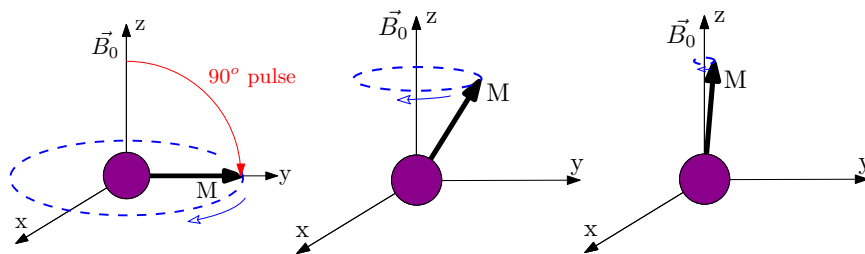


Figure 2-1: Illustration depicting the motion of the net magnetization of an ensemble of spins,  $\vec{M}$ . At equilibrium,  $\vec{M}$  is aligned with  $B_0$ . Immediately following a  $90^\circ$  excitation pulse,  $\vec{M}$  precesses in the  $x - y$  plane. The  $x - y$  component of  $\vec{M}$  can be detected with receive coils. Over time,  $\vec{M}$  returns to the equilibrium alignment with  $B_0$  at a rate described by relaxation time constants.

### 2.1.2 Acquisition

The second stage of pulsed NMR involves observing and acquiring data from the precession of the spins. According to Faraday’s law, a changing magnetic field in a loop of wire generates an emf that is proportional to the rate of change 2.2.

$$\varepsilon = -\frac{d\phi_B}{dt} \tag{2.2}$$

With sufficiently sensitive measurement hardware, the net magnetization of the precessing spins can be detected through Faraday’s law with antennae referred to as

receive coils.

### 2.1.3 Image Encoding

If  $B_0$  is uniform over the imaging object and the RF excitation field is applied uniformly, the precession of spins will be in phase and signals from spins at various locations in the object will be indistinguishable. In order to infer the source locations from the detected signal, spatial encoding magnetic fields are used,  $B_{SEM}$ . These encoding fields add gradient fields to the  $B_0$  field. Usually the field variation is linear (constant gradient), but linearity is not essential to image encoding.

The spatially varying encoding fields cause the precession frequencies of the spins to vary (eq. 2.3).

$$f(\mathbf{x}) = \frac{\gamma}{2\pi} |B_0 + B_{SEM}(\mathbf{x})| \quad (2.3)$$

We can predict the signal precession frequency and time-evolved phase at every location in the object, based on knowledge of the encoding magnetic fields that are applied. Therefore, after excitation, when the net signal from the precessing spins is acquired, the source locations of the components can be inferred, and an image of the object can be formed. If relaxation time constants are not considered, then image contrast is based on the spatial distribution of hydrogen (proton) density in the object. Contrast based on tissue dependent relaxation times can also be achieved. Spatial differences in relaxation times in the object are captured by different types of excitation pulses and the temporal spacing of the excitation pulses and the signal acquisition window.

## 2.2 Conventional MRI

### 2.2.1 Basic Hardware Components

Conventional Magnetic Resonance Imaging scanners are made up 3 basic magnetic field sources that are used to manipulate the magnetic moments of the hydrogen

atoms in the body.

1. The polarizing magnet: This magnet produces the static homogeneous magnetic field ( $B_0$ ) in the  $z$  direction, which polarizes the spin magnetic moments. Most  $B_0$  magnets are superconducting solenoid electromagnets cooled with liquid helium and produce 1 - 3 T fields. Less commonly, resistive electromagnets or temperature-stabilized rare-earth magnets have been used to generate  $B_0$  for low-field “open” MRI scanners. The homogeneity constraint results in magnets that are very heavy (5-10 tons) due to the numerous windings in the electromagnet case or iron yokes and shim plates in the permanent magnet case. These magnets are also mechanically fragile because of their cryostats and temperature stabilization equipment. In addition, the large stray field of conventional solenoidal MRI magnets requires a restricted area where ferrous materials are prohibited to prevent injury to the patient. The entire system is usually housed in a special Faraday cage room to prevent RF interference.
2. The gradient coils: In conventional MRI scanners, the spatial encoding magnetic fields are comprised of three individually controlled DC fields in the  $z$  direction that vary linearly in the  $x$ ,  $y$  and  $z$  directions. These gradient fields,  $G_x$ ,  $G_y$ ,  $G_z$ , are varied and switched during the imaging experiment, and require a high slew rate for reasonable imaging times. The fields are produced by specially shaped electromagnetic coils that are epoxy-potted, water-cooled copper windings weighing up to 1000 kg. The coils are driven with gradient power amplifiers that provide up to 900A and 2000V. High power is needed because high gradient strengths must dominate  $B_0$  inhomogeneities, and because fast switching is desired from the high inductance coils.
3. The excitation coil: The excitation coil is used to produce the alternating excitation magnetic field ( $B_1$ ) which tips the spins from alignment with  $B_0$ . The excitation magnetic field is perpendicular to the  $B_0$  field, and must oscillate at the resonant frequency of the scanner which is typically in the radio-frequency (RF) range. It is desirable for the  $B_1$  coil to be efficient in order to minimize the

power handling of the RF power amplifiers. This is achieved by using tuned resonant circuits and a high coil filling factor. Because the  $B_0$  field is typically produced by a solenoidal superconducting magnet with  $z$  along a cylindrical axis, a coaxial  $B_1$  solenoid cannot be used because of the orthogonality requirement of  $B_1$ . Instead less efficient birdcage coils or saddle coils are used.

### 2.2.2 Fourier Imaging: non-ideal for portable human scanning

When MR image encoding is done with switchable linear gradient fields, the k-space formalism can be used [22]. Conventional MRI pulse sequences indicate the timing of the gradient waveforms and RF excitation pulse, and are designed to fill the Cartesian spatial frequency domain, k-space, with data points. When k-space is sufficiently sampled, the image can be reconstructed very efficiently with a 2D discrete Fourier transform (DFT). This type of imaging is therefore referred to as Fourier imaging.

The key requirement of Fourier imaging is the use of linear encoding magnetic fields to provide a linear relationship between the detected signal frequency (or phase) and position. This means that the  $B_0$  field must be very homogeneous in relation to the gradient of the encoding fields in order for the linear relation to dominate. Alternatively, the linear gradient fields must be strong enough to dominate spurious encoding from  $B_0$  inhomogeneity. As an example, a typical 1.5 T low-end clinical MRI scanner might have a magnet homogeneity of  $<10$  ppm in a 40 cm diameter volume and use 10 mT/m gradients.

This Fourier imaging requirement is problematic for the design of portable MR scanner because it is inherently difficult to build a polarizing magnet with a reasonable field strength that is both lightweight and highly homogeneous. An inhomogeneous magnet can be counterbalanced by strong magnetic field gradients, but larger gradient fields require heavier gradient coils and high power consumption. In addition to being lightweight, a portable MRI scanner should operate from a standard power outlet or battery, and should not require special power services.

Taken together, conventional MRI scanners require a heavy magnet and a heavy gradient coil tethered to a large electrical service and specialized shielding; the oppo-

site of what is desired for portable systems. The size, power, and cost constraints of conventional MRI scanners limit their siting and accessibility. Siemens and Philips currently offer “mobile MRI” scanners. These scanners are transportable because the scanner rooms are replaced with trailers, but the scanners are essentially identical to their stationary counterparts. They are meant to be transported, parked, and plugged in (to electrical services capable of supplying hundreds of amperes) on a semi-permanent basis. They are often used as a temporary supplement to a hospital’s radiology service, but are not truly portable to the extent that they may be used in emergency field hospitals and standard hospital rooms.

## 2.3 Previous Work in Portable NMR/MRI

Several NMR devices for niche applications have explored relaxing the magnet homogeneity constraint, as well as reducing the reliance on traditional Fourier image encoding. The oil well-logging industry was the first to explore the idea of mobile NMR using “external sample”, or “inside-out”, NMR tools for measuring fluid in rock formations down-hole [23]. This work was initially done with electromagnets or in the earth’s field, but the advent of rare-earth magnets with high energy products such as SmCo and NdFeB [24], has allowed more effective borehole NMR tools to be developed [25].

Some portable single-sided NMR devices [26] [27] exploit inhomogeneous magnetic fields from permanent magnets for 1D spatial encoding. In these systems a rare-earth magnet array is placed against the object such that the field falls off roughly linearly with depth. Broadband excitation and spin-echo refocusing are used to obtain a 1D depth profile of the water content in the object [28], [29], [30]. Thus, these systems use the inhomogeneity of the small magnet to spatially encode the depth of the water; a principle that we exploit in a more complete way.

Recently, high resolution imaging has been achieved with table-top and small bore permanent magnet systems with long acquisition times [31], including a mobile MRI system developed for outdoor imaging of small tree branches [32]. However, these

scanners lack a bore size suitable for brain imaging and the long acquisition times are not conducive to imaging in triage settings.

There have been specialized clinical MRI systems that offer a smaller footprint and are easier to cite than conventional scanner. For example, Medtronic’s Polestar shows promise as a surgical MRI system that allows for intra-operative brain imaging [33], which has been shown to lead to more complete tumor resections [34]. The Polestar systems uses a 0.15 T permanent magnet and 23.5 mT/m linear gradient fields. The system is open and compact, but weighs 680 kg and requires a 3 phase, 400 V x 12 amp power source [35]. While these systems are relatively easy to retrofit in operating room, they are not portable.

There are several specialized MRI scanner for extremity imaging available (or previously available) including low-field (0.2 - 0.3 T) permanent magnet based scanners by Esaote, compacTscan and MagneVu/GE, and some high field (1 - 1.5 T) superconducting magnet scanners by ONI/GE [36]. Some of these are very compact and easy to site. For example, the Esaote O-scan is a 0.31 C-shape permanent magnet design that has low power requirements, a 9m<sup>2</sup> footprint, and does not require a shielded room. However, some of these low-field orthopedic scanners have been criticized for a limited ability to detect pathology compared to high-field MRI and limited field of view (although the compacTscan may have solved some of these problems) [37]. The MagneVu 1000 was a portable “in-office” extremity scanner primarily used for diagnosing rheumatoid arthritis erosion<sup>2</sup>. The scanner used 0.2 T permanent magnet with a permanent magnet gradient for one encoding direction. The MagneVu/Applause system is no longer in production, reportedly due to limited ability to detect synovitis, reduced FOV and poor resolution [36]. ONI Medical Systems introduced superconducting extremity scanners<sup>3</sup>. The Optima MR430s is a small footprint (20 sq<sup>2</sup>), superconducting 1.5 T scanner that weighs 408 kg, and is advertised to increase patient comfort and throughput without sacrificing image quality [38]. However, like conventional scanners, the high field magnet must be used in a stationary shielded

---

<sup>2</sup>The MagneVu 1000 was also distributed by GE as the “Applause”.

<sup>3</sup>The ONI MSK Extreme scanners were later distributed by GE as the “Optima MR430s”

environment. These extremity scanners set a precedent for the specialty MRI market.

## 2.4 Introduction to the rSEM encoding method

In 1973, Paul Lauterbur published an article titled “Image Formation by Induced Local Interactions: Examples Employing Nuclear Magnetic Resonance” [1], which presented the first 2D MR imaging method. He showed that when NMR signals are obtained in the presence of a magnetic field gradient, the water content of the object is integrated over the planes orthogonal to the gradient direction to form 1D projections. He presented the experiment shown in Figure 2-2, in which four 1D projections of two capillaries of water were acquired by rotating the object in  $45^\circ$  increments in the presence of a static gradient field. The four 1D projections were used to construct a 2D image referred to by Lauterbur as a NMR zeugmatogram. The NMR zeugmatography method is now well known as MR projection imaging.

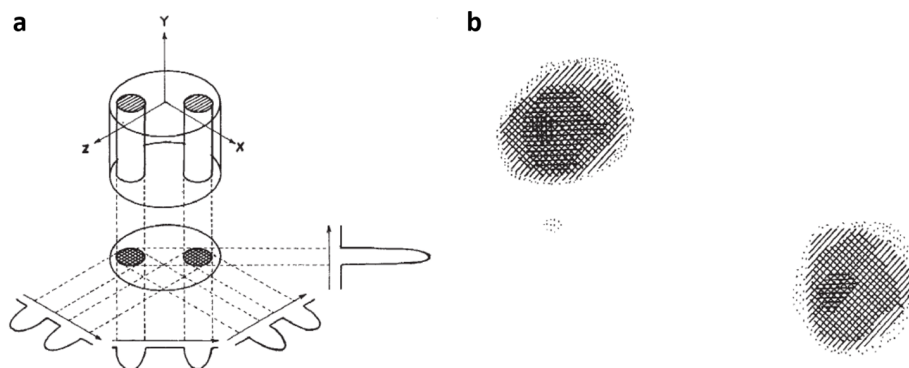


Figure 2-2: Figures from Lauterbur’s original NMR Zeugmatography paper. (a) The relationship between the 3D sample, the 2D projection along  $y$ , and the 1D projections in the  $x - z$  plane is shown. The 1D projections are formed by integrating over planes orthogonal to the gradient direction (indicated with arrows). (b) Proton NMR zeugmatograph (2D image of object) constructed from the four relative orientations of the object and gradients shown in (a).

In this work, we use an image encoding method based on rotating spatial encoding magnetic fields (rSEM) to create a portable scanner. The 2D encoding method is based on the projection imaging method described by Lauterbur [1], but the  $B_0$  magnet and linear gradient are replaced with a single rotating permanent magnet

featuring an inhomogeneous field pattern used for spatial encoding. In this scheme, the inhomogeneity in the  $B_0$  field serves as a spatial encoding magnetic field (SEM), and is a requirement for image encoding rather than a nuisance. Relaxing the homogeneity requirement of some conventional magnet designs leads to a reduction in the minimum required magnet material, and allows for more sparse/lightweight designs (45kg in our prototype). Additionally, the rotation of the magnet’s inhomogeneous field pattern replaces the function of heavy switchable gradient coils that come with significant power requirements.

Related work involving a mechanically rotating DC gradient field was published in 1998 by Cho et al. with a primary motivation of silent MRI [39]. The rotating electromagnet used by Cho et al. produced a linear gradient field, replacing the audible noise-producing X and Y pulsed gradients in a conventional scanner. Because the rotating gradient field was linear, traditional projection reconstruction methods could be used (filtered back projection), or the data could be interpolated to a k-space grid for conventional FFT image reconstruction.

In the presently described portable scanner, the dominant SEM field term is quadrupolar, which requires specialized acquisition and reconstruction techniques. Spatial encoding with similar nonlinear fields created with special gradient coils has recently drawn attention as a way to achieve focused high imaging resolution [40], reduced peripheral nerve stimulation [41], and improved parallel imaging performance [42]. In our scanner, the approximately quadrupolar SEM fields are physically rotated around the object along with the  $B_0$  field, and stationary RF coils are used to acquire generalized projections of the object in spin-echo train form.

In this manuscript, we describe the design, construction, and testing of a portable 2D MRI scanner. We show that our encoding scheme can achieve a resolution of a few millimeters in phantom images. While full 3D encoding is not demonstrated, the system is compatible with RF encoding schemes, such as the TRASE method [20], [43], capable of adequately encoding the third dimension (along the axis of the cylindrical magnet).



# Chapter 3

## Magnet - Polarizing and Encoding fields

### 3.1 Magnet Design Considerations

To build a truly portable scanner that is easy to use in remote locations, the hardware design should be as simplified as possible. Arguably, the biggest challenge in realizing a portable MR system, is the design of a lightweight  $B_0$  magnet with a strong homogeneous field and a sufficient bore geometry [44], [45]. The use of a superconducting magnet for  $B_0$  is unreasonable because of the complexity of the cryostat. Assuming the proposed rotating encoding method, a superconducting magnet would be far too delicate. It may be possible to implement a rotating electromagnet through careful cable management, but the need for a large stable current supply would increase the weight of the scanner and the power requirements. All of these considerations lead us to a permanent rare-earth magnet array design. The size and arrangement of permanent magnets determines the weight of the magnet, the  $B_0$  field strength, and the spatial encoding magnetic field shape. The rotating Spatial Encoding Magnetic field MRI (rSEM MRI) encoding method is valid for arbitrary encoding field strengths and shapes, but the field strength will affect the signal to noise ratio (SNR) and the field shape will affect the spatially variable resolution of the images. There are several considerations in designing the permanent magnet arrangement for brain imaging:

1. Average field strength ( $B_0$  strength): Higher magnetic field strengths generally lead to higher image SNR. This has motivated the push to higher and higher field strengths in conventional scanners. When a stronger magnet is used, there is a higher percentage of spins that align with the  $B_0$  field, which means a larger net magnetization  $\vec{M}$  to detect after excitation. Higher field strengths also translate to a higher Larmor frequency. This means that the Faraday detected signal is at a higher frequency. This leads to an SNR improvement as well because according to Faraday’s law<sup>1</sup>, the electromagnetic induction produces an EMF (electromotive force), which is proportional to  $dB/dt$ , the rate of change in the magnetic field.
  
2. Encoding capability (high enough gradient): As described in section 2.2, conventional  $B_0$  magnets are required to be very homogeneous for Fourier imaging. In contrast, our method requires variation in the  $B_0$  magnet for spatial image encoding. Even though they are produced by the same magnet in our case, we can think of the “encoding field” and  $B_0$  field separately by subtracting the mean magnetic field magnitude ( $B_0$ ) from the magnetic field map. When considering the encoding field intuitively, we can think of magnetic field values mapping to specific locations in the image. If the encoding magnetic field varies gradually in space, the image resolution will be low because the points in the image will blur together. Therefore, we want sufficiently high gradient values in the encoding field. For uniform image resolution, a linear encoding field (constant gradient) is necessary. However, we have chosen to relax the linear encoding field constraint in order to simplify the hardware, and therefore expect non-uniform image resolution.<sup>2</sup>
  
3. Reasonable Larmor frequency bandwidth (low enough field variation): Although we want significant encoding field gradient values, we want the total field variation to be limited. Unlike in traditional MRI scanners, the excitation pulses

---

<sup>1</sup>Faraday’s law is  $\varepsilon = -d\phi_B/dt$ .

<sup>2</sup>Note: In the first magnet iteration we did not try to optimize the encoding field shape. We will see later that the encoding shape has a significant impact on the image resolution, which will be taken into account in the 2nd magnet design iteration.

must be played in the presence of the encoding field because it is produced by permanent magnets (cannot be switched off). The magnetic field range of the encoding field translates that to a Larmor frequency range. For example, for a encoding field variation of 5 mT, the encoding bandwidth is 213 kHz. This encoding bandwidth is significant to the excitation and data acquisition methods. During excitation, we want to impart the same spin flip angle to the entire field of view. In order to do that we need the excitation bandwidth to cover the encoding bandwidth. If we use a basic square RF pulses, we must use very short high power pulses to excite the bandwidth (more in section 4.3). This is undesirable because large RF power amplifiers are necessary for these wide bandwidth RF pulses. In addition, the RF coils are tuned to a specific frequency. In order to achieve uniform efficiency over a wide bandwidth, low Q (quality factor) RF coils must be used. For example, for a field variation of 5 mT and average field of 100 mT, the bandwidth is 213 kHz, the average resonant frequency is 4.258 MHz, and the coil Q must be 20. This is undesirable, because low quality factors decrease coil efficiency.

4. Magnet material mass: The amount of rare-earth material in the magnet design determines the weight and cost. Rare-earth magnet material is expensive and heavy compared to the equivalent copper wire required for an electromagnet. The weight and cost of rare-earth material has been a deterrent in MRI scanners in the past. Minimal magnet weight is obviously desired to increase portability of the scanner. However, a higher  $B_0$  can generally be achieved with more rare-earth material. A maximum weight was not set, but limiting the number of rare-earth magnet blocks was a consideration in the design.
5. Permanent magnet material: In addition to weight, another historic deterrent to the use of permanent magnets is the magnetic field drift which changes reversibly with temperature [46], [47]. The ratio of the change with temperature is the “temperature coefficient”. Field drift is a problem that must be addressed in all permanent magnet based NMR systems. The temperature coefficient of rare-

earth magnets vary. For example, SmCo grade 26 magnets have a temperature coefficient of 300 ppm/°C and NdFeB grade 48 magnets have a temperature coefficient of 1200 ppm/°C. This means that if the N48 NdFeB magnets were used to build a 0.1 T magnet, a 1°C change in temperature would lead to a 5 KHz change in the Larmor frequency. In the same situation the grade 26 SmCo magnets would lead to a 1 kHz change in Larmor frequency. Ideally, we would avoid such changes which lead to off-resonance RF and field map inaccuracies, and SmCo magnets are preferred for this temperature stability consideration. However, NdFeB magnets are roughly 50% lower in cost and up to 30% higher remnant flux density ( $B_r$ ) than the SmCo magnets. In addition, NdFeB magnets are more commercially available in a variety of shapes. It was a requirement to use commercially available stock material in order to keep costs down. This means either bar and cylindrical magnet pieces are favorable.

6. Human head geometry: There are difficult geometrical constraints on the magnet array to achieve human brain imaging. Figure 3-1 illustrates some benchmark geometric measurements for human brain imaging. Clearly, there must be an opening (bore) in the magnet into which a human head can be inserted. The opening should be at least 26 cm in diameter<sup>3</sup>. The magnet should be designed to fit closely around the head to maximize  $B_0$ . Similar to the design of head-only gradient coils [48], this means that the magnet should remain above the shoulders of the subject. It is generally assumed that the center of the brain is located 18 cm above the shoulders, so if the magnet is symmetric with the brain in the center, the length is limited to 36 cm.

---

<sup>3</sup>We did not meet this bore opening requirement in the first magnet iteration, because additional magnets were added to the end to boost the field fall off along the length of the magnet. This is taken into account in the 2nd magnet design iteration.

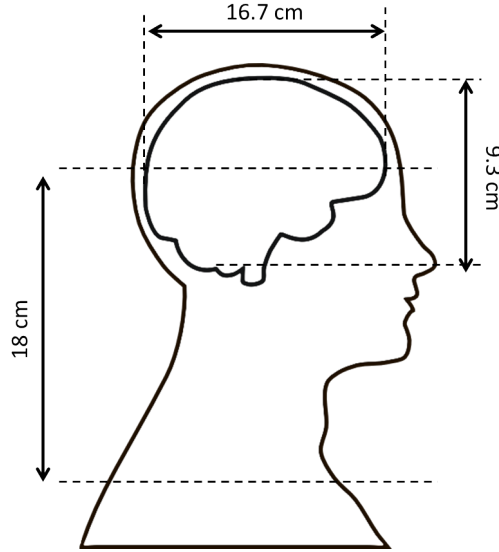


Figure 3-1: Anatomical benchmarks for human brain imaging.

### 3.2 Background - Permanent Magnets in MR

Permanent magnet designs for magnetic resonance applications fall into 2 categories, yoked and yokeless. An ideal yoke is a medium with infinite magnetic permeability, which contains and directs the magnetic flux. In practice, yokes are made from soft iron or high permeability steel. Yokes can be integrated into complex prismatic shaped permanent magnets, such as those described by Abele [49], but they are usually used more simply as a method of returning flux between two permanent magnet pieces configured in a dipole configuration. The two permanent magnet poles may be “hockey puck” shaped pieces, or made up of several smaller pieces in the case of larger magnets. The most common implementations were summarized by Jiang et al. in Figure 3-2. An example of a four-column structure was implemented by Miyamoto et al. [47] in 1989. This four-column implementation was intended for “compact” human MRI scanners, and weighed 9 tons with a 0.2 T field, 0.5 m gap, and a homogeneity of 30 ppm in a 35 cm diameter spherical volume. Variations of the two-column yoked magnet are commonly seen in home-made or commercial educational NMR/MRI systems and sometimes referred to as “closed C-shaped” or “H-shaped” configurations [50], [51], [52], [53], [21]. For example, Pure Devices produces a benchtop MRI system with a 17.5 kg, 0.5 T “close C-shaped” magnet for imaging

10 mm samples. Asymmetric two-column designs have also been implemented for whole-body human MRI [2], including the 0.3 T Hitachi Airis magnet. Finally, the most ubiquitous yoked permanent magnet design is the one-column or “C-shaped” design. This design has been used for portable or desktop MRI designs [54], [55], and has also been the basis for commercial “open-bore” permanent magnet scanners such as the Siemens Magnetom C! (0.35 T).

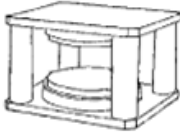
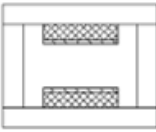
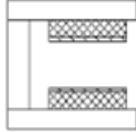
	Four columns	Two columns	C-shaped
<b>Magnet type</b>			
<b>Access</b>	wide	wider	widest
<b>Field homogeneity (before shimming)</b>	highest	higher	OK
<b>Flux leakage</b>	lowest	lower	low
<b>Mechanic stability</b>	best	better	OK

Figure 3-2: Figure from [2] by Jiang et al., which summarizes popular yoked permanent magnet designs.

In 1973, Mallinson introduced planar magnetization patterns which resulted in “one-sided flux” [56]. This was the basis for subsequent “magic ring” and “magic sphere” yokeless permanent magnet designs. Klaus Halbach first discussed permanent multipole magnets based on the same principle with the use of rare earth cobalt material in 1980 [57]. He introduced quadrupole designs for particle accelerators, as well as linear designs for undulator and production of synchrotron radiation [58], [59]. Around the same time, Abele and Leupold demonstrated various similar yokeless permanent magnet designs that included “magic rings” and square cavity magnets made up of triangular prism shaped magnets [49], [60], [61]. While this yokeless square-cavity design has proven effective in a small permanent magnet MRI scanners [62], the dipolar version of the Halbach cylinder have gained more popularity in portable NMR devices.

Halbach cylinders are often considered the most efficient permanent magnet geometry for producing high fields [63], and offer a good balance of a comparatively strong field for a relatively large bore size and weight [64]. In addition, the cylindrical inner

geometry is ideal for a head scanner, and the cylindrical outer geometry is convenient for rotation purposes. Therefore, we chose a Halbach cylinder-based design for our magnet.

Ideal Halbach cylinder magnets are infinitely long continuous hollow cylinders, with a continuously rotating magnet polarizing along the circumference. When the polarization along the circumference rotates by multiples of  $2\pi$ , the flux is completely contained inside the cylinder. The mode ( $k$ ) determines the number of poles in the Halbach cylinder. At angle  $\theta$ , the polarization orientation is  $\varphi$  (see Figure 3-3).

$$\varphi = k \times \theta \tag{3.1}$$

Figure 3-3 illustrates the cross-section of a  $k = 2$  ideal Halbach cylinder. The dipolar mode creates a homogeneous magnetic field oriented transversely to the axis of the cylinder, and is of use in NMR experiments as the polarizing  $B_0$  field. The orientation of the magnet polarization around the circumference mimics the fringe field that would result from a perfect magnetic dipole along the center of the cylinder.

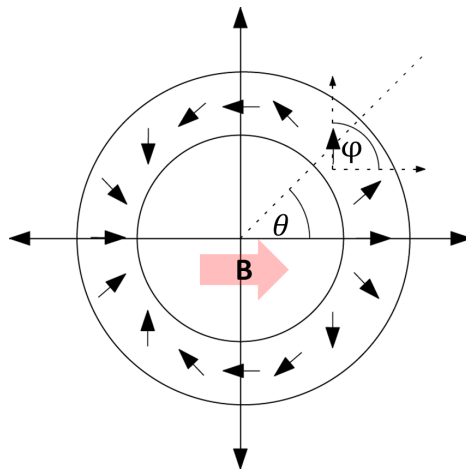


Figure 3-3: The magnet polarization is shown around the circumference of a dipolar ( $k = 2$ ) Halbach cylinder.

Dipole Halbach cylinder's offer many advantages to other permanent magnet designs:

1. Halbach dipole designs that have a large outer radius ( $r_{out}$ ) relative to the inner

radius ( $r_{in}$ ) can result in a center field ( $B$ ) that exceeds the remnant flux density of the magnet material ( $B_r$ ).

$$B = B_r \ln(r_{out}/r_{in}) \quad (3.2)$$

The largest reported remnant flux density in permanent magnets is 1.5 T (Neomax 50), but Halbach-based permanent magnets have been assembled with fields exceeding 5 T [65].

2. The lack of iron/steel yoke pieces result in a higher field to weight ratio. For a given bore cross-sectional area, the C-shape magnets generally have a lower field and are heavier [64].
3. The resulting  $B_0$  field is oriented transversely to the long axis of the magnet. This allows the use of solenoid RF coils which produce an orthogonal  $B_1$  field along the cylindrical axis, and are well known to be more efficient to transverse  $B_1$  coils (bird-cage, saddle, Alderman-Grant) [66].
4. Ideal Halbach cylinders are particularly useful for portable MRI applications because the flux is completely contained in the magnet. Although, there is some flux leakage in a non-ideal segmented Halbach cylinder, the field is relatively well-contained and the stray field is minimal.

These properties have led to use of Halbach magnets in many portable applications [44], [67], [68], [69], [70], [71]. Clearly, the ideal Halbach cylinder design is not realizable, and all of the above mentioned cases used finite length, discrete (sparse in some cases) magnet designs. The closest feasible approximation to the ideal magnet, is broken up into trapezoidal shaped segments. This trapezoidal-based geometry is the best choice if a high and homogeneous field is the priority [65]. However, it is difficult and expensive to machine and accurately polarize the trapezoidal magnet pieces. Therefore, when cost and weight are a priority it makes sense to use an assembly of rectangular and cylindrical stock-magnets. In Ref. [67], Moresi et al. show that the use of sparse material makes equation 3.2 invalid, and show that equation 3.3 applies

to the use of cylindrical magnet pieces, where  $n$  is the number of cylinders,  $R$  is the radius of each cylinder,  $r$  is the distance between the center of the assembly and the center of the magnet piece, and  $B_r$  is the remnant flux density.

$$B = \frac{n}{2} B_r \frac{R^2}{r^2}. \quad (3.3)$$

The finite length of the cylinder must also be accounted for when estimating  $B$ . Zhang et al. reported an analysis in which the “fringing effects” of the Halbach cylinder length were evaluated [72]. The study assumed  $r_{out}/r_{in} = 2$  and reported the ratio of the cylinder length ( $L$ ) which was within 90% of the maximum field strength<sup>4</sup>. For  $\frac{L}{2r_{in}} = 1$  the ratio was 50%, for  $\frac{L}{2r_{in}} = 4$  the ratio was 70%, and for  $\frac{L}{2r_{in}} = 10$  the ratio was 90%. In addition, the maximum field  $B$  compared to the field in the ideal Halbach ( $B_{ideal}$ ) is also affected by the cylinder length. For example, for  $\frac{L}{2r_{in}} = 1$   $\frac{B_{max}}{B_{ideal}} = 0.75$ , and for  $\frac{L}{2r_{in}} = 2$   $\frac{B_{max}}{B_{ideal}} = 0.9$ .

### 3.2.1 Halbach magnets for portable NMR

In 2003, Moresi et al. [67] describe a small 8 rung Halbach cylinder (array diameter = 9 cm) using cylindrical magnet (diameter = 2 cm, length = 15 cm) for tabletop NMR experiments. Iron plates with a 5 mm small gap for access were added to the ends of the cylinder to improve homogeneity. The resulting field was 0.6 T with 20 ppm homogeneity in a 3-5 mm ellipse.

In 2004, Raich and Blümlier introduced the NMR Mandhala (Magnet Arrangements for Novel Discrete Halbach Layout), which was a dipolar Halbach magnet arrangement using identical stock bar magnets with square cross-sections. The magnet consisted of Halbach rings (5.7 cm diameter) made up of 16  $1.8 \times 1.8 \times 2.2$  cm closely spaced magnet pieces, sandwiched between aluminum sheets. Eight of the “sandwiches” were stacked together to form the complete 11.4 kg magnet, which produced a 0.3 T  $B_{max}$  field. In 2011, Wroblewski et al. [73] reported an attempt to expand the NMR Mandhala into a more useful size (29 cm diameter) for low-field

---

<sup>4</sup>As we will see later, this  $r_{out}/r_{in}$  ratio is much higher than in our design, so the results in [72] may not be relevant.

MRI. They stacked four “sandwiches” of 16  $2.5 \times 2.5 \times 5.0$  mm magnet pieces for a 26 cm length (including aluminum plates). The resulting assembly produced a 20 mT field in the center, with very poor homogeneity. It was intended to include 32 magnets in each ring, to produce a theoretical field of 0.1 T, but the assembly was too difficult because the magnet pieces were designed to be very close together (almost touching).

In 2005, Hills et al. reported the construction of a small sparse Halbach dipole design for “open-access” NMR [69]. The magnet was constructed of only four  $1.8 \times 1.8 \times 20$  cm magnet rungs, with an overall diameter of 7.4 cm. The center  $B$  field was 89 mT, with an estimated homogeneity of 2300 ppm in 1 cm DSV.

In 2009, Danieli et al. presented a highly homogeneous mobile Halbach array design [68]. Similar to the “NMR Mandhala”, this magnet consisted of 6 stacks of Halbach rings made up of 16  $4 \times 4 \times 4$  cm NdFeB blocks. However, Danieli et al. optimized the spacing between the stacks, improving the fringe field behavior along the cylindrical axis. The resulting magnet (including aluminum housing) had an inner diameter of 20 cm, an outer diameter of 33 cm, and a length of 27 cm. The magnet weighed 50 kg and had an average field strength of 0.22 T. They went on to shim the field using small NdFeB shim blocks. The field was mapped, and simulation software was used to determine the position and size of the shim units. In addition, linear fields from the gradient coils were also used for shimming. The pre-shimmed magnet produced a 20 kHz line width for 3 cm volumes, and the shimmed magnet produced a 0.1 kHz line width.

### 3.3 Magnet Design (version 1)

The magnet design method was based on 3D simulations of the flux density produced by NdFeB magnet pieces from COMSOL Multiphysics. Although we can tolerate significant inhomogeneity in the magnet (in fact it is necessary for image encoding), it soon became apparent that designing a magnet with a reasonable homogeneity over the roughly brain size volume while maintaining a small lightweight design was

a significant challenge.

Although, simulations began with arbitrary arrangement of permanent magnet pieces, the orientation of the pieces soon converged to “magic ring”, or Halbach cylinder based polarizations. Similar to other mobile low-cost Halbach designs in [67], [68], [69], [70], [71], [44] we chose to use stock magnet material instead of trapezoidal pieces. Although cylindrical magnet pieces were considered, we chose to use rectangular stock material for ease of construction. Cylindrical pieces are more difficult to accurately orient in a Halbach assembly. Our design is therefore similar to the NMR Mandhala [70], except we chose to use continuous magnet rungs instead of stacked Halbach rings. The N42 magnet bars were obtained from Applied Magnets (Plano, TX). A  $1'' \times 1''$  cross-section was chosen as a manageable size. These N42 NdFeB magnets have a remnant flux density of  $B_r = 1.32$  T, and temperature coefficient of 1100 ppm/C°.

### 3.3.1 $y - z$ plane

Several array diameters and rung quantities ( $N$ ) were simulated to compare trade-offs in field strength, homogeneity, and weight. Unlike the NMR Mandhala designs [70], [68], [73], a reasonable amount of space was reserved between magnet rungs ( $> 2$ cm) because of the envisioned construction method (section 3.4). Figure 3-4 shows simulations of  $N = 20$  designs with varying array radii. The average magnetic flux density was evaluated in the center 20 cm diameter spherical volume (DSV),  $B_{ave}$ , as well as the Larmor frequency range,  $f_{range}$ . The resulting design consists of  $N = 20$   $1'' \times 1''$  magnet rungs, with an array radius of  $r = 18$  cm (distance from array center to center of rung).

### 3.3.2 $x$ profile

Longer Halbach cylinders perform more closely to the ideal Halbach cylinder, and there are significant fringe effects associated with short cylinders. According to Zhang et al. [72] (and intuitively), the ratio of the length  $L$  to inner radius  $r_{in}$  should be

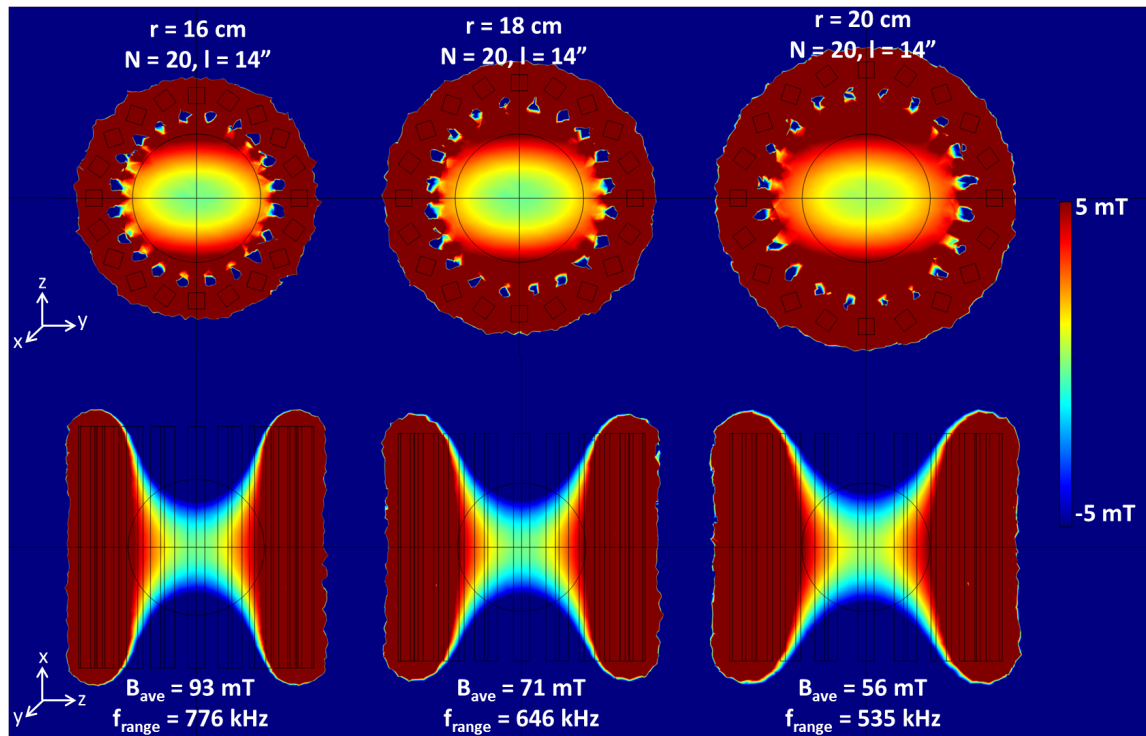


Figure 3-4: Magnetic flux density simulations of three sparse dipolar Halbach cylinder designs are shown. The field was evaluated in a 20 cm spherical volume (outlined in black). The average fields ( $B_{ave}$ ) and the Larmor frequency ranges ( $f_{range}$ ) in the sphere are indicated. The colorbar range was chosen to be  $\pm 5$  mT of  $B_{ave}$  for each model. The cylindrical arrays are 14" long and made of 20 NdFeB magnet rungs (outlined in black). The simulation shows a comparison of three array radii (distance from the array center to center of magnet rung).

maximized. Therefore, we would like the cylinder to be as long as is allowed by the geometrical constraints described in section 3.1 (#6), the length of the magnet array is limited by the distance to the subject’s shoulders. According to the common benchmark, the brain is centered 18 cm above the shoulders. Since it is assumed that the strongest and most homogeneous region of the cylinder is in the center, we designed the array to be  $\approx 36$  cm long so that a subject’s brain would be roughly centered. The stock material from our vendor (Applied Magnets) is available in 1” increments, so  $L = 14''$  ( 35.56 cm) rungs were used. Our length to diameter ratio,  $L/2r$  is roughly 1.

We are interested in a relatively large volume, so fringe effects along the x-axis are problematic. The average adult brain height is 10 cm. Assuming a magnet length of  $L = 35.5$  cm, we are interested in about  $10 \text{ cm}/35.5 \text{ cm} = 28\%$  of the  $x$  dimension of the magnet for imaging. However, given subject size variations, we care about at least  $15 \text{ cm}/35.5 \text{ cm} = 42\%$ . According to [72], 50% of the cylinder length will be within 90% of  $B_{max}$  for  $L/2r = 1$ , but a 10% field variation is unacceptable. Figure 3-5 shows the field fall-off along the x-axis for the  $N = 20$ ,  $r = 18$  cm,  $L = 14''$  array.

There are a few methods in the literature to compensate these fringe effects. For example, the addition of iron plates at the end [67] and the optimization of the Halbach ring stack spacing [68]. We chose to add two additional Halbach “end rings” made up of twenty 1” NdFeB cubes inside the main array at the ends of the cylinder to reduce field fall-off. Figure 3-5 and 3-6 shows the effect of this. The spacing between the end rings can be optimized to provide the flattest flux density profile along the  $x$  axis. Figure 3-6 shows the simulated  $x$  profile for three spacing options, and compares the results to an approximately infinitely long cylinder and the 14” cylinder with no end rings. The 30 cm spacing (red line) provided the highest simulated homogeneity along the  $x$  axis, and was incorporated into the final design.

Figure 3-7 shows a 3D drawing of the final magnet design, the simulated field, and a photo of the constructed magnet. Unfortunately, the addition of the Halbach end rings limit the magnet accessibility. Although the bore is still theoretically large enough for an adult head plus RF coils, the constructed bore opening is a smaller

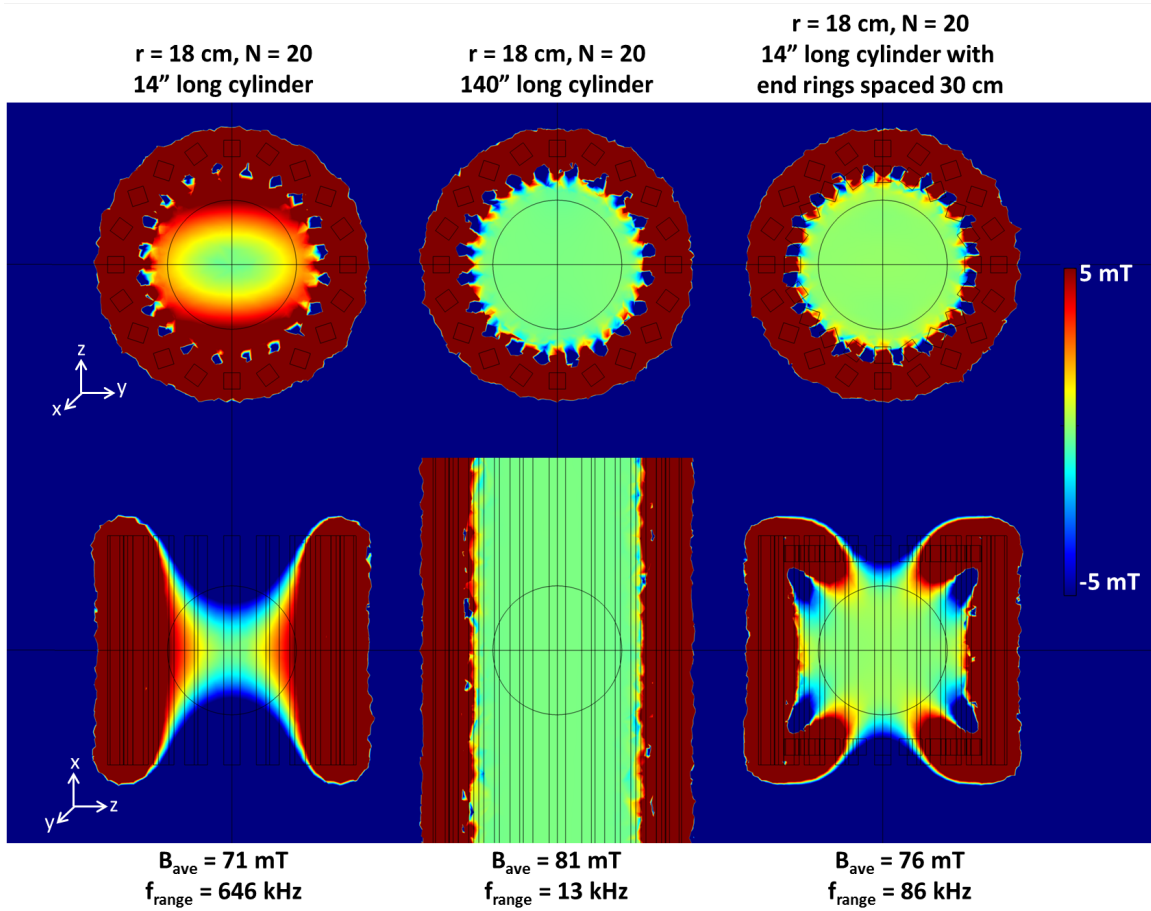


Figure 3-5: Magnetic flux density simulations of three sparse dipolar Halbach cylinder designs are shown. The cylindrical arrays are made of 20 NdFeB magnet rungs (outlined in black) with a radius (distance from array center to center of magnet rung) of 18 cm. The simulation shows a comparison of the filed pattern in the  $x$  direction, for a 14" long cylinder a 140" long cylinder, and for a 14" long cylinder with additional booster Halbach rings. The field was evaluated in a 20 cm spherical volume (outlined in black). The average fields ( $B_{ave}$ ) and the Larmor frequency ranges ( $f_{range}$ ) in the sphere are indicated. The colorbar range was chosen to be  $\pm 5$  mT of  $B_{ave}$  for each model.

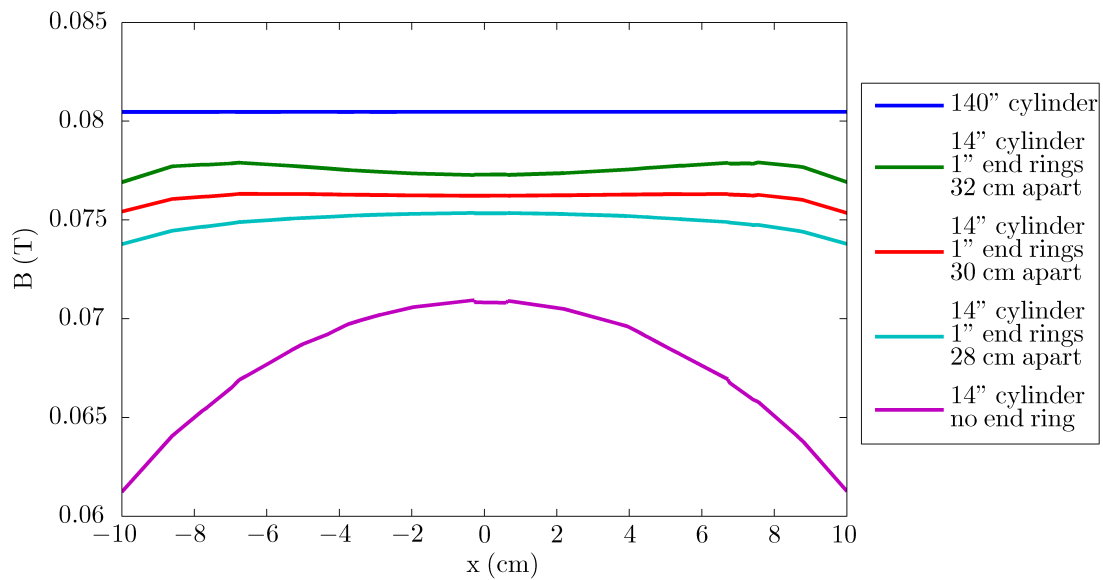


Figure 3-6: The simulated magnetic flux density variation along the  $x$  axis is shown for several sparse Halbach cylinder designs, including the three simulations shown in Figure 3-5. Three  $x$  spacings of Halbach booster rings (end rings) are compared along with models with no end rings and the 140" long cylinder. The 140" long cylinder can be approximated as infinitely long (compared to the radius), and has a very flat field profile along  $x$ . Practically, the length of the cylinder is limited to 14", and the 30 cm booster ring spacing produces the flattest  $x$  profile with this constraint.

diameter (23 cm), which is too small for a subject's head and RF coils. This will be addressed in the next magnet iteration. However, the magnet described here is still capable of imaging our targeted brain size objects.

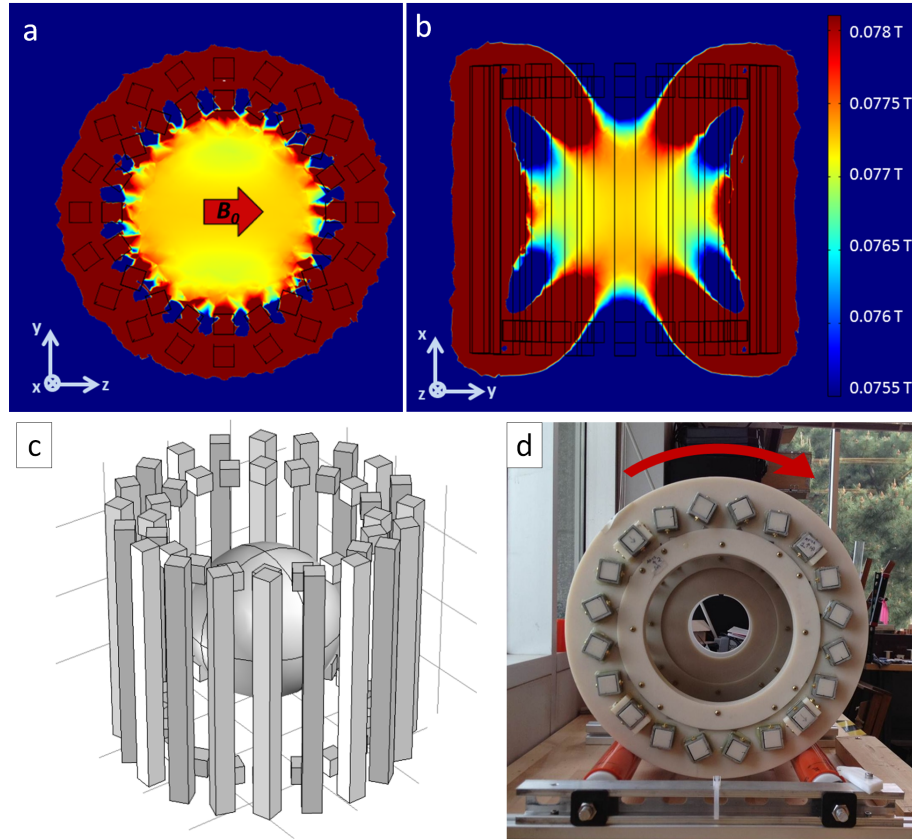


Figure 3-7: The magnet array consists of twenty 1"x 1"x 14" NdFeB magnets oriented in the  $k = 2$  Halbach mode. Additional Halbach rings made of 1"x 1"x 1" magnets were added at the ends to reduce field fall off along the cylindrical axis. (A,B) Simulation of the magnetic field in two planes. The field is oriented in the  $z$ -direction (transverse to the cylinder axis). (C) Schematic of NdFeB magnets composing the array. The targeted spherical imaging region (18 cm diameter) is depicted at the isocenter. (D) End-view photo of the Halbach magnet mounted on high friction rollers. The Magnet was constructed with ABS plastic and square fiberglass tubes containing the NdFeB magnets. Faraday cage not shown.

### 3.4 Magnet Hardware and Construction

The NdFeB magnet configuration is only one aspect of the magnet design. The mechanical design of the magnet housing and construction procedure are significant.

### 3.4.1 Force simulations

The simulated forces between the magnet rungs are shown in Figure 3-8a. Although the “pull-force” between the largest magnet pieces ( $4'' \times 1'' \times 1''$ ) is 979 N (220 lbf), the internal forces in the constructed Halbach array are much lower. Fortunately, the maximum estimated internal force was estimated to be 178 N (40 lbf), which can be adequately handled by the fiberglass and ABS frame chosen for the magnet frame. ABS and fiberglass are convenient because they are not conductive and therefore prevent potential eddy currents in the magnet housing, and are relatively lightweight and easy to machine.

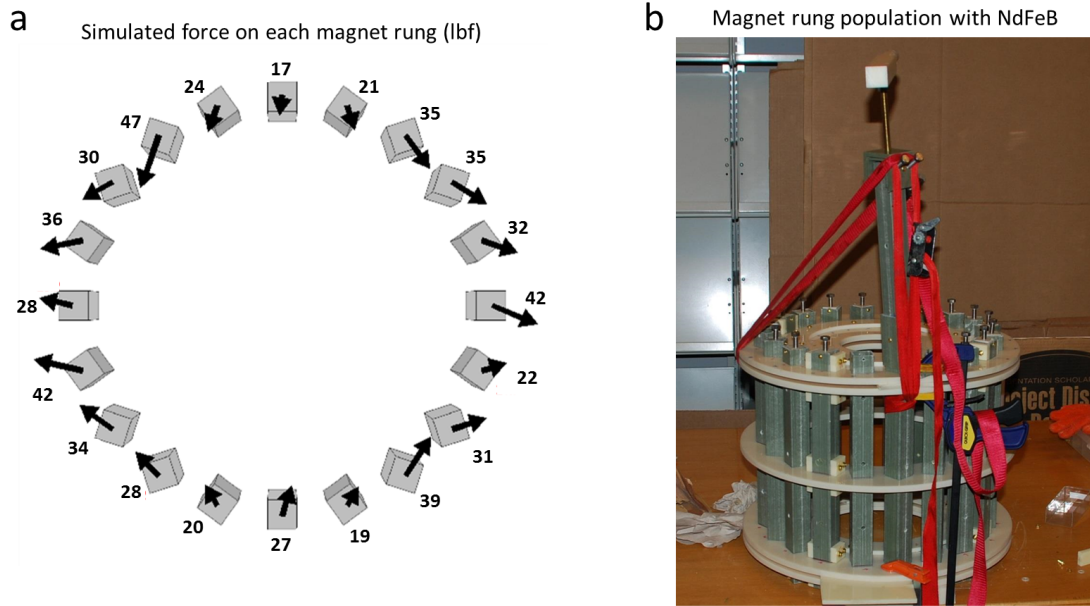


Figure 3-8: (a) The radial forces between the Halbach magnet’s rungs were simulated with COMSOL prior to designing the magnet frame. (b) The magnet frame was fully constructed from sheets of ABS plastic and fiberglass square tubes before populating the magnet rungs. The 1” Halbach end rings were integrated in the frame construction. Each 14” magnet rung is made up of three 4” magnet bars and one 2” magnet bar, which repel each other inside the fiberglass tubes. To populate the magnet rungs, NdFeB pieces were inserted one at a time, and bonded together with Loctite magnet bonding adhesive. A jig was used to push the bars together while the adhesive cured. The jig is shown mounted to the table and magnet with straps while two bar magnets were bonded together in the fiberglass rung.

### 3.4.2 Magnet Housing

The magnet rungs consist of NdFeB magnets stacked inside square fiberglass tubes (McMaster-Carr, Elmhurst, Illinois USA). Each 14" long magnet rung is comprised of four individual bar magnets (Applied Magnet, Plano, TX, USA) which were bonded together (three 4" bars and a 2" bar).

The 1" Halbach end rings were constructed by sandwiching the 1"x1"x1" magnets between ABS pieces (similar to the Halbach rings in [70]). The end ring "sandwiches" were incorporated in the magnet housing assembly.

The fiberglass tubes are fixed in place by five 3/8" ABS rings (two on each end and one in the center). To precisely orient the magnet rungs, square holes were waterjet cut from the ABS rings. The ABS/fiberglass frame was fully assembled prior to NdFeB magnet handling. To accurately position the fiberglass tubes in the ABS rings, plastic blocks fixed to the tubes were used as stops, while ABS rings and tubes were epoxied together.

### 3.4.3 Magnet Population

After the frame was constructed, the magnet rungs were populated one at a time. The four magnets comprising each rung repel each other as they are inserted into the tube, so a magnet loading and pushing jig was necessary to force the magnets together while the magnet bonding adhesive cured (Loctite p/n 331 and 7387). The jig was a simple threaded rod mounted to the magnet assembly frame above the opening of the fiberglass tube. Figure 3-8b shows a photo of the magnet population process. The fiberglass tubes were cut to be longer than 14" to facilitate the magnet loading process. Large stainless steel bolts were used at the ends to fill the excess space, and prevent the bonded magnets from sliding around in the tube<sup>5</sup>.

---

<sup>5</sup>The bolts were probably an unnecessary precaution because the magnet bonder also seems to adequately bond the magnets to the fiberglass tube.

### 3.4.4 Rotation Hardware

The cylindrical magnet sits on heavy-wall aluminum tubes covered with a high friction urethane. The MRI console is used to drive a stepper motor (model 34Y106S-LW8, Anaheim Automation, Anaheim, CA, USA) that is attached to the aluminum axis of one of the rollers through a 5:1 gearbox (model GBPH-0901-NS-005, Anaheim Automation, Anaheim, CA, USA). Magnet rotation is incorporated into the pulse sequence so that it is controlled by the MRI console to a precision of one degree at a rate of 10 deg/s. Peripheral nerve stimulation is not a concern with this  $B_0$  rotation rate. Even at 10x the current rotation rate, the dB/dt from the rotating magnet is 2 orders of magnitude below the dB/dt generated by a modest clinical gradient system.

### 3.4.5 Results

The constructed magnet weighs 45 kg and has a 77.3 mT average field in the 16 cm field of view (FOV) center plane, corresponding to a 3.29 MHz proton Larmor frequency. Although, simulations were based on a 20 cm diameter spherical volume (DSV), subsequent field maps (discussed in section 3.5 and 3.6) will be in a 16 cm DSV (which nearly encompasses the average brain size) due to field mapping hardware limitations. The magnet assembly is enclosed in a copper mesh Faraday cage to reduce RF interference.

## 3.5 Gaussmeter Map and Shimming

An initial 3D field map was obtained with a 3-axis gaussmeter probe attached to a motorized stage. Figure 3-9 shows a photo of the gaussmeter/motorized stage setup, and a plot of the measurement points. The measured field shape is roughly quadrupolar, similar to the fields used in the initial realization of multipolar PatLoc (Parallel Imaging Technique using Localized Gradients) encoding [41], but with other significant field components as well. The measured field variation range in y-z (imaging plane), x-z, and x-y planes of a 16 cm sphere were  $\Delta f_{yz} = 95$  kHz,  $\Delta f_{xz} = 60$  kHz and

$\Delta f_{xy} = 52$  kHz. Variations from the simulated field are expected and very common in permanent magnet assemblies due to small perturbations in the remnant flux density and polarization direction of the magnet blocks. In addition, small errors in magnet block positioning are likely.

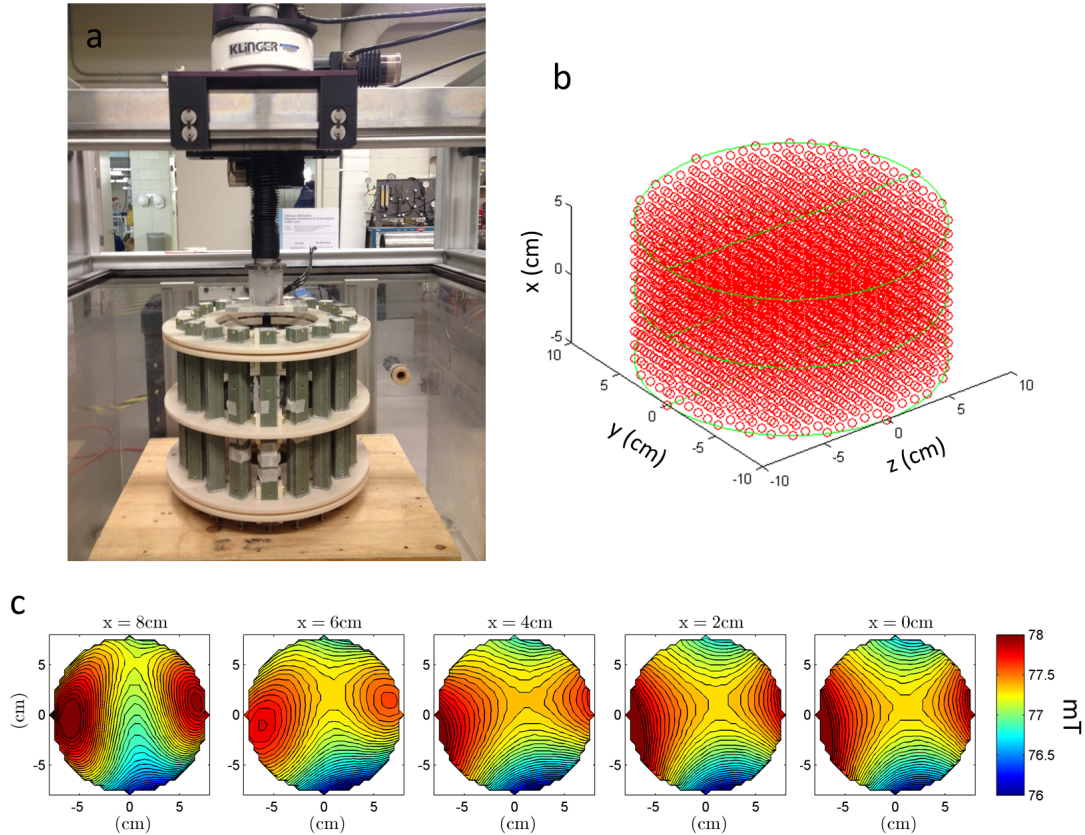


Figure 3-9: (a) A gaussmeter probe mounted to a computer controlled 3-axis translation stage was used for initial field maps. (b) The 3D gaussmeter measurement points are plotted (c) The resulting axial field maps are shown for several  $x$  slices.

As described in section 3.1 (#3), large Larmor frequency bandwidths make it difficult to design RF excitation and refocusing pulses that achieve the same flip angle and phase across all the spins. In addition, it is difficult to make transmit and receive coils uniformly sensitive over the entire bandwidth. Shimming was done to decrease field variation<sup>6</sup>. The shimming method (similar to [68]) is describe below.

1. A “difference field map”,  $B_{diff}$ , is evaluated by subtracting the measure fieldmap

<sup>6</sup>No attempt was made to reshape the SEM.

( $B(x, y, z)$ ) from the the average field ( $B_{ave}$ ).  $B_{diff}(x, y, z) = B_{ave} - B(x, y, z)$ . These difference maps from several axial slices are shown in Figure 3-10a.

2. A configuration of small shim magnets (0.5" diameter, 0.25" length cylindrical NdFeB magnets) is estimated through simulation ( $B_{shim}$ ) to mimic  $B_{diff}$ . In yokeless magnet designs, the superposition of independently generated fields is valid. Therefore the shimming can be optimized by minimizing  $B_{diff} - B_{shim}$ .  $B_{shim}$  is illustrated in the Figure 3-10b for one shim magnet configuration (Figure 3-10d). The positions of shim magnets are determined in this way.
3. Shim magnets are attached to the magnet rungs, in the previously determined positions.
4. The field is remapped, and the process is iterated.

The field variation was shimmed down to  $\Delta f_{yz} = 32$  kHz,  $\Delta f_{xz} = 32.5$  kHz and  $\Delta f_{xy} = 19$  kHz. The 3 planes of the shimmed field map are shown in Figure 3-11. Shimming could be further improved by installing a mechanism for accurately positioning of shim magnets (a shim tray), as well as the use of smaller shim magnet.

## 3.6 Field Mapping - Field Probe Arrays

### 3.6.1 Background

The field mapping technique described in section 3.5 is not feasible in mobile applications. As we will see in later sections, an accurate field map is critical for image reconstruction, particularly when nonlinear encoding fields force the use of iterative matrix solvers rather than the Fourier transform [42]. The field is perturbed by external fields (including the earth's magnetic field), and must be remapped when the magnet is relocated.

Although there are several types of magnet sensor technologies [74], NMR probes are commonly used because of their naturally compatibility with MR and the ability to quickly measure inhomogeneous fields with high sensitivity [75], [76]. Generally,

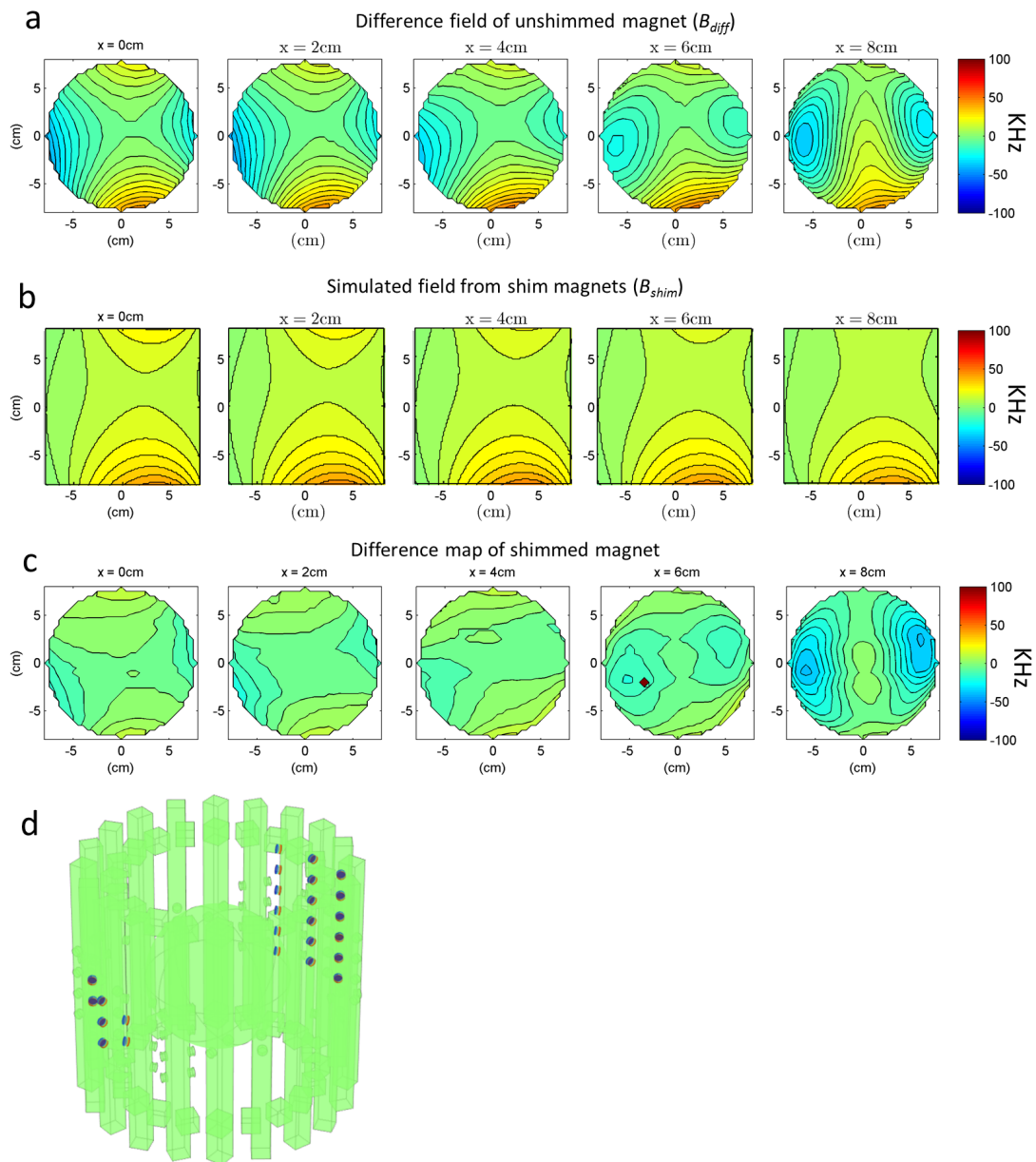


Figure 3-10: Illustration of shimming method. (a) The difference field is calculated by subtracting the measured field map from the average field ( $B_{diff}(x, y, z) = B_{ave} - B(x, y, z)$ ). The magnet is shimmed by estimating the distribution of small shim magnets that approximates the difference field. (b) The simulated field from the shim magnet arrangement in (d). (c) The difference field map is shown after the addition of shim magnets.

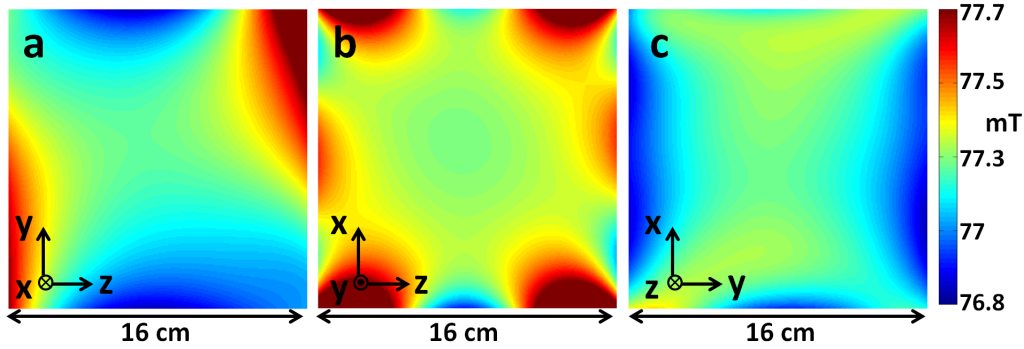


Figure 3-11: Measured Larmor frequency maps of the spatial encoding magnetic field (SEM) in the z-y (imaging plane), z-x, and y-x planes of shimmed Halbach magnet. The  $B_0$  field is oriented in the z direction.

small capillaries serve as a sample holder and coil former. Sensitive tuned solenoids are directly wrapped around the capillary allowing a high filling factor and therefore high SNR. At high fields, susceptibility mismatches between the sample and air may cause line-broadening in the acquired signal and a short-lived signal. To prevent this, special non-miscible liquid combinations with similar magnetic susceptibility are used for the sample and “susceptibility plugs” (for example, a cyclohexane droplet suspended in heavy water) [75]. The “susceptibility plugs” must also be MR invisible at the observation frequency of the sample. Luckily, at low-field strengths susceptibility matching with air is not an issue, and a simple droplet of water can be used inside a capillary. The probes are often located on the surface of a sphere so that a spherical harmonics model can accurately be used for field calculations [76].

### 3.6.2 2D Field Probe Array

Our first goal with the scanner was to obtain 2D images using a thin sample. For this goal, 2D field maps were sufficient. In order to quickly acquire center-plane field maps, a linear array of 7 field probes spaced 1.5 cm apart was constructed (Figure 3-12a). The field probes are tuned 5 mm long, 4 mm diameter, 18-turn solenoids measuring signal from 1 mm capillaries of copper sulfate ( $\text{CuSO}_4$ ) doped water.  $\text{CuSO}_4$  doping is done to decrease the T1 relaxation time and allow rapid averaging. To acquire a field map, the probes are held stationary while the magnet is rotated around them.

Polynomial basis functions are then fit to the measured points and the field map (Figure 3-12b) is synthesized. The polynomial coefficients up to 6th order of one magnet rotation angle are shown in Table 3.1.

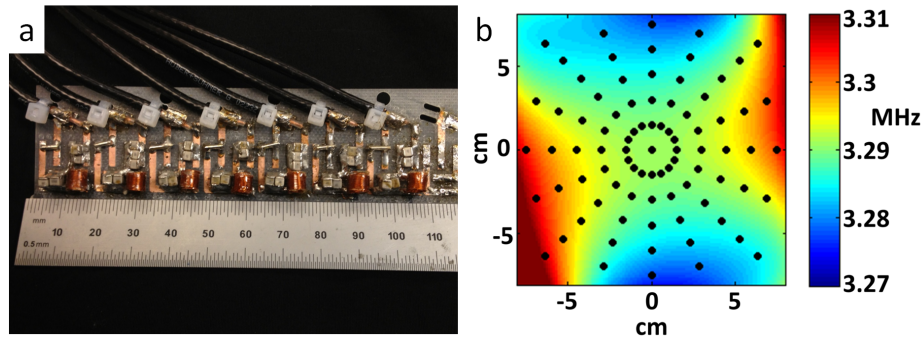


Figure 3-12: (A) Linear array of 7 NMR field probes used for mapping the static magnetic field. The probes are held stationary, while the magnet is rotated around them and points on the 2D center plane are sampled. (B) Measured field map for the center transverse slice through the magnet after fitting 6th order polynomials to the probe data. The black dots mark the location of the probe measurements. The field is plotted in MHz (proton Larmor frequency). This field distribution serves as the SEM information used in image reconstruction.

### 3.6.3 3D Field Probe Array

3D image encoding is an ongoing project for which we envision the use of  $B_1$  encoding fields along the  $x$  axis. To reconstruct 3D images, 3D field maps will be necessary. We have designed and fabricated an array of field probes in an 16 cm diameter circular configuration (Figure 3-13a-b). Previously, we rotated the Halbach magnet around a 1D linear array of probes to create the 2D field maps. By contrast, the magnet remains stationary as this circular array of field probes is rotated in increments of 15 degrees on a fiberglass rod that is coaxial to the Halbach cylinder. The field probe measurement locations are on “lines of longitude” on the surface of sphere. Spherical harmonics up to 4th order are fit to the acquired NMR frequency data to create 3D field maps (Figure 3-13c).

$z^n y^m$	$n = 0$	$n = 1$	$n = 2$	$n = 3$	$n = 4$	$n = 5$	$n = 6$
$m = 0$	$z^0 y^0 : 3.3e6$	$z^1 y^0 : -89$	$z^2 y^0 : -274$	$z^3 y^0 : 1.9$	$z^4 y^0 : 1.1e-2$	$z^5 y^0 : 2.4e-2$	$z^6 y^0 : 9.2e-3$
$m = 1$	$z^0 y^1 : -62$	$z^1 y^1 : 104$	$z^2 y^1 : -8.3$	$z^1 y^3 : -1.7$	$z^1 y^4 : -4.6e-2$	$z^1 y^5 : -1.8e-3$	
$m = 2$	$z^0 y^2 : 164$	$z^1 y^2 : -13.3$	$z^2 y^2 : -0.53$	$z^3 y^2 : -0.12$	$z^4 y^2 : 0.11$		
$m = 3$	$z^0 y^3 : 3.9$	$z^1 y^3 : 6.5$	$z^2 y^3 : 4.4e-2$	$z^3 y^3 : -2.3e-2$			
$m = 4$	$z^0 y^4 : 0.95$	$z^1 y^4 : 0.21$	$z^2 y^4 : -1.9e-2$				
$m = 5$	$z^0 y^5 : -3.9e-3$	$z^1 y^5 : -6.6e-2$					
$m = 6$	$z^0 y^6 : 9.2e-3$						

Table 3.1: Calculated polynomial coefficients composing the  $z - y$  plane (2D imaging plane) of the Halbach spatial encoding field in Hz/cm<sup>m+n</sup>. Measured points from the linear array of field probes (Figure 3-12) were used for this sixth order polynomial fit.

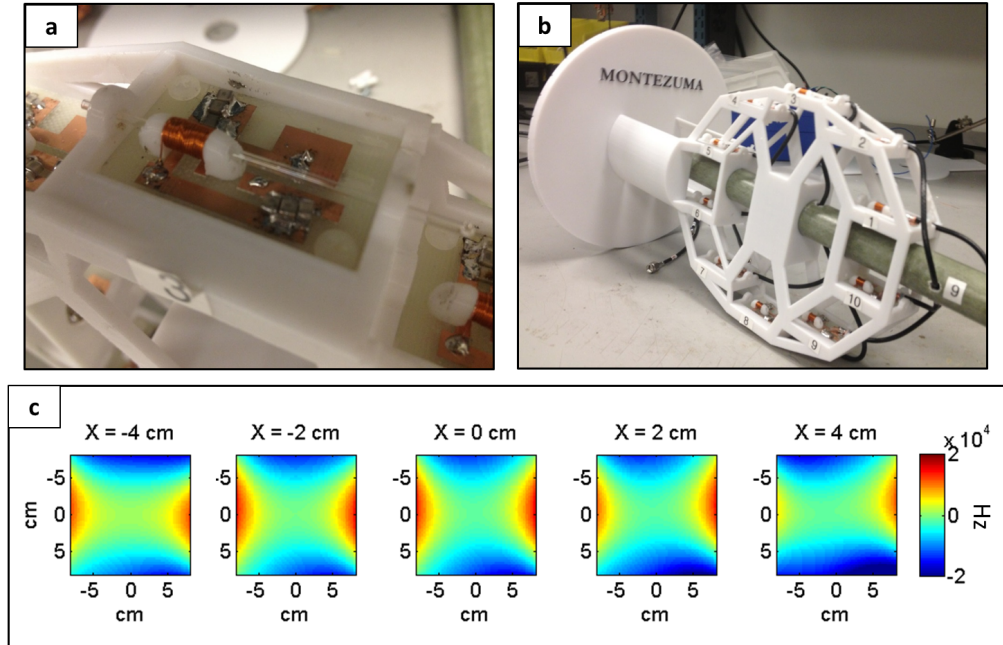


Figure 3-13: (A) A single field probe is shown, which consists of a tuned solenoid wound on a 3D printed former that also holds a 1.5 mm capillary tube. (B) The field probe array is shown, which consists of 10 field probes in a 16 cm diam. circular configuration. (C) 4th-order spherical harmonic fitting was used to produce these field maps slices along the  $x$  axis.

### 3.6.4 Field Drift Tracking

As described in section 3.1 (#5), NdFeB magnets have a significant temperature coefficient. Figure 3-14 shows a measured correlation between temperature inside the Halbach magnet and Larmor frequency over 12 hours. This was done by acquiring a FID from a field probe and a temperature reading from a thermocouple every 60 seconds. The correlation was about  $-3750 \text{ Hz}/^\circ\text{C}$  ( $-1140 \text{ ppm}/^\circ$ ), which is consistent with standard reversible temperature coefficient values for NdFeB magnets [24], [77]. In addition to drift with temperature, the net magnetic field from the NdFeB magnets is also sensitive to interactions with external fields such as the earth's magnetic field. To account for both of these things, an additional field probe is mounted to the Halbach array and rotated with magnet. This "field tracker" probe is used to monitor field changes,  $\Delta B_0$ , which may occur during acquisition or field mapping. The measured field changes during data acquisition are accounted for in the image reconstruction (see section 5.2).

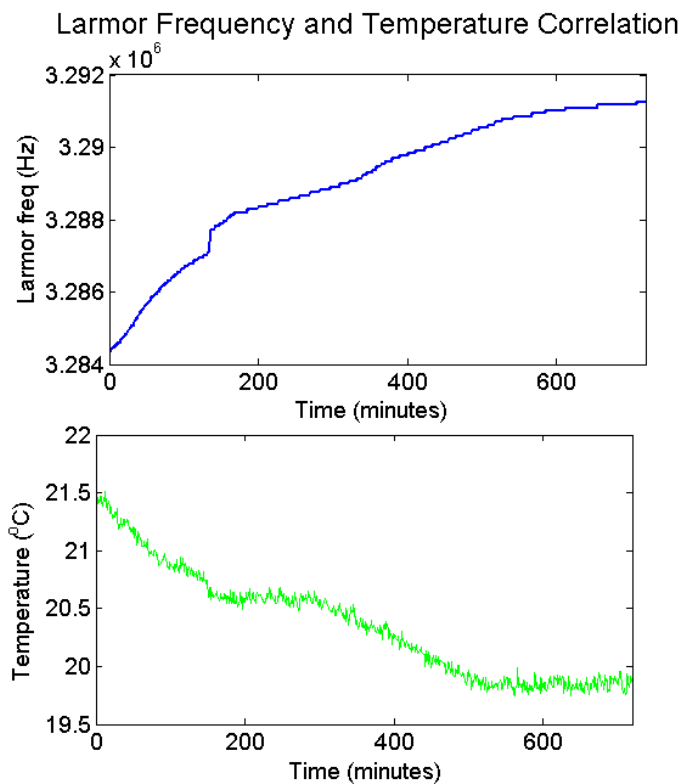


Figure 3-14: The NdFeB rare-earth magnets that comprise the Halbach array have a significant reversible temperature coefficient, which cause the net  $B_0$  field to change with temperature. The correlation was measured by acquiring an FID from a field probe and a temperature measurement inside the magnet every minute for 12 hours. The results show an average temperature coefficient of  $-3750 \text{ Hz}/^{\circ}\text{C}$  ( $-1140 \text{ ppm}/^{\circ}$ ).



# Chapter 4

## 2D Data Acquisition and RF Coils

### 4.1 Overview

Instead of acquiring lines of k-space, we acquire a set of data at each rotation angle of the magnet ( $\theta$ ). The dataset is a “projection” onto the Halbach magnet’s spatial encoding magnetic field (SEM) acquired from a spin-echo train. Just like the original 1973 Lauterbur experiment [1], rotation of the encoding field in relation to the object enables one dimensional projections of the object onto the encoding field. A series of one-dimensional projections at several rotation angles are then used to do a two-dimensional image reconstruction. In our case, generalized projections onto a nonlinear field are acquired (similar to those described in [78]), so the projection do not provide a linear mapping of position to frequency. Examples of these projections are shown in Figure 4-1 for a simple two-sphere phantom, where the projection plots are produced by an FFT of the time domain spin-echos. The gradient field experienced by the spheres changes at each rotation, providing new information in each projection.

There are unique challenges to the data acquisition method because the encoding field is always on and is non-bijective<sup>1</sup>. The static encoding fields force excitation and acquisition to be performed in a very inhomogeneous field (9878 ppm in the 16

---

<sup>1</sup>A bijective function has a one to one correspondence between elements of sets. Multi-polar encoding fields are considered non-bijective because there is not a one-to-one mapping between image space and frequency space.

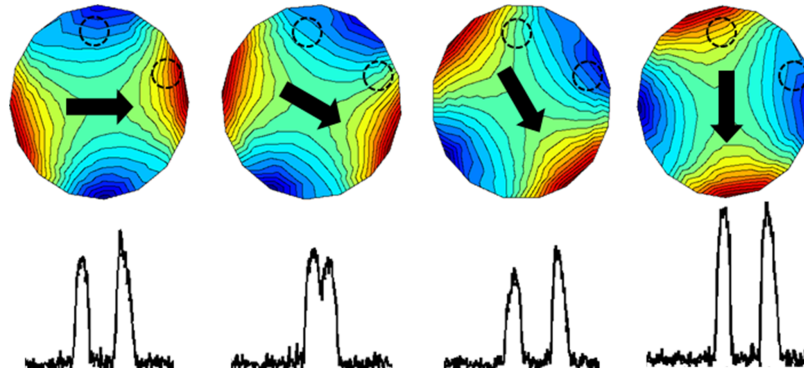


Figure 4-1: Schematic depiction of the generalized projections (bottom row) of an object onto the rotating SEM field. The object consists of two water-filled spheres depicted as dashed black lines which are superimposed on the Halbach magnet’s SEM field at a few rotations (black arrow depicts  $B_0$  orientation). The NMR spectrum was acquired with a single volume Rx coil.

cm circular FOV). This requires the use of broadband spin-echo sequences and low Q coils. The non-bijective field requires the use of multiple receive coils to resolve the aliasing.

At each rotation angle, a spin echo train is excited using broadband  $90^\circ$  and  $180^\circ$   $B_1$  pulses (typically  $25\mu\text{s}$  and  $50\mu\text{s}$  long) from a solenoid transmit coil and 1 KW power amplifier. An 8 channel array of surface coils are used to acquire data. A Tecmag Apollo console is used to transmit the excitation pulses and a single receive channel is used to acquire the data from the output of the pre-amplifiers. A Tecmag Apollo console is used with 1 RF transmit output, 1 RF receive input, and 3 gradient waveform lines<sup>2</sup>. Tecmag TNMR software is used to program the pulse sequences, and extra gradient lines are used to control a combination of Arduinos boards, op-amp drivers and relays to switch the console receive channel between the multiple receive coils, detune coils, and also control the motor driver for magnet rotation.

## 4.2 Pulse Sequences

The magnet is physically rotated around the sample in discrete steps, and subsets of data are acquired with the simple pulse sequence in Figure 4-3.

<sup>2</sup>Gradient coils are not used so these lines are used for other purposes

The spatial encoding magnetic field (SEM) is always on, and therefore the static magnetic field is very inhomogeneous. This causes a rapid loss of transverse phase coherence of the proton precession [79], and therefore a very short  $T2^*$  signal decay time constant (on the order of  $10\mu s$  for a large sample). Luckily the  $T2^*$  dephasing can be refocused with the application of a  $180^\circ$  pulse, producing a spin-echo signal. In conventional MRI scanners, gradient refocusing can also be used to refocus the signal, but this is impossible when gradients cannot be switched. Therefore the pulse sequences used for the Halbach magnet scanner consist of spin-echo trains (RARE-type sequences). For the same reasons, CPMG based sequences are also used in previously mentioned NMR devices operating in inhomogeneous fields [23], [80], [81], [26].

If an encoding field is linear, then the acquired signal is a radial spoke of conventional k-space. An analogous trajectory is traversed in the generalized k-space corresponding to the nonlinear SEM. The encoding field is always on, so immediately following the  $90^\circ$  pulse, the k-space trajectory of the FID moves out radially from the center. The  $180^\circ$  refocusing flips the current trajectory point about the center of k-space. Then the data acquisition window turns on, and data is acquired as the trajectory transverses the center of k-space radially.

When non-linear encoding fields are used, the conventional k-space formalism does not exist because the field gradient is different everywhere. The concept of “local k-space” can be used, in which distinct spatial frequency trajectories are defined throughout the object space. This concept will be revisited in Chapter 6.

Long spin-echo trains can be acquired with this system because at the low field strength  $T2$  is longer in vivo, and unlike in high-field systems, the specific absorption rate (SAR) from the consecutive  $180^\circ$  pulses is negligible because of the low excitation frequency (3.29 MHz). The echo trains can efficiently be used for signal averaging, partially offsetting the low-field SNR disadvantage. Typical acquisitions consist of trains of 16-64 spin echoes (depending on the sample  $T2$ ) with 6.4 ms readouts (256 points and 40 kHz) of each echo, at 181 rotation angles at 2 deg increments around the object, and repeated excitation for signal averaging when necessary.

The scanner pulse sequences are programmed in TNMR, the software that is

compliant with the Tecmag Apollo Console. A photo of the Apollo console and screen shot of a projection in TNMR is shown in Figure 4-2. A simplified pulse sequence diagram for a single rotation index ( $r$ ) is shown in figure 4-3, which shows a spin echo train sequence ( $90^\circ, 180^\circ, 180^\circ, 180^\circ, 180^\circ\dots$ ) while the encoding field is always on. At each magnet rotation, the sequence is repeated, and the SEM shape changes with respect to the sample.

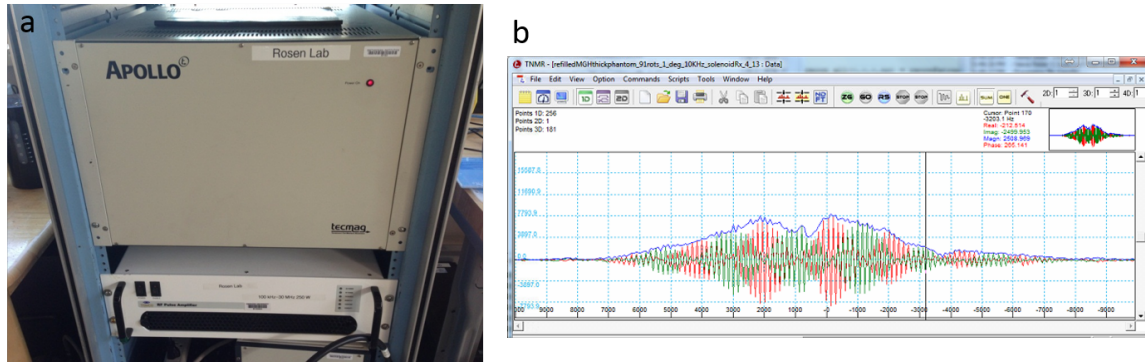


Figure 4-2: (a) Photo of the Tecmag Apollo console and Tomco RF power amplifier. (b) Screenshot of an experimental projection in the TNMR software, formed by an averaged train of spin-echos.

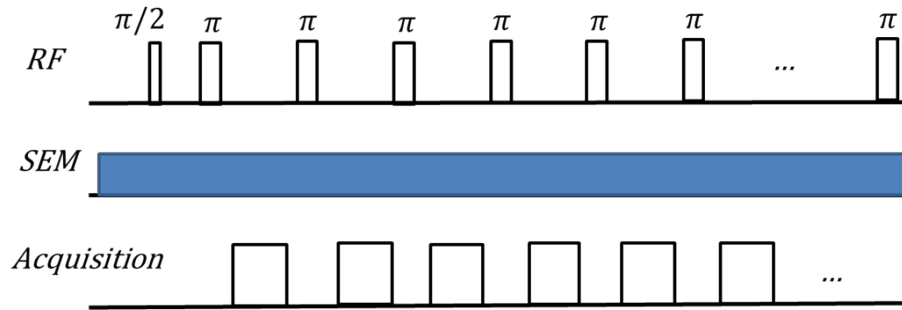


Figure 4-3: A simple pulse sequence diagram is shown for the spin-echo train, which is a  $90^\circ$  excitation pulse followed by a series of  $180^\circ$  refocusing pulses. The encoding magnetic field (SEM) is always on during the acquisition because it is produced by permanent magnets. However, the shape of the SEM changes in relation to the object with each magnet rotation.

This basic pulse sequence is very simple because there are no gradient pulses to program; instead our non-linear gradient field is always on. However, the additional programmable console lines such as the analog gradient outputs and scope trigger lines are necessary for controlling the ancillary hardware for RF coil switching, detuning,

and magnet rotation. The magnet rotation must be synched with the pulse sequence, so one of the analog gradient line ( $G_z$ ) is connected to the motor driver (Anaheim Automation MLA 10641) to control the magnet rotation. Another gradient line ( $G_x$ ) is used for coil array switching and detuning (see section 4.5).

The basic spin-echo train pulse sequence in figure 4-3 can be used to produce proton density (PD), T2, and T1 weighted images. The images that have been acquired so far have been mostly PD with some T2 weighting (short TE). T2 contrast can be emphasized however by increasing the time between the 90° and the first 180° excitation pulse (long TE). T1 contrast can be acquired by beginning the sequence with a 180° inversion pulse, like common inversion recovery prepped sequence (IR, Turbo IR, STIR, FLAIR) [79].

## 4.3 Excitation Method

### 4.3.1 Broadband Excitation

In addition to the use of spin-echo refocusing, NMR experiments in inhomogeneous fields also require broadband excitation pulses because the wide magnetic field variation causes a wide Larmour frequency range.

The default method for exciting a wide frequency band is short rectangular shaped pulse played at the center Larmour frequency (hard pulses). A hard pulse of length  $T$ , has a sinc shaped frequency profile with the first zero crossing at  $1/T$ . The FWHM (full-width at half max) range is  $1.21/T$  [82]. Assuming, a homogeneous  $B_1$  field, the flip angle produced by a hard pulse is simply:

$$\theta = \frac{\gamma}{2\pi} B_1 T. \quad (4.1)$$

The 2D images shown in chapter 5, were acquired using a 1 KW power amplifier (Tomco, Stepney, SA, Australia). Short 25  $\mu$ s 90° pulses and 50  $\mu$ s for 180° pulses were transmitted at 600W for broadband excitation<sup>3</sup>. This hard pulse method is

---

<sup>3</sup>It is questionable if true 180° pulses were excited across the entire bandwidth though

simple and works well in cases without power limitations. For example, the NMR MOUSE can produce  $180^\circ$  flip angles with  $2\mu\text{s}$  pulses at 100-300W [27]. However, similar to well-logging instruments our excitation bandwidth is limited by the available RF amplitude [83]. This RF amplitude is limited by the power available from the RF power amplifier and the amount of power that the RF coil can tolerate before arcing. In addition, power reflection from the transmit coil has been problematic. This may be a result of a small coil bandwidth compared to the frequency content of the transmitted RF pulse. Currently, we are exploring the use of wide bandwidth pulses that require less peak power such as composite pulses [84], [85] or frequency swept pulses [86], [87]. A recently publication presents the use of chirped pulses in a CPMG chain for inhomogeneous NMR well-logging applications [88], which is very relevant to our application.

### 4.3.2 Excitation Coil

Unlike conventional MRI scanners, the  $B_0$  field of the Halbach magnet is oriented radially instead of along the bore of the magnet. This means that in order for  $B_1$  to be orthogonal to  $B_0$  at all rotations, it should be directed along the cylindrical axis of the Halbach magnet. This makes a solenoid more suitable than a birdcage coil for RF excitation. The constructed solenoid, shown in Figure 4-4a, has a 20 cm diameter and a 25 cm length.  $N = 25$  turns of AWG 20 was chosen as a reasonable value in the trade off between  $B_1$  homogeneity and parasitic capacitance from closely spaced windings. The 70  $\mu\text{H}$  Tx coil is tuned to 3.29 MHz with eight 230 pF series capacitors distributed along the length of the solenoid, which reduces the susceptibility to stray capacitance. Because the static SEM field is always on, the transmit coil must have a relatively low Q in order to excite a wide bandwidth of spins. The Q of the coil is about 60 corresponding to a 55 KHz bandwidth.

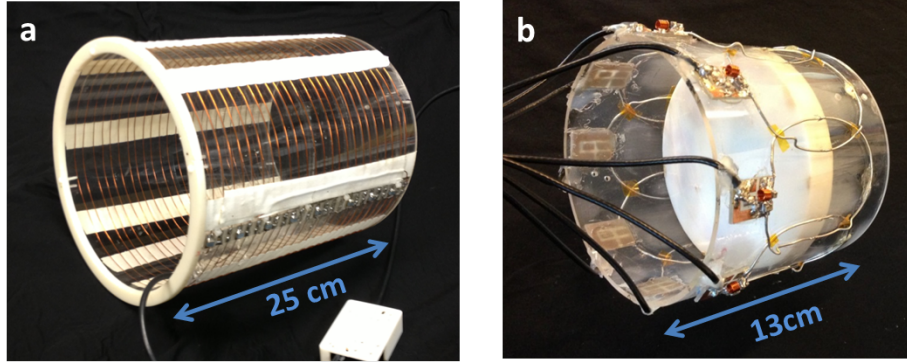


Figure 4-4: (a)Photo of the 25 turn, 20 cm diameter, 25 cm length solenoid transmit coil. (b) Photo of the 8 channel receiver array coil with 3D printed disk-phantom at isocenter. The 14 cm diameter array is made up of eight, 8 cm loops overlapped to reduce mutual inductance.

## 4.4 Rx Coil Array

The constructed Halbach magnet’s spatial encoding field is approximately quadrupolar and therefore produces a non-bijective mapping between object space and encoding space. This encoding ambiguity leads to aliasing across the center onto the frequency matched isocontours. This same aliasing behavior occurs in all multipolar encoding fields such as those originally described by Hennig et al. in 2008 [41]. The described “Parallel Imaging Technique with Localized gradients” (Patloc) uses multiple encircling receive coils to disambiguate the non-bijective mapping. This is possible because the coil sensitivity profiles provide additional spatial encoding that localizes signal within each source quadrant of the FOV, eliminating aliasing. Our implementation of projection imaging in an approximately quadrupolar encoding field closely resembles the case of PatLoc imaging with quadrupolar fields and a radial frequency-domain trajectory (Schultz, et al., 2011).

Parallel imaging is often done with receive coil arrays made up of surface coils. These coil arrays are commonly used for accelerated parallel reconstruction techniques, like SENSE [89] and GRAPPA [90], [91]. SENSE is a reconstruction technique in which the coil sensitivities are used to un-alias undersampled images. Similarly, coil sensitivity profiles can be used to un-alias data acquired with a non-bijective gradient field, which is a common theme in nonlinear gradient imaging

techniques [41], [92], [93], [94], [95]. The general design procedure of receiver coil arrays for parallel imaging techniques have been optimized over the years [96], [97].

MRI receive coils are tuned to the resonant frequency of the system ( $f_0 = \frac{\gamma}{2\pi} B_0$ ) to increase their sensitivity to the MR signal. In the classic design, the output impedance of the coil is matched to the pre-amplifier impedance of  $50\Omega$  for efficient power transfer and to minimize noise [98]. This is not the case in modern parallel imaging receive arrays that use pre-amplifier decoupling to prevent coupling between the coils in the receive array [99]. Pre-amp decoupling is achieved by limiting the current in the receive coils and therefore the mutual inductance and coupling. This is done by using a low input impedance pre-amplifier which effectively shorts a series inductor across a tuning capacitor in the coil loop. This LC circuit is tuned to the resonate at the Larmor frequency, and appears as a high impedance in the current path.

The constructed Rx coil array (Figure 4-4b) consists of eight 8 cm diameter loops of wire encircling the FOV on the surface of a 14 cm diameter cylinder. The inductances of the coils are roughly 230 nH, requiring capacitors on the order of 10 nF (Voltronics, Salisbury, MD) for tuning. Appropriate low-impedance pre-amplifiers that operate at 3.29 MHz are unavailable, so geometric decoupling and PIN diode detuning are implemented instead of pre-amp decoupling (see Section 4.5). The coils are tuned and matched to 50 Ohm impedance low noise pre-amplifiers (MITEQ P/N AU-1583, Hauppauge, NY).

#### 4.4.1 Coil sensitivity profiles

The coil sensitivity profile is a measure of how sensitive the coil is to signal coming from each point in the imaging field of view. Volume coils, like solenoids, have a fairly uniform sensitivity profile. Surface coils, which are usually a single loop of wire that sit on the surface of the object, have non-uniform complex valued sensitivity profiles.

Two scanner coordinate systems are defined because the object and RF coils remain stationary while  $B_0$  is rotated. The rotating coordinate system of the magnet and the spins is defined as  $x', y', z'$  (examples shown in Figure 4-5b), and fixed coordinate system for the coils and objects is defined as  $x, y, z$ . Image reconstruction

requires accurate knowledge of the coil sensitivity map,  $C_{q,r}(x)$ . Here the index  $q$  refers to the coil channel and  $r$  to the rotation position of the magnet. The coil sensitivity map is different for each rotation position since  $B_1^-$  is formed from a projection of the coil's  $B_1$  field onto the  $x' - y'$  plane (which rotates with the magnet). In conventional MRI,  $B_1^-$  is mapped by imaging the object or a phantom with fully sampled encoding by the gradient waveforms. However, this approach is not possible with our encoding scheme because knowledge of  $C_{q,r}(x)$  is necessary to form an image without aliasing.

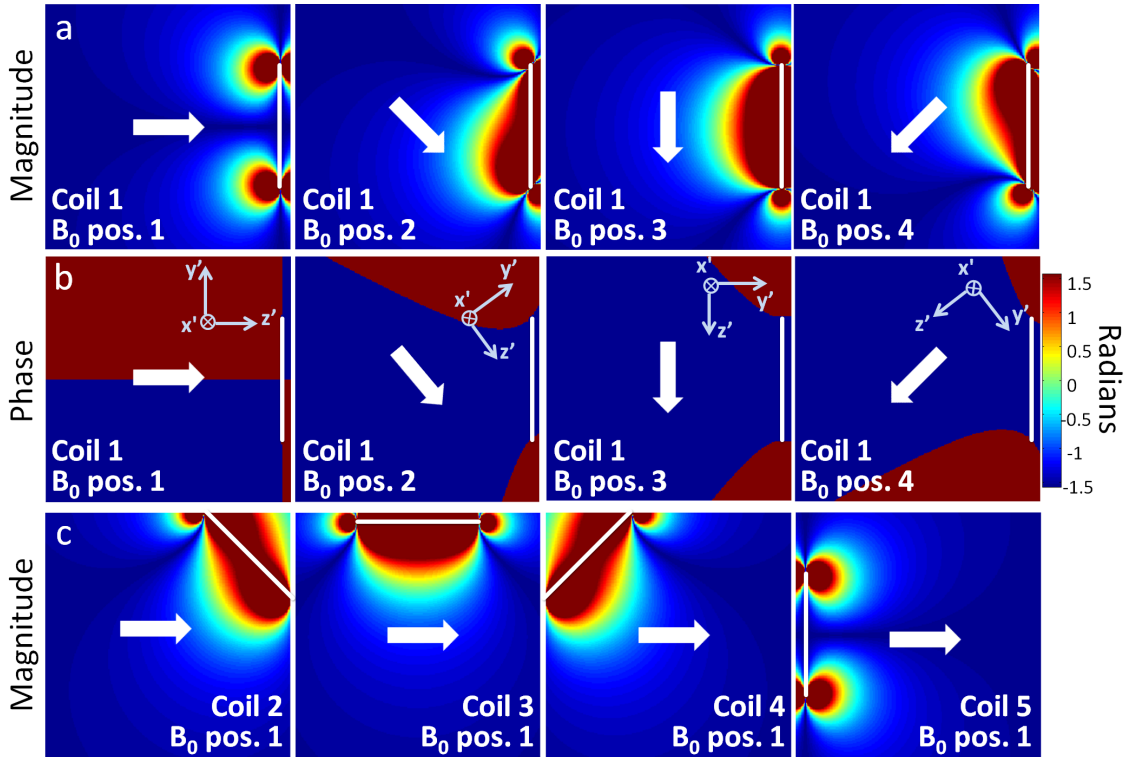


Figure 4-5: Biot-Savart calculation of the sensitivity map of the Rx coil array. The white arrows show representative orientations of  $B_0$ , which define the spin coordinate system orientation  $(x', y', z')$ . Image reconstruction requires accurate coil sensitivity profiles for each  $B_0$  angle used in the experiment. (a-b)  $B_1^-$  magnitude and phase for a single representative surface coil located at the right side of the FOV (position marked with white line). Because of the symmetry of the coils' at isocenter, the coils'  $x'$  component is always zero, and the process of taking the projection onto the  $x' - y'$  plane (to solve for  $B_1^-$ ) will produce a vector parallel or anti-parallel to  $y'$ . Therefore, the  $B_1^-$  phase is always  $+90^\circ$  or  $-90^\circ$  in the depicted transverse isocenter plane. (c)  $B_1^-$  magnitude of 4 different coils of the array (marked with white lines) for a single magnet rotation position.

Because of the difficulty of measuring  $B_1^-$  on our scanner, we use estimated  $B_1^-$  maps. Magnetostatic approximations are suitable at the 3.29 MHz Larmor frequency, so  $B_1$  of the individual coils was modeled with Biot-Savart calculations. By symmetry, the  $x$  component of the circular surface coils'  $B_1$  is zero in the center plane FOV. The  $x'$  component  $B_0$  is also nearly zero because of the geometry of the magnet. So the coil sensitivity calculation reduces to a two dimensional problem, since only the  $B_1$  component perpendicular to  $B_0$  contributes to the sensitivity map.

To calculate the coil sensitivity map for each rotation ( $r$ ), the  $B_1$  component parallel to  $B_{0,r}$  (the  $B_0$  vector for rotation  $r$ ) is subtracted and we are left with the perpendicular component.

$$B_{1r}^\perp = B_1 - (B_1 \cdot B_{0,r})B_{0,r} \quad (4.2)$$

The phase is equal to the angle,  $\theta_r$ , between  $B_{1r}^\perp$  and  $B_{0,r}$ , which will either be  $+90^\circ$  or  $90^\circ$  due to the symmetry properties discussed above. The variation in a single coil's  $B_1^-$  as a function of  $B_0$  angle is illustrated in Figure 4-5a-b, and the  $B_1^-$  magnitude for 4 coils and a single  $B_0$  angle is shown in Figure 4-5c. When  $B_0$  points along the normal to the coil loop, the sensitivity profile resembles a “donut” pattern with low sensitivity in the center of the FOV. Maximum signal sensitivity occurs when  $B_0$  is oriented orthogonal to the normal vector of the coil loop.

#### 4.4.2 Rotating Rx coils

In the described experiments the  $B_0$  field rotates relative to the receiver coils (coils are stationary), which causes the shape of the coil profiles to change with each acquisition angle. However this arrangement is not a requirement for rSEM imaging, and in theory the receiver coils could rotate with the magnet. In this case, the coil sensitivity profiles are simply rotated for each acquisition angle, but the shapes of profiles do not change. Data acquisition with rotating coils and stationary coils was simulated and are shown in Figure 4-6 (simulation method are described in Chapter 6). However, there was not a significant difference in performance in either the visual appearance of

the reconstructed images or the RMSE (root mean squared error). For data simulated with 91 magnet rotations there was a 0.2% RMSE improvement when using the rotating coil profiles, and for data simulated with 23 magnet rotations there was a 3.6% RMSE improvement. This suggests that the rotating coil array may improve performance modestly when data is “undersampled”. The rotating receive coil case is similar to the RRFC (Rotating RF Coils) method described in [100], [101], where continuously rotating surface coils are used in a conventional magnet for parallel imaging. The same group has also introduced a rotating RF coil method for encoding without conventional gradient coils [102].

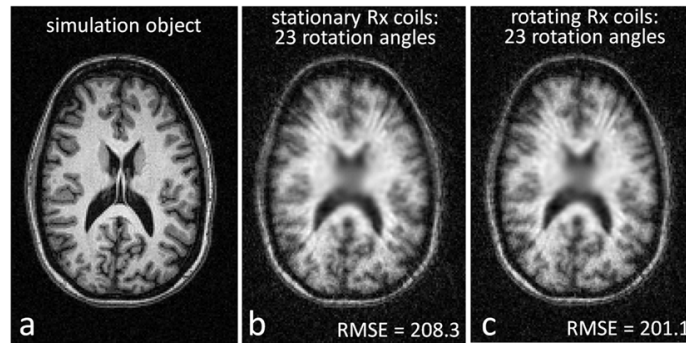


Figure 4-6: Simulated images comparing the performance of rotating and stationary receiver coil arrays in the rotating Halbach magnet. Data was simulated using 23  $8^\circ$  rotations of the encoding field and 6.4 ms, 256 point readouts. The model data was then reconstructed using the Algebraic Reconstruction Technique in a 16 cm FOV. (A) Reference high resolution 3 T T1 weighted brain image used as the model object. Note: the SEMs were scaled to the brain FOV. (B) Simulated reconstruction with added noise using stationary coil profiles (same as experimental setup). The root mean squared error (RMSE) of the simulated image compared with the reference image is 208.3. (C) Simulated reconstruction with added noise using coil profiles that rotate with the magnet, RMSE = 201.1. Compared to brain simulations in Figure 6-7, these simulated images contain more artifacts because the data was undersampled (23 magnet rotations versus 181 rotations).

## 4.5 RF Coil Decoupling and Switching

### 4.5.1 Theory

Coupling between the closely spaced coils tuned to the same frequency must be addressed during the coil design. The mutual inductance between coils causes resonant peak splitting and signal and noise coupling. For the receive coils, resonant peak splitting causes the pre-amplifier noise match to be poor which results in decreased SNR. In addition, signal coupling between the coils increases their linear dependence, which limits the spatial encoding ability of the coil array [103].

The coupling between adjacent coils in the receive coil array is greatly reduced by geometric decoupling, which is achieved by overlapping adjacent coils to eliminate mutual inductance. Geometric decoupling was achieved in our receive coil array by finely adjusting the overlap of adjacent coils until the measured  $S_{12}$ <sup>4</sup> of the two coils was minimized. The resulting overlap is about 2 cm (25% of diameter). Unfortunately, there is significant coil coupling between non-adjacent coils as well, which is commonly managed by “pre-amplifier decoupling” [96] in parallel imaging. Pre-amplifier decoupling is achieved with the combination of a low-impedance pre-amplifier and LC circuit to effectively add a high-impedance to coil and therefore reduce current and mutual inductance. Pre-amplifier decoupling is not used in our system yet, but will be added when true parallel imaging is implemented (section 8.2.4). Instead, we use PIN-diode detuning to prevent coupling.

PIN-diode detuning is achieved by somehow breaking the resonant circuit in the tuned coil with a PIN-diode [104]. This usually causes the coil to resonate at a much higher frequency, which greatly reduces the coupling with other coils tuned the original Larmor frequency. PIN-diodes appear as a short circuit when properly biased with +100 mA (with a console controlled DC voltage), and appear as an open circuit when they are un-biased or negatively biased. Generally, in parallel imaging systems, pin-diode detuning is used to break the surface coils’ resonant circuit during excitation pulses which is important for protecting the sensitive pre-amplifiers and

---

<sup>4</sup>S-parameter measured with a network analyzer that indicates the level of coil coupling.

preventing SAR hotspots [99].

Although, it would be far more time efficient to acquire data from the coil array in parallel, the console hardware limitations require serial data acquisition from the receiver coils. This means that the RF coils (including the transmit coil) are never used simultaneously, and during the pulse sequence all except one coil can be detuned. The single console receiver channel must also be switched between the coils as data is acquired in series.

## 4.5.2 Implementation

### Coil Detuning

Figure 4-7 shows the basic surface coil circuit. A Mini-Circuits bias tee (ZFBT-4R2GW-FT+) is connected between the surface coil and low noise MITEQ pre-amplifiers (P/N AU-1583) to direct the DC bias to the PIN-diode.

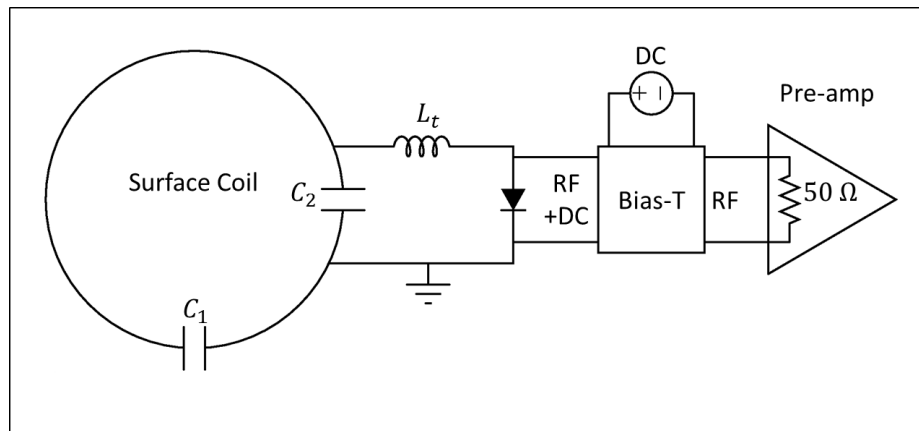


Figure 4-7: A schematic of the surface coil circuit is shown. Capacitors  $C_1$  and  $C_2$  are used with the inductance of the loop coil to tune and match the coil to  $50\ \Omega$  at 3.29 MHz. This means that the combined imaginary impedance is 0 and the real impedance is  $50\ \Omega$  at 3.29 MHz. The inductance of  $L_t$  is chosen to resonate with  $C_2$  at 3.29 MHz. When the PIN-diode is forward-biased,  $L_t$  and  $C_2$  form a parallel LC circuit and introduce a series high impedance to the coil, which detunes it. The PIN-diode bias is introduced by a bias-tee, which directs console controlled DC current to the diode.

When the surface coil is not in use, the PIN diode should be “on” (positively biased), creating a parallel LC circuit with  $L_t$  and  $C_2$ . The inductance,  $L_t$ , is chosen

to resonate with  $C_2$  at the Larmor frequency, which effectively adds a high impedance in the loop and detunes the coil.

Each surface coils' DC bias is controlled by the analog level of the Gx gradient from Apollo console. The amplitude of the Gx line is set in the pulse sequence to correspond to a receiver coil channel and is connected to the analog input of an Arduino Uno board. The Arduino board is programmed to associate defined Gx amplitude ranges with a specific digital output. For example, when  $G_x = 0.5$  V, digital output 1 is set high and the rest are low, and when  $G_x = 2$  V, digital output 4 is set high and the rest are low, etc. The eight Arduino outputs that are assigned to the eight surface coils are buffered and amplified by an inverting op-amp circuit and then connected to the DC input of the bias tees. Therefore, when the Gx level is programmed to an associated surface coil level, the DC input to that coil's bias-tee is negative and the PIN diode is "off" (coil is tuned). The other inverting op-amp circuits output a positive bias by default, causing all the non-selected coils to be detuned.

## **Coil Switching**

The individual pre-amplifier outputs are connected to a 10 input 1 output relay (10 pole, single throw), which passes one of the inputs to the Apollo receiver channel (ADC). The RelComm Technologies (Salisbury, MD) relay has 10 TTL control inputs which determine which input is passed to the output.

In addition to controlling the detuning/tuning of the coils, the Gx line (plus Arduino board) is also used to produce the TTL control lines in a similar way. The Gx amplitude controls the digital outputs of the Arduino board which are each associated with a single coil of the array. The digital outputs are boosted with the recommended relay driver to provide the TTL pulses that switch the relay.

# Chapter 5

## Image Reconstruction

The use of non-linear spatial encoding magnetic fields (SEM) and the associated spatially-varying k-space coverage and resolution of each voxel prevents the use of conventional 2DFT reconstruction. Instead the acquired signal is modeled by calculating the expected phase accumulation of the spins at each voxel over time. This phase accumulation is calculated for each magnet rotation and receiver coil and incorporated into an encoding matrix ( $\mathbf{E}$ ). The encoding matrix is constructed so that the product of the the encoding matrix and the estimated image (in vector form) is the acquired signal (in vector form). This matrix model is used to find the least-squares optimal estimator for the unknown image.

### 5.1 Signal Equation

The basic signal equation for a single projection (one magnet rotation angle) acquired with a uniform RF coil is Eq. 5.1, where  $s$  is the signal acquired over time  $t$ ,  $\phi$  is the phase of the precessing spins at each location  $\mathbf{x}$ , and  $m$  is the object's magnetization at each location  $\mathbf{x}$ .

$$s(t) = \int_x e^{-i\phi(\mathbf{x},t)} m(\mathbf{x}) dx \quad (5.1)$$

Image reconstruction is the process of solving for the unknown object or image,

$m(\mathbf{x})$ . Depending on the acquisition pulse sequence, the magnetization  $m$  may be the density of protons or it may include some relaxation (T1, T2) contrast. The magnetization is modulated by the spatial encoding magnetic fields (SEM) at each rotation. The SEM causes slight variations in the precession frequency (Larmour frequency) of the spins over space  $f(\mathbf{x}) = \frac{\gamma}{2\pi} B_{SEM}(\mathbf{x})$ . For the spin echo pulse sequence, immediately after the  $90^\circ$  and in the center of the spin echo formation, the spins are in phase and  $\phi(\mathbf{x}) = 0$  (assuming ideal RF excitation). Then phase differences accumulate over time because of the frequency variation,

$$\phi(\mathbf{x}, t) = f(\mathbf{x})t = \frac{\gamma}{2\pi} B_{SEM}(\mathbf{x})t. \quad (5.2)$$

According to equation 5.1, at time  $t$ , the signal  $s$  (detected uniformly over the object) is the integral of the object magnetization,  $m(\mathbf{x})$ , modulated by the phase of the magnetization precession,  $\phi(\mathbf{x})$ , over space,  $\mathbf{x}$ .

The acquired signal is discretized into  $N_{\text{readout}}$  samples by the console ADC, and the image is discretized into  $N_{\text{voxels}}$  voxels. This discretized version of the signal shown in equation 5.3,

$$s(t) = \sum_{\mathbf{x}} e^{-i\phi(\mathbf{x}, t)} m(\mathbf{x}), \quad (5.3)$$

can easily be expressed in matrix form:

$$\mathbf{S} = \mathbf{E}\mathbf{m}. \quad (5.4)$$

The encoding matrix,  $\mathbf{E}$ , contains the predicted phase of each voxel in the image field of view (FOV) for each time point in the acquisition. The multiplication of each row of the encoding matrix with  $\mathbf{m}$  corresponds to one readout point. With linear gradient fields,  $\mathbf{E}$  is made up of a sinusoidal Fourier basis set, which allows the image to be reconstructed with the 2D or 3D Fourier transform. In the nonlinear gradients case,  $\mathbf{E}$  is more complicated, but can be calculated from the appropriate SEM field maps.

So far the signal equation has been described for a uniform receive coil and a single projection. However, an array of coils (number of coils =  $N_c$ ) will generally be used to acquire projections at several rotations (number of rotations =  $N_{\text{rots}}$ ).

The discretized signal acquired by a single coil ( $q$ ) at a given magnet rotation increment ( $r$ ) at time  $t$  is:

$$s_{q,r}(t) = \sum_{\mathbf{x}} C_{q,r}(\mathbf{x}) e^{-i\phi_r(\mathbf{x},t)} m(\mathbf{x}), \quad (5.5)$$

where  $C_{q,r}(\mathbf{x})$  is the complex spatial sensitivity of the coil, and  $\phi_r(\mathbf{x},t)$  is the evolved phase from the SEM for rotation index  $r$ , location  $\mathbf{x}$ , and time  $t$ . The coil sensitivity profiles vary with rotation angle because the direction of  $B_0$  is changing relative to the vector RF magnetic field of the coils (see section 4.4.1). The phase term and coil sensitivity term can be grouped together to form the encoding function:  $enc_{q,r}(\mathbf{x}, t)$ .

$$s_{q,r}(t) = \sum_{\mathbf{x}} enc_{q,r}(\mathbf{x}, t) m(\mathbf{x}) \quad (5.6)$$

The matrix form of this signal equation 5.6 is:  $\mathbf{S}_{q,r} = \mathbf{E}_{q,r} \mathbf{m}$ , which is visually depicted in Figure 5-1.

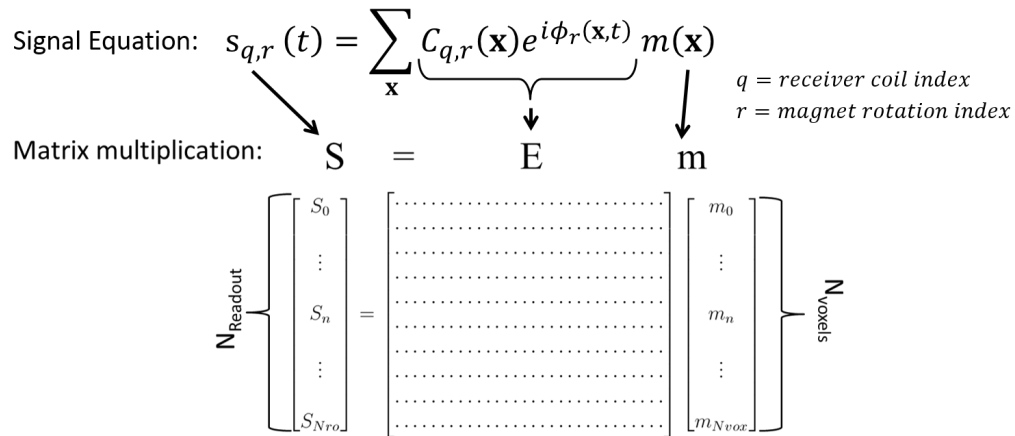


Figure 5-1: Matrix form of the signal equation for a single projection at magnet rotation,  $r$ , and acquired by a single surface coil,  $q$ . The acquired signal,  $\mathbf{S}_{q,r}$ , is a vector made up of the sampled readout points  $N_{\text{readout}}$ . The object that we are solving for,  $\mathbf{m}$ , is a vector made up of all the image voxels ( $N_{\text{voxels}}$ ).

A separate block of the encoding matrix,  $\mathbf{E}_{q,r}$  is calculated for the data acquired by each coil at each rotation. There will be a total of  $N_{\text{rots}} \times N_c$  blocks, which are vertically concatenated to form the full encoding matrix,  $\mathbf{E}$ .  $\mathbf{S}$  is also made up of vertically concatenated subparts,  $\mathbf{S}_{q,r}$ , which are the signals acquired from each coil at each rotation.<sup>1</sup> The full encoding matrix size is  $(N_{\text{readout}} \times N_{\text{rots}} \times N_c) \times (N_{\text{voxels}})$ . In the typical case of 256 readout points, 181 rotations, 8 coils and a  $256 \times 256$  voxel reconstructed image, the full matrix size is  $371\text{K} \times 65\text{K}$ .

## 5.2 Encoding Matrix Calibration

The encoding matrix,  $\mathbf{E}_{q,r}$ , is a forward model which represents the imaging process. As shown in Figure 5-1 it contains the evolved phase of each voxel in the FOV for each time point in the acquisition as well as the coil sensitivity multiplier, and can be calculated with knowledge of the encoding scheme and RF coil profiles. Accurate calibration of the encoding matrix is crucial to image reconstruction.

### 5.2.1 Coil sensitivity weighting

$C_{q,r}(\mathbf{x})$  comes directly from the complex valued sensitivity distribution of each of the surface coils in the Rx coil array (section 4.4.1). The theoretical three dimensional magnetic field produced by each of the coils when driven with a DC current was calculated with the Biot-Savart law and stored. Based on the exact  $B_0$  angles used in a given imaging experiment, the sensitivity profiles of each coil are calculated for each magnet rotation to give  $C_{q,r}$  during the encoding matrix calculation.

### 5.2.2 SEM induced phase

$\phi_r(\mathbf{x}, t)$  is determined by the SEM experienced by the object at the given rotation angle, and is calculated by equation 5.2. It is practically challenging to calculate an accurate  $B_{SEM,r}(\mathbf{x})$  for each rotation angle. As described in section 3.6, field probe

---

<sup>1</sup>The actual ordering of the rows does not effect the reconstructed image, but might have an effect of the iterative reconstruction rate of convergence.

arrays are used to quickly map the SEM. However, the effects of field changes during the acquisition must be accounted for (from external fields like the earth’s magnetic field and field drift with temperature). The “field tracking” probe (mounted to the magnet) measures these global  $B_0$  changes as a function of magnet rotation angle (section 3.6.4) during field mapping ( $B_{offset}(\psi)$ ) and data acquisition ( $B_{offset}(\theta(r))$ ), where  $\psi$  is the magnet rotation angle during fieldmapping and  $\theta(r)$  is the magnet rotation angle for each rotation index,  $r$ , during imaging experiments. Since the earth’s magnetic field contribution is known at each rotation angle, deviations from this expected sinusoidal field variation are assumed to arise from temperature drift. An experimental example of  $B_{offset}(\theta(r))$  is shown in figure 5-2 in Larmor frequency variation.

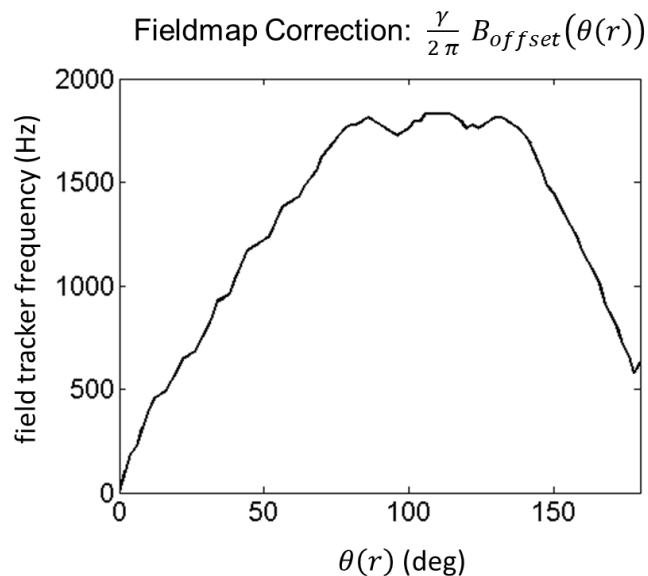


Figure 5-2: Experimental offset frequencies tracked with the “field tracking” NMR probe which is fixed to the magnet during data acquisition. An FID was acquired at each magnet rotation angle to track  $B_{offset}$  from temperature drift and external magnetic fields (i.g. earth’s field). These offset values are added to the rotated field maps that are used to calculate the encoding matrix.

The field mapping measurements are collected by rotating the magnet while the field probes remain stationary. The measurements from the field probe array (7 probes spaced by 1.5 cm along the magnet’s radius) at each angle are  $B_{fp1}(\psi)$ ,  $B_{fp2}(\psi)$ ,

$B_{fp3}(\psi)$ , etc. The baseline field probe measurements used for  $\mathbf{E}$  calibration are formed by subtracting the tracked field changes,  $B_{fp1}(\psi) - B_{offset}(\psi)$ ,  $B_{fp2}(\psi) - B_{offset}(\psi)$ ,  $B_{fp3}(\psi) - B_{offset}(\psi)$ , etc.

Based on the exact magnet rotation angles used for the imaging experiment,  $\theta(r)$ , the baseline field mapping probes' measurement positions are rotated and then polynomials are fit to form the appropriately rotated 2D field maps,  $B_{SEM,r}(\mathbf{x})$ . Then, the appropriate  $B_{offset}(\theta(r))$  (measured by the field tracking probe during data acquisition) is added to the rotated field map as a global offset. These corrected field maps are used to calculate the phase term,  $\phi_r(\mathbf{x}, t)$ , in the encoding matrix.

$$\phi_r(\mathbf{x}, t) = f_r(\mathbf{x})t = \frac{\gamma}{2\pi}(B_{SEM,r}(\mathbf{x}) + B_{offset}(\theta(r)))t. \quad (5.7)$$

### 5.3 Iterative Reconstruction Methods

To recover the object information from the acquired signal, linear image reconstruction can be performed because of the linear relationship between the acquired signal and the magnetization. The linear reconstruction problem can be described with simple matrix-vector operations. The direct method involves the calculation of a reconstruction matrix,  $\mathbf{F}$ , where the image  $\mathbf{m}$  is solved like:  $\mathbf{m} = \mathbf{F}\mathbf{s}$ .

The straightforward way to solve for  $\mathbf{F}$  is a matrix inverse of  $\mathbf{E}$ , often solved for with a Moore-Penrose Pseudo Inverse [105]. However, the use of multiple receiver coils results in large encoding matrices, making matrix inversion methods problematic. When linear gradient encoding fields are used, data from each coil can be FFT'd and combined in some way [96], [89]. But these Fourier imaging methods unsuitable in our case because of the use of nonlinear encoding fields.

Although it may be possible to represent  $\mathbf{E}$  as a sparse array in memory, permitting the use of direct inversion methods, iterative methods can be used instead to solve the least squares problem  $\|\mathbf{E}\mathbf{m} - \mathbf{s}\|$  on the full encoding matrix. We have chosen a time-domain based iterative reconstruction, which is accomplished by the successive evaluation of the forward model expressed as  $\mathbf{E}$ , instead of determining  $\mathbf{F}$ . The

Conjugate Gradient method [106] is popular, but the Algebraic Reconstruction Technique [107] is also often used. The generality of this approach allows arbitrary field shapes and coil profiles as well as systematic errors such as temperature-dependent field drifts to be incorporated into the encoding matrix.

### 5.3.1 Conjugate Gradients

The linear Conjugate Gradients method was initially proposed by Hestenes and Stiefel in 1952 for solving linear systems. The coefficient matrix must be positive definite, and the performance is determined by the condition number of the matrix. Pre-conditioning matrices can be used to improve the matrix condition number, and allow for faster convergence.

The iterative linear conjugate gradient algorithm is commonly used as an alternative MRI reconstruction method when 2DFT cannot be directly applied. For example, in undersampled parallel imaging [108], non-linear gradient MRI [78], imaging in the presence of field inhomogeneities [109], or non-cartesian k-space acquisitions [110].

The iterative method is used to solve a linear system of equations,  $Ax = b$ , by minimizing the quadratic function,  $\frac{1}{2}x^T Ax - b^T x$  [111]. A vector of zeros is often assumed for the initial guess of the solution,  $x_0$ , and then a new solution is searched for in each iteration,  $x_b$ . An advantage of the conjugate gradient algorithm is that it steps only once along each conjugate direction in the hyperspace defined by the quadratic objective function. There are built in MATLAB functions for the conjugate gradient method, but the user must decide how many iterations to calculate based on a convergence criterion, such as the relative change in mean image intensity between iterations.

Although, conjugate gradients is not currently the preferred reconstruction method for our scanner, it may prove to be advantageous in parallel computing of a solution and the possible addition of total generalized variation penalty for reducing artifacts and noise [112]. Initial CG reconstruction code has been used to reconstruct a biological experimental image (Figure 5-3). It is not feasible to store the entire encoding matrix and perform necessary matrix vector operations. Instead, ancillary functions

were used to generate the necessary products by calculating and storing one line of the  $\mathbf{E}$  matrix or  $\mathbf{E}^T$  matrix at a time. We found that simple matrix pre-conditioning with the diagonal of the  $\mathbf{E}$  matrix greatly accelerated the convergence of the solution (see Figure 5-3).

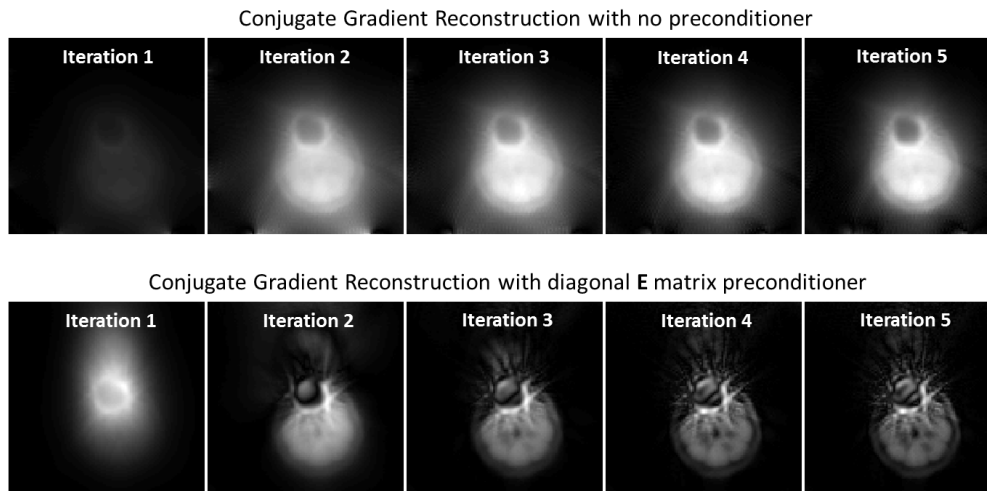


Figure 5-3: Conjugate Gradient reconstruction of experimentally acquired data of a lemon slice (described in section 5.4.2). The first row was reconstructed with no matrix preconditioner, and the second row was reconstructed with a simple preconditioner, the diagonal entries of the encoding matrix,  $\mathbf{E}$ .

### 5.3.2 Algebraic Reconstruction Technique - Kaczmarz method

The Kaczmarz method for iteratively solving linear system of equations was introduced in 1937 [113]. The method was applied in 1970 for the use of image reconstruction from CT projections, and is known as the "Algebraic Reconstruction Technique" (ART) [107]. Similar to the conjugate gradient method, this iterative technique can also be used to solve for the minimum norm least squares estimator of the image,  $\mathbf{m}$ . ART has been used for MR image reconstruction in O-space imaging [114], [95], [42].

The method is summarized by equation 5.8.

$$\hat{\mathbf{m}}_{new} = \hat{\mathbf{m}}_{old} + \lambda \frac{S_n - \langle \mathbf{E}_n, \hat{\mathbf{m}}_{old} \rangle}{\|\mathbf{E}_n\|^2} \mathbf{E}_n^* \quad (5.8)$$

The estimated image,  $\hat{\mathbf{m}}_{old}$ , is multiplied by the  $n^{th}$  row of the encoding matrix,  $\mathbf{E}_n$ , and subtracted from the  $n^{th}$  acquired signal,  $\mathbf{S}_n$ , to form an error. The index,  $n$ , can be incremented through the rows of the encoding matrix in any order, but for simplicity we simply step through the rows from first to last. The error is scaled and multiplied by the complex transpose of  $\mathbf{E}_n$  to update the image. This is done for each row of the encoding matrix, and then iterated through multiple times to eventually converge to the minimum norm least squares estimator. MATLAB code for calculating the  $n^{th}$  row of the encoding matrix is shown below.

```
E_n = C(:,q,r).*exp(-1i*2*pi*gamma*(field_map(:,r)+B_offset(r))
    *time(t));
```

The Algebraic Reconstruction Technique (ART) is currently our preferred method because intermediate reconstructed images can be monitored during the reconstruction on a line-by-line basis as the algorithm steps through the encoding matrix. This is useful because errors with the encoding matrix calibration or data structure may be seen immediately. Example of these intermediate images are shown in section 5.4.1. In contrast, CG requires full matrix-vector products before each image iteration may be viewed. There are some methods for parallel processing of ART [115], but the use of parallel computing to accelerate the CG method is more straightforward which may lead to the long-term use of the Conjugate Gradient method.

We currently use 5 iterations of ART for  $\lambda = 0.2$ . These numbers have been determined by visual examination of the reconstructed image quality. Examination of the reconstruction convergence based on L-curve plots of image bias versus noise may be useful in future work.

## 5.4 Results: 2D Images

The reconstructed images and simulations shown here were done using the Algebraic Reconstruction Technique. To demonstrate the importance of temperature drift compensation, a phantom image was also reconstructed with an uncorrected encoding matrix. The field of view of the images is 16 cm and the in-plane voxel size is 0.625

mm. All of the spin-echos were acquired with a 40 kHz readout bandwidth with 256 points (read-out time = 6.4 ms). The other pulse sequence parameters vary (number of magnet rotations, the length of the spin-echo train, number of averages).

### 5.4.1 Single Coil Image

Figure 5-4 shows initial images of a “MGH” phantom filled with  $\text{CuSO}_4$  doped water. The 3D printed polycarbonate phantom is 1.7 cm thick with a 13 cm diameter. The data were not acquired from the currently used receive array. Instead, the solenoid transmit coil was used as a transmit/receive coil with the addition of a passive transmit/receive switch.

91 projections ( $N_{\text{rots}} = 91$ ) were acquired as spin-echo trains from magnet rotations spaced  $2^\circ$  apart. 32 averages of a spin-echo train with 6 echos were acquired at each rotation. The repetition time (TR) between average was 550 ms, and the temporal spacing between the spin-echos (echo-spacing) was 8 ms. The total acquisition time for this image was 12 min. 30 sec. For a selection of 5 out of the 91 rotations, Figure 5-4a shows the orientation of the SEM and the relative position of the phantom. Figure 5-4b shows the projection of the phantom onto the nonlinear field at each rotation. Figure 5-4c shows intermediate ART reconstructed images ( $\hat{\mathbf{m}}_{\text{new}}$ ) after going through the corresponding rotation in the encoding matrix. The final image is also shown after 4 iterations of the entire encoding matrix in the reconstruction. The top half of the image should ideally be empty. Instead, the expected aliasing pattern is seen through the center onto the frequency matched quadrants of the FOV because the data was acquired with a single uniform coil instead of the multi-coil array. The alias is blurred because the Halbach magnet’s SEM is only approximately quadrupolar, with some first-order and higher-order field components.

### 5.4.2 Multi-coil Images

Images of a “MIT/MGH” phantom were acquired with 7 coils ( $N_c = 7$ ) of the Rx array Figure 5-5(b-c). This phantom is also a 3D printed polycarbonate 1.7 cm thick with a

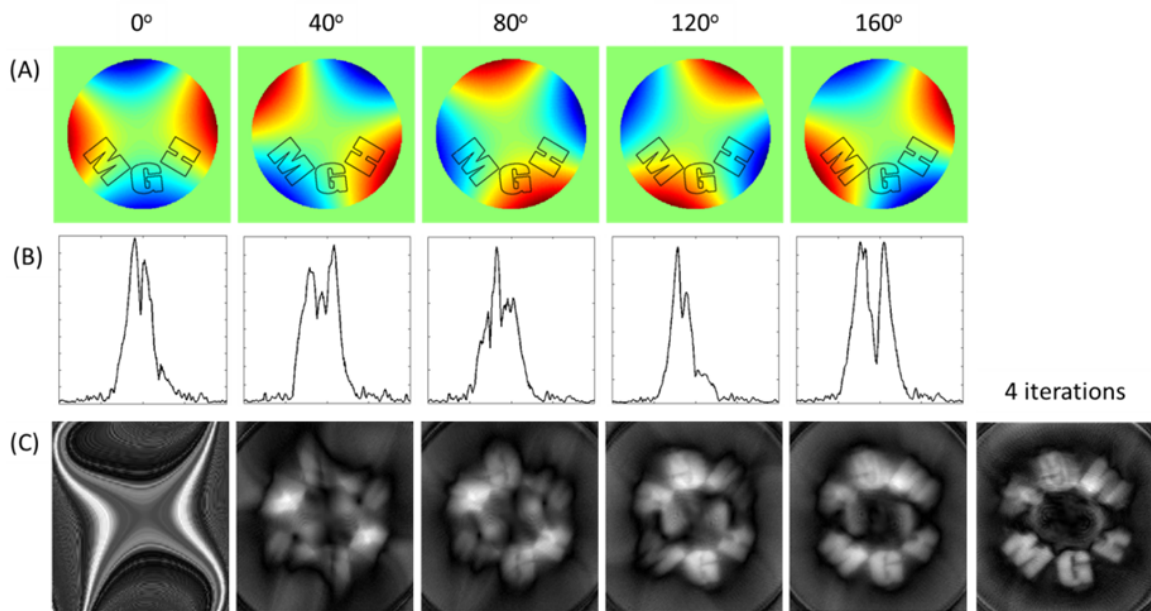


Figure 5-4: Experimental 2D image of an “MGH” water-filled phantom, acquired with the transmit solenoid in Tx/Rx mode. (A) The position of the phantom in the field map is shown for each rotation. (B) The projection of the phantom onto the encoding field is shown for each rotation. (C) The intermediate reconstructed images from the rotations so far are shown. The reconstructed image is then shown after 4 iterations through the entire encoding matrix. Projections are acquired at 91 rotation angles ( $N_{\text{rots}} = 91$ ).

13 cm diameter disk filled with  $\text{CuSO}_4$ -doped water. 91 projections ( $N_{\text{rots}} = 91$ ) were acquired as spin-echo trains from magnet rotations spaced  $2^\circ$  apart. Eight averages of a spin-echo train with 16 echos were acquired at each rotation with  $\text{TR} = 550$  ms and echo-spacing = 8 ms. The coil array's lengthy acquisition time of 66 minutes results from acquiring with a single console receiver and would be reduced to 7.3 minutes by acquiring data from all of the coils in parallel. The importance of monitoring and correcting for field drift due to temperature is emphasized by comparing Figure 5-5b and Figure 5-5c which show images with and without temperature drift correction (from the field-tracking probe).

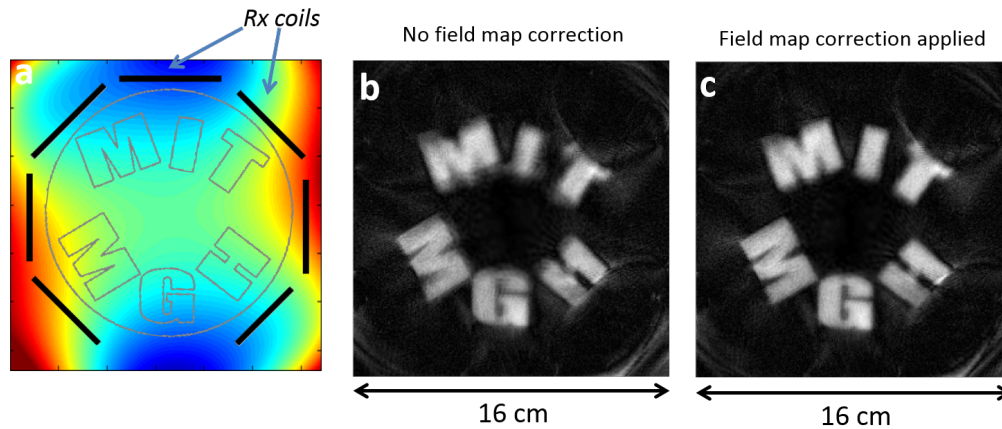


Figure 5-5: Experimental  $256 \times 256$  voxel, 16 cm FOV images of a 3D printed phantom with  $\text{CuSO}_4$  doped water occupying the interior of the letters. The phantom has a 13 cm diameter and is 1.7 cm thick. 91 magnet rotations spaced  $2^\circ$  apart were used ( $N_{\text{rots}} = 91$ ), readout bandwidth/ $N_{\text{readout}} = 40$  KHz/256,  $\text{TR} = 550$  ms, 8 ms echo-spacing. Echoes in the spin-echo train for a given rotation were averaged. (a) The water filled cavities of the phantom are shown in relation to the encoding field,  $B_{SEM}$ , for the first rotation angle. The positions of the Rx coils are also shown. (b) Image acquired with 7 coils ( $N_c = 7$ ) of the Rx coil array (8 averages of a 16 spin-echo train). Temperature drift was not corrected for. (c) Image from same data as (b), but with temperature drift correction implemented.

A 1 cm thick lemon slice was imaged using only the bottom 5 surface coils ( $N_c = 5$ ) with 181 magnet rotations ( $N_{\text{rots}} = 181$ ) spaced  $1^\circ$  apart. (Figure 5-6). The total acquisition time was 93 minutes (15.5 minutes if surface coils and field-tracking probe were acquired in parallel). A single average of a 128 echo train at each rotation provided sufficient SNR ( $\text{TR} = 4500$  ms, echo spacing = 8 ms). The use of 5 coils

of the receive array minimizes aliasing in the image. For comparison, the image was reconstructed using data from 91 out of the 181 rotations as well as the full data set. Using the reduced data set results in poorer image quality and streaking artifacts.

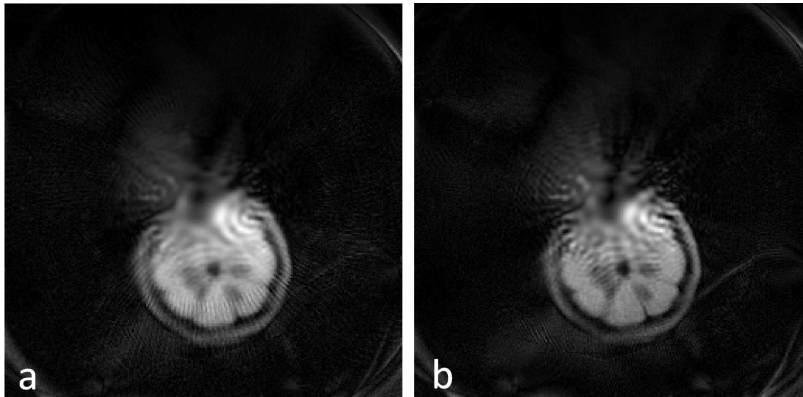


Figure 5-6: Experimental  $256 \times 256$  voxel, 16 cm FOV image of a 1 cm thick slice of lemon placed off axis in the magnet. 5 receiver coils of the array ( $N_c = 5$ ) were used to acquire 1 average of a 128 spin-echo train, readout bandwidth/ $N_{pts} = 20$  KHz/256, TR = 4500 ms, echo-spacing = 8 ms. A) 91 magnet rotations ( $N_{rots} = 91$ ) spaced  $2^\circ$  apart were used (B) 181 magnet rotations ( $N_{rots} = 181$ ) spaced  $1^\circ$  apart were used.

### 5.4.3 Discussion

As expected, the non-bijective mapping of the Halbach magnet’s SEM results in aliasing through the center (Figure 5-4). Fortunately, as described in [41] the aliasing is resolved by the addition of a multi-channel receive array with differing spatial profiles and an appropriate geometry. Since the Halbach magnet’s encoding is dominated by the quadrupolar “PatLoc” SEM, the system’s spatially-varying voxel size changes approximately as  $c/\rho$  within the FOV, where  $\rho$  is the radius and the constant  $c$  depends on the strength of the SEM and the length of the readout [92]. This means that our Halbach magnet encoding field results in higher resolution at the periphery due to the uniform nature of the SEM near the center of the FOV. This center blurring is seen in both the experimental images in Figure 5-6, and will be discussed in more detail in Chapter 6.

The lemon images of Figure 5-6 show that when 91 projection rotations are used instead of 181, a radial streaking artifact is visible. The streaking artifacts are con-

sistent with those arising in conventional undersampled radial trajectories played by linear SEMs [110] as well as undersampled radial trajectories played by PatLoc SEMs [93], [112]. It has been shown that the use of total variation and total generalized variation priors during reconstruction suppresses streaking artifacts in undersampled conventional radial [110] and PatLoc radial [112] acquisitions. Similar techniques may be pursued in future work to suppress streaking in images obtained with fewer projection rotations of our scanner.

In addition to the center “encoding hole”, which is expected from the SEM shape (see Chapter 6), there are other artifacts from systematic errors. These errors are most likely a result of field map and coil sensitivity profile inaccuracies, which are critical to the iterative reconstruction [42]. The current coil sensitivity profiles facilitate proof-of-concept reconstructions, but their fidelity is suspect because they were calculated rather than measured. In these calculations the magnetostatic Biot Savart approximation was used with no external structures present. While wavelength effects in the body are not expected at this frequency, the close proximity of the conducting magnets and other coils might perturb the experimental fields. Additionally, a 2D field map is currently used to reconstruct thin samples (1 to 1.5 cm thick), but field variation does exist in the  $x$  direction (along the axis of the Halbach cylinder) within the sample thickness (see Figure 3-11 in Section 3.5). This may cause through-plane dephasing and should be incorporated into the encoding matrix based on a 3D field map.

Field map errors arise from temperature drifts which are significant on the time scale of the imaging and mapping acquisitions. We have shown that any uncorrected temperature drift causes substantial blurring in the image (Figure 5-5b). Temperature drift is a pervasive problem in permanent magnet MRI and has been addressed in a number of ways. In the current experimental protocol the frequency at a fixed point is measured at every rotation and the drift is built into the encoding matrix as a global offset to the field maps. This method reduces blurring considerably (Figure 5-5c), but the assumption that magnet heats isotropically is suspect. Other hardware options have been proposed for permanent magnet NMR and MRI that may offer higher

encoding matrix accuracy, such as the addition of insulation and RF frequency-lock method [31] or a more temperature stable magnet designs [116].

Currently, the forward model assumes perfect  $90^\circ$  and  $180^\circ$  flip angles throughout the FOV from the excitation pulses; this is another potential source of reconstruction error. The SEM is always on during the excitation pulses, so there is a wide Larmor frequency range in the sample (about 35 KHz for a large 2D sample) which should ideally be covered uniformly by the excitation magnetic field. However, the excitation pulses have a finite bandwidth that is approximately sinc-shaped in frequency due to the frequency content of the console generated signal as well as the quality factor (Q) of the transmit coil. Therefore, “off-resonant” spins in the sample experience different flip angles and phase variation. “Crusher gradients” are generally used in conventional spin-echo pulse sequences to spoil unwanted transverse magnetization from imperfect flip angles. In our case, the gradient field is not switchable so we cannot use crusher gradients. The imperfect spin behavior could be estimated in a flip angle simulations based on field maps and the frequency content of the excitation magnetic field. This estimated behavior may be incorporated into the forward model in future work for increased accuracy in the image reconstruction.



# Chapter 6

## Spatial Resolution in rSEM

When non-linear spatial encoding magnetic fields (SEMs) are used for MR image encoding, the resulting spatial resolution is spatially non-uniform. This is the case in the intrinsic encoding field present in constructed Halbach magnet, as well as in the gradient coil produced SEMs in PatLoc [41], Ospace [95], and 4D-RIO imaging [94]. The proposed portable brain scanner uses permanent magnet to produce the SEM, therefore the gradient field is always on, and encoding is performed by rotating the SEM around the object. This rotating spatial encoding magnetic field form of MRI (rSEM) can be done with arbitrary encoding field shapes. We examine the spatial variations in image resolution from different SEMs for rotating scanners through simulation.

### 6.1 Simulation Method

2D data sets were simulated for the multiple rotating SEMs shown in Figure 6-1 including:

- (a) The measured center slice field map from the previously described Halbach magnet.
- (b) The measured center slice field map from the Halbach magnet + an artificial linear gradient field of 1.2 mT/m

- (c) The measured center slice field map from the Halbach magnet + an artificial linear gradient field of 2.4 mT/m
- (d) A pure linear gradient magnetic field of 6 mT/m (comparable range as the Halbach SEM)

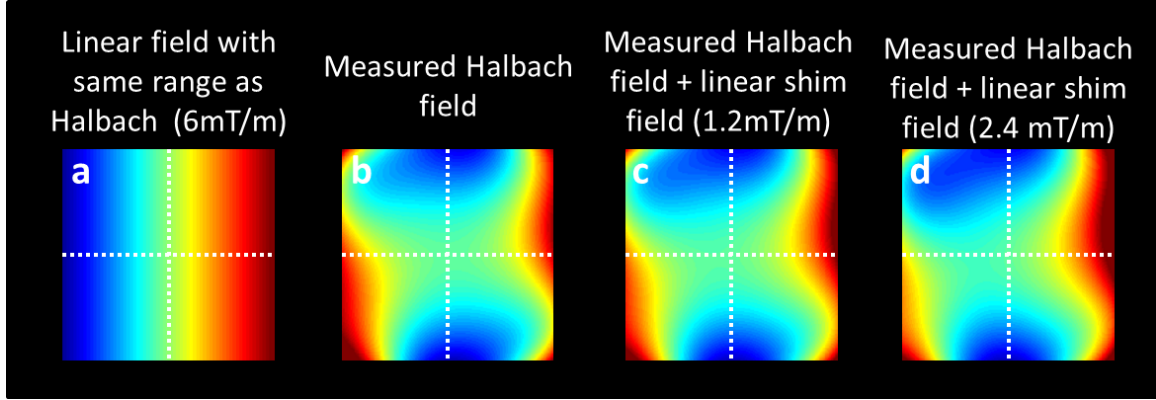


Figure 6-1: Rotating Spatial Encoding Magnetic Fields (rSEMs) used in simulations. (a) The measured center slice field map from the previously described Halbach magnet. (b) The measured center slice field map from the Halbach magnet + an artificial linear gradient field of 1.2 mT/m. (c) The measured center slice field map from the Halbach magnet + an artificial linear gradient field of 2.4 mT/m. (d) A pure linear gradient magnetic field of 6 mT/m (comparable range as the Halbach SEM)

In order to evaluate spatial resolution, data was simulated from a line of point sources (0.25 mm width) spaced 5 mm apart along the radius of the 16 cm circular FOV (Figure 6-2a). Images were also simulated using a high resolution T1 weighted brain image as a simulation object, which was scaled to the 16 cm FOV of the SEMs (Figure 6-2b).

The simulation method involves the formation of an encoding matrix based on the simulation parameters and the chosen SEM. The encoding matrix is calculated the same way it is for reconstructing images (section 5.2), except it is unnecessary to include  $B_{offset}$ . The data,  $\mathbf{S}_{sim}$ , is simulated as the product of simulation object (represented as a vector:  $\mathbf{m}_{sim}$ ) and the encoding matrix,  $\mathbf{E}$ .

$$\mathbf{S}_{sim} = \mathbf{E}\mathbf{m}_{sim}, \quad (6.1)$$

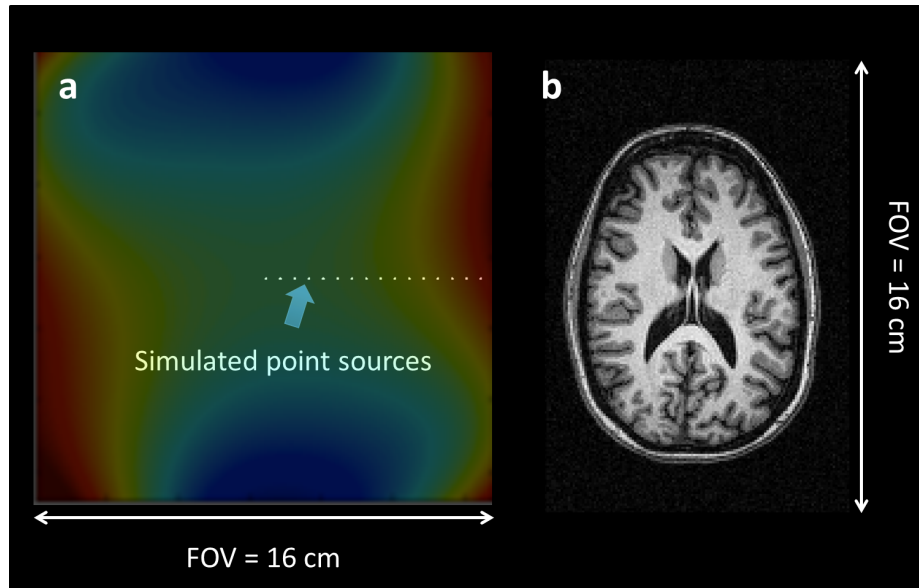


Figure 6-2: Simulation objects. (a) Line of 0.25 mm wide point sources spaced 5 mm apart along the 8 cm radius of the FOV. (b) Reference high resolution 3T T1 weighted brain image used as simulation object. The brain simulation object was scaled to the 16 cm FOV of the SEMs.

The encoding matrix was formed assuming a 40 KHz sampling bandwidth and 256 readout points. Spin-echoes were simulated for each coil and each magnet rotation (181 angles spaced  $1^\circ$  apart). The phase accumulation with time in each voxel is calculated using the magnetic field map, then multiplied by the complex coil sensitivity map and the magnitude of the simulated object, and summed to form the net signal. MATLAB code for calculating each data point  $S(n)$  is shown below. The calculation requires the line-by-line calculation of the encoding matrix,  $E_n$ , instead of the storing the full matrix. This code snippet is nested in for-loops to compute data for all of the coils and rotation angles.

```
E_n = C(:,cc,rr).*exp(-1i*2*pi*gamma*field_map(:,rr)*time(tt));
S(n) = sum(E_n .* m_sim) + noise_level*(rand+1i*rand);
```

Simulated images are reconstructed with the same reconstruction method used for experimental data (Chapter 5). The general encoding model forms a set of linear equations that are solved iteratively using the Algebraic Reconstruction Technique.

## 6.2 Simulation Results

The 2D images of a line of point sources simulated from 4 rotating SEMs are shown in Figure 6-3. 1D images of a line through the center of the point sources (along the radius), is shown in Figure 6-4. These images represent the radially variable point spread function for the given simulation parameters. These results simulate the use of the solenoid coil in transmit/receive mode, so a single uniform coil sensitivity was assumed.

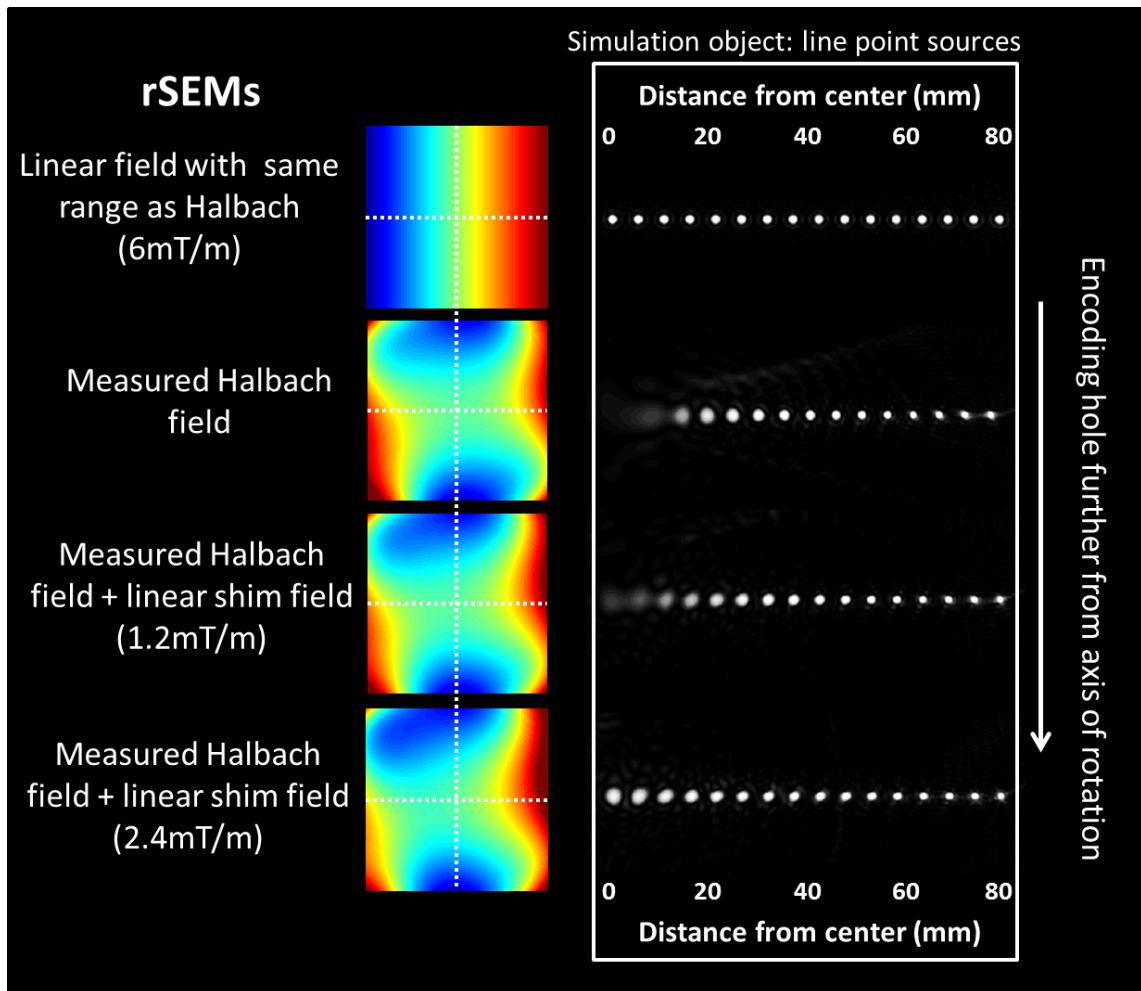


Figure 6-3: Simulated 2D image of a line of points starting at center of FOV (spaced 5 mm apart) using multiple rotating SEMs.

As expected, the resolution of the images produced by the pure linear encoding field is uniform. This is because the magnetic field gradient is the same everywhere in

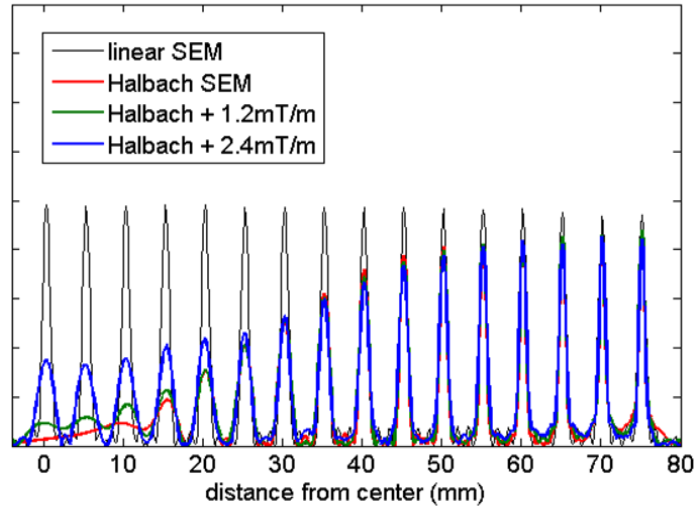


Figure 6-4: Simulated 1D image of a line of points starting at center of FOV (spaced 5 mm apart) using multiple rotating SEMs.

the FOV, and resolution is inversely proportional to the gradient strength [117]. In the simulation done with the measured Halbach SEM, the point-spread-functions are no longer uniform along the radius because the gradient is not uniform. The non-linearity of the encoding field is especially dramatic in the center where the spatial derivative of the SEM gradient is close to zero resulting in no spatial encoding. However, when a linear field component is added to the Halbach SEM, some of the resolution is recovered.

The simulations shown in Figure 6-3 and 6-4 were done assuming a single uniform receive coil instead of the 8 channel receive array. This is was simply done for the sake of simulation time. The simulation of the line of point sources for the Halbach SEM was repeated using the coil sensitivities of the 8 channel array. The resulting 1D image is shown in Figure 6-5, with the previously shown “solenoid” generated simulation for comparison. The resolution does not seem to be significantly effected by the use of the coil array. However, the signal level increases dramatically at points further from the center because they are closer to the surface coils (which are more sensitive to nearby signals).

Figure 6-6 shows the variation in full-width at half-max (FWHM) of the simulated point spread functions along the radius (same simulation as Figs. 6-4 and 6-3). These

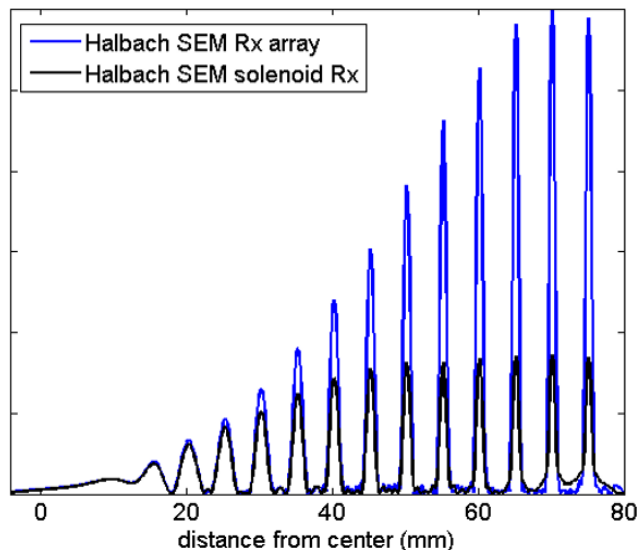


Figure 6-5: Simulated 1D image of a line of points starting at center of FOV (spaced 5 mm apart) using the measure Halbach SEM for rSEM encoding, and the coil sensitivities of the solenoid (assumed to be uniform) and 8 channel receive array.

FWHM point-spread-function simulations can be used to determine an appropriate SEM to achieve a desired resolution in the center of the FOV. For example, for a target resolution of 3 mm in the center, Figure 6-6 suggests a linear shim  $> 2$  mT/m must be added to the Halbach SEM.

Figure 6-7 shows the simulated brain images using the calculated 8 channel receive array sensitivity maps. The same previously described SEMs were used for the simulations. The noise levels added to the simulated time domain data were set greater than the observed noise in experimentally acquired spin-echos of a water phantom.

### 6.3 Discussion

In all of the simulations, the resolution resulting from the rotating linear SEM is nearly uniform. In contrast, multi-polar SEMs (like the Halbach SEM) have a steep gradient near the periphery and a shallow gradient near the center. Therefore the spatially-varying voxel size changes approximately as  $c/\rho$  within the FOV, where  $\rho$  is the radius and the constant  $c$  depends on the strength of the SEM and the length of

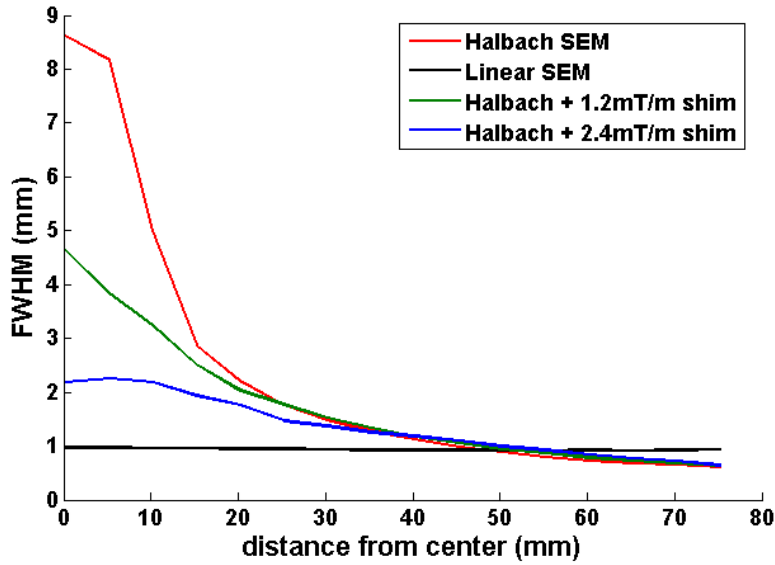


Figure 6-6: Point sources (0.25 mm width) were used to evaluate FWHM of point spread function along radius of the FOV. From these FWHM calculations, it can be concluded that for target resolution of 3 mm in center, a linear shim of  $> 2$  mT/m is necessary.

the readout. This translates to higher resolution near the periphery and an “encoding hole” in the center. This center blurring is seen in all of the simulated images above, and also in the experimental images in Chapter 5.

Other encoding methods which employ the use of multi-polar encoding fields have also encountered the encoding hole problem, and have combined multi-polar (typically quadrupolar) and linear SEMs to move the encoding hole and to take advantage of position dependent resolution [94], [95]. This is an idea that we have exploited as well in simulation.

Intuitively, if a sufficient linear term is added to the rotating quadrupolar SEM, the encoding hole will no longer coincide with the axis of rotation. Instead, the hole will move around the object as the magnet is rotated during acquisition. This will allow some rotations to contribute to encoding of any given pixel. This is shown in the simulations that were performed with the “Halbach+Linear SEM”, which show improved resolution near the center.

The spatially varying resolution of an image acquired with nonlinear SEMs can be evaluated with the idea of “local k-space”, which is defined in equation 6.2 [94], [118], [40].

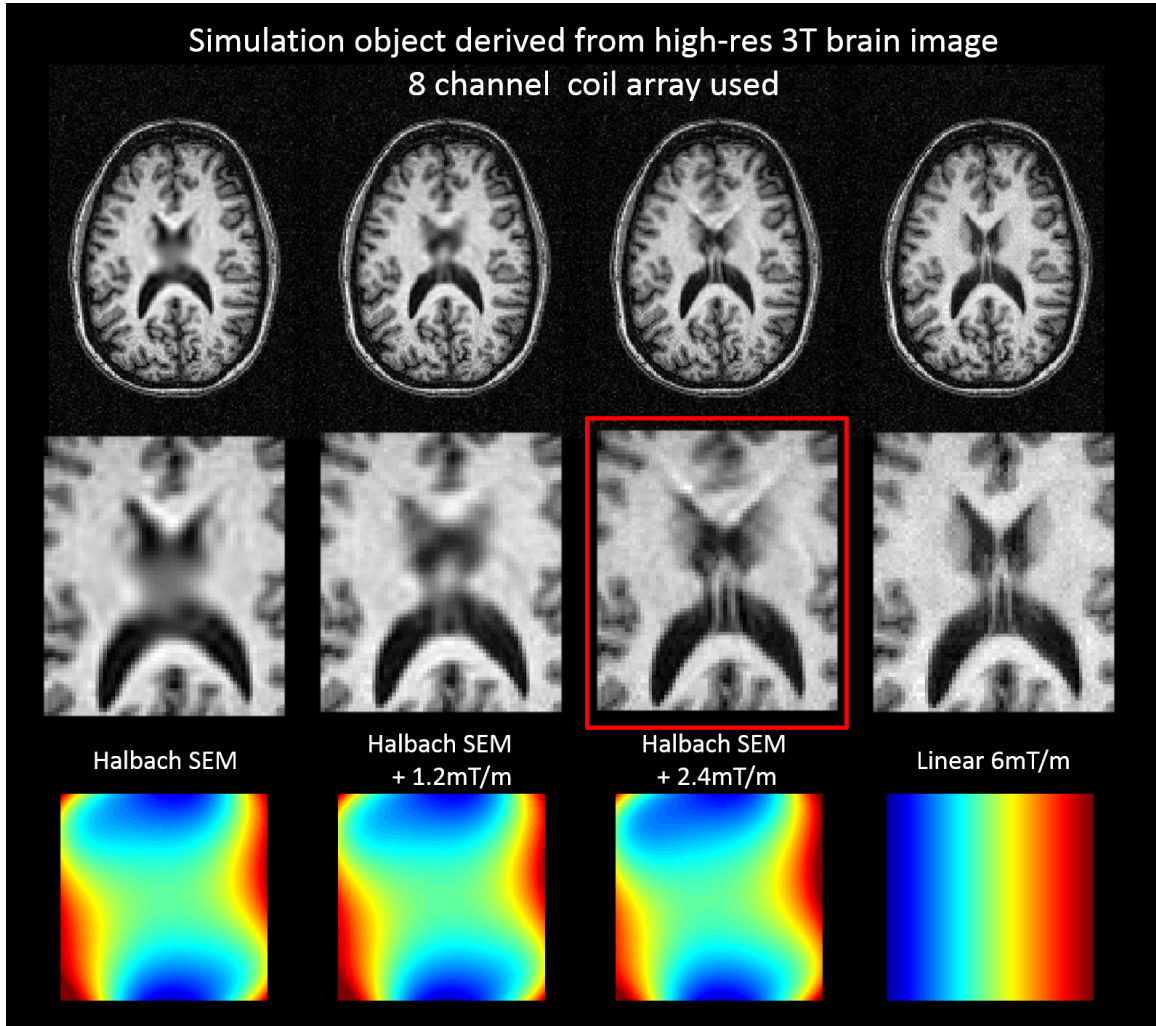


Figure 6-7: A high resolution T1 weighted brain image was used as the simulation object, and four field maps were used for the rotating SEMs (bottom row). The top row shows the full simulated brain images, and the second row shows a zoomed-in version of the center to emphasize the resolution in the shallow gradient region. Spin-echo signals modulated by the SEM and coil sensitivities are simulated for the standard readout time (6.4 ms) for the 8 surface coils at each rotation index,  $r$ . Data is simulated for 181 magnet rotation angles spaced  $1^\circ$  apart.

$$k_{loc}(\mathbf{x}, t) = \nabla\phi(\mathbf{x}, t) \quad (6.2)$$

Local k-space is simply the spatial derivative of accumulated phase, which is spatially dependent when non-linear SEMs are used. If traditional linear SEMs are used  $k_{loc}$  is independent of  $\mathbf{x}$ . Gallichan et al. evaluated the spatially varying resolution of different linear + non-linear SEM trajectories using local k-space analysis in [118]. Layton et al. used local k-space to design trajectories that improve local resolution in selected regions of interest (ROI) at the expense of blurring elsewhere in the FOV in Ref. [40].

A similar analysis can be done with the rotating SEMs evaluated here, to predict the spatially varying resolution. In figure 6-8, the average SEM gradient ( $G_{ave}(\mathbf{x})$ ) seen by the object for the image sequence described above (181 rotation angles spaced  $1^\circ$  apart) is shown for the four evaluated rSEMs.

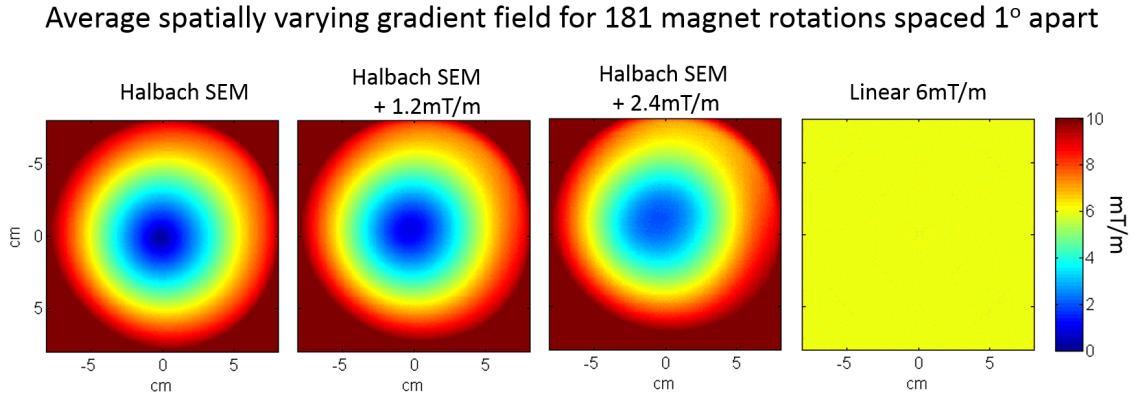


Figure 6-8: The average gradient field seen throughout the 2D FOV is shown for 181 magnet rotations spaced  $1^\circ$  apart. The gradient magnitude was calculated in each pixel for each rotated field map. The gradient fields for all of the rotations were then averaged together.

In Fourier imaging, the theoretical resolution limit is  $\frac{1}{k_{max}}$ . For non-linear SEM, this is analogous to equation 6.3, where  $T$  is half of the total spin-echo readout time.

$$\Delta\mathbf{x} = \frac{1}{\frac{\gamma}{2\pi}G_{ave}(\mathbf{x})T} \quad (6.3)$$

The spatially varying voxel size estimate is shown in Figure 6-9. The values were calculated using the average gradient field map in Figure 6-8. For the 40 kHz BW, 256 point spin-echo readouts that are generally used, the maximum phase accumulation occurs over half the readout time, so  $T = 6.4 \text{ ms}/2 = 3.2 \text{ ms}$ . These calculated values, do not agree exactly with the simulated FWHM values in Figure 6-6, but follow the same trend.

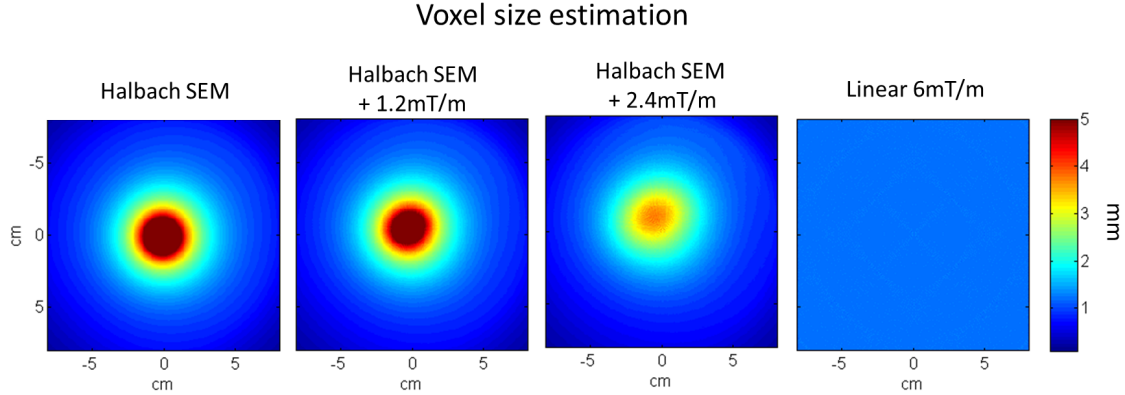


Figure 6-9: The spatially varying voxel size was estimated using the average gradient fields shown in Figure 6-8. The voxel size was calculated according to equation 6.3, assuming  $T = 3.2 \text{ ms}$ .

For all of the simulations shown, the same voxel grid is used for the encode step and the reconstruction step. This potentially limits the accuracy of the results, since the effect of intravoxel spin dynamics are not fully captured. However, the present simulations are consistent with much of the published simulation literature involving non-linear gradients and as such still provide a great deal of insight into the imaging performance that can be achieved using the Halbach magnet rSEM method.

## 6.4 Conclusion

While we did not attempt to control the precise spherical harmonic distribution in the magnet design, future work will likely benefit from shimming the magnet to obtain a more desirable SEM. For example, if a sufficient linear term were added, the uniform encoding field region would not lie on-axis with the rotation, and the

“encoding hole” will move around the FOV causing less severe blurring. Pursuing this strategy even further would result in a SEM containing only a linear term. In this case, the encoding becomes very similar to a radial imaging scheme with conventional gradients, and to the strategy proposed by Cho et al. who used a rotating gradient coil in a conventional magnet [39]. With accurate field mapping instrumentation and shimming software, we suspect that the magnet could be shimmed to a SEM that is dominated by 1st order (linear) terms, but completely eliminating higher order terms is unlikely. The generalized reconstruction method would permit the use of approximately linear SEMs that have significant higher-order impurities which would cause artifacts in Fourier reconstruction.

Although a linear SEM would eliminate the encoding hole and image aliasing, higher order SEMs lead to a gain in resolution at the periphery compared to linear SEMs with equivalent field ranges. This gain in resolution at the periphery comes at the expense of decreased resolution in the center, but might be advantageous in some applications. For example, higher resolution near the skull would be useful for the detection of subdural and epidural hematoma from traumatic brain injury. While an approximately linear SEM is the most versatile, the ideal SEM may depend on the imaging application.



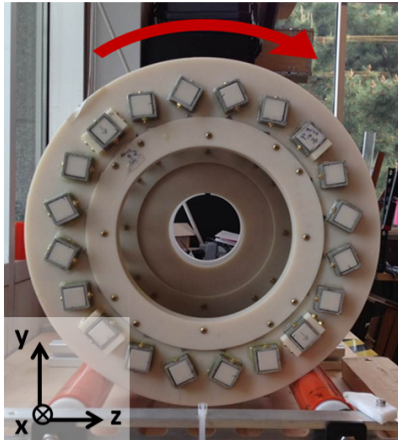
# Chapter 7

## Potential 3rd Dimension Encoding

### Methods

We have demonstrated proof-of-concept images for the 2D encoding method with thin samples. However, the addition of 3rd axis encoding is an obvious requirement for medical applications.

2D encoding– projection imaging



3<sup>rd</sup> axis encoding –  $B_1$  encoding

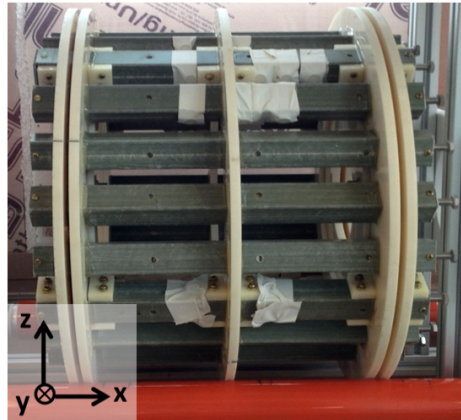


Figure 7-1: 2D image encoding in the  $y - z$  plane is done by rotating the magnet around the sample to do generalized projection imaging. In order to image 3D objects, we need to encode in the  $x$  direction as well. We propose using a  $B_1$  encoding method instead of the addition of a gradient coil.

2D image encoding in the y-z plane is accomplished as a general form of projection imaging by physically rotating the cylindrical magnet. The unique aspect of this encoding method is that it is accomplished without electromagnetic gradient coils. This has major advantages for keeping cost, weight, complexity, and power requirements low for the portable scanner. Likewise, it would be preferred to encode in the 3rd dimension (along the cylindrical axis) without adding a gradient coil and gradient power amplifier. Instead, a  $B_1$  encoding method could be used, in which the RF excitation coil creates spatial phase variation. This could be accomplished with little additional cost, weight, or power requirements because the excitation coil is already a requirement for data acquisition. There are two  $B_1$  encoding methods which we are currently exploring, the Bloch-Siegert Spatial Encoding Technique (BS-SET) and TRansmit Array Spatial Encoding (TRASE). These two methods both theoretically work well with our pulse sequences (spin-echo trains), but have not been experimentally validated in the portable scanner yet.

## 7.1 Bloch Siegert Spatial Encoding Technique - BS-SET

### 7.1.1 Theory

The Bloch Siegert Spatial Encoding Technique was proposed by Kartausch and Helluy in 2013 [19] as a way of exploiting the Bloch-Siegert shift phenomenon for image encoding. The Bloch-Siegert shift is a change in the resonant frequency of the spin caused by far off-resonance RF excitation [119], [120].

The difference between the precession frequency of the spins,  $\omega_0$ , and the frequency of the off-resonance “Bloch-Siegert pulse” (BS pulse),  $\omega_{RF}$ , is  $\Delta\omega_{RF} = \omega_0 - \omega_{RF}$ . The nutation frequency of the coil,  $\omega_{B1} = \gamma B_1$ , is the frequency at which the excitation pulse rotates the spin magnetization. If we assume that the off-resonance of the Bloch-Siegert pulse is large compared to the nutation frequency of the coil:

$$\Delta\omega_{RF} \gg \omega_{B1}, \quad (7.1)$$

then it can be shown that Bloch-Siegert shift in precession frequency is:

$$\Delta\omega_{BS} = \frac{(\gamma B_1)^2}{2\Delta\omega_{RF}}, \quad (7.2)$$

and the resulting phase shift is:

$$\Delta\phi_{BS} = \int_0^\tau \Delta\omega_{BS}(t)dt = \int_0^\tau \frac{(\gamma B_1(t))^2}{2\Delta\omega_{RF}} dt. \quad (7.3)$$

This idea was used for  $B_1$  mapping by Salolick et al. in 2010 [121] by inserting an additional off-resonance RF pulse into an imaging sequence (making sure that the extra pulse does not excite the sample). Then, the resulting spatial phase shift was used to determine the spatial variation in the  $B_1$  magnitude. If a square BS pulse of length  $\tau$  is used, then the phase relationship is:

$$\Delta\phi_{BS}(x) = \frac{(\gamma B_1(x))^2 \tau}{2\Delta\omega_{RF}}. \quad (7.4)$$

Similarly, Kartausch et al. proposed an intentionally varying  $B_1$  magnitude to induce a spatially dependent phase shift for image encoding [19]. They demonstrated an experiment using a dedicated “BS coil” with a spatially dependent  $B_1$  shape to apply an off-resonance RF pulse, and used a separate on-resonance RF coil for excitation.

When a far off-resonance BS pulse is played after excitation, the flip angle of the spins should not be effected. Instead, much like the application of a  $B_0$  gradient pulse, a spatially varying phase accumulation is imposed which depends on the length of the pulse. If a BS coil is used that imposes a linear  $B_1$  field along the encoding axis, the induced precession phase will be spatially quadratic according to equation 7.4. Instead, if the BS coil has  $B_1$  magnitude that varies with  $\sqrt{x}$  instead of  $x$  (shown in Figure 7-2a), the resulting spatial phase variation will be linear and the traditional k-space model can be used.

## 7.1.2 Pulse Sequence

An example spin-echo based pulse sequence is shown in Figure 7-2b. If we assume  $\Delta\phi_{BS}(x)$  to be linear in  $x$ , then a short BS pulse ( $\tau = \Delta t$ ) played after the  $180^\circ$  (green pulse in Figure 7-2) results in the k-space sample,  $k = \Delta k$  (green dot). The sequence is then repeated with a longer BS pulse after the  $180^\circ$  (blue pulse) with  $\tau = 2\Delta t$ . This results in the  $k = 2\Delta k$  sample (blue dot). This idea is repeated with pulses  $\tau = n\Delta t$ , until the desired number of positive k-space points ( $k_{max} = n\Delta k$ ) are acquired. Then, the whole process is repeated with the BS pulse played before the  $180^\circ$  excitation pulse. The  $180^\circ$  pulse causes the BS induced phase to be flipped, effectively filling negative k-space.

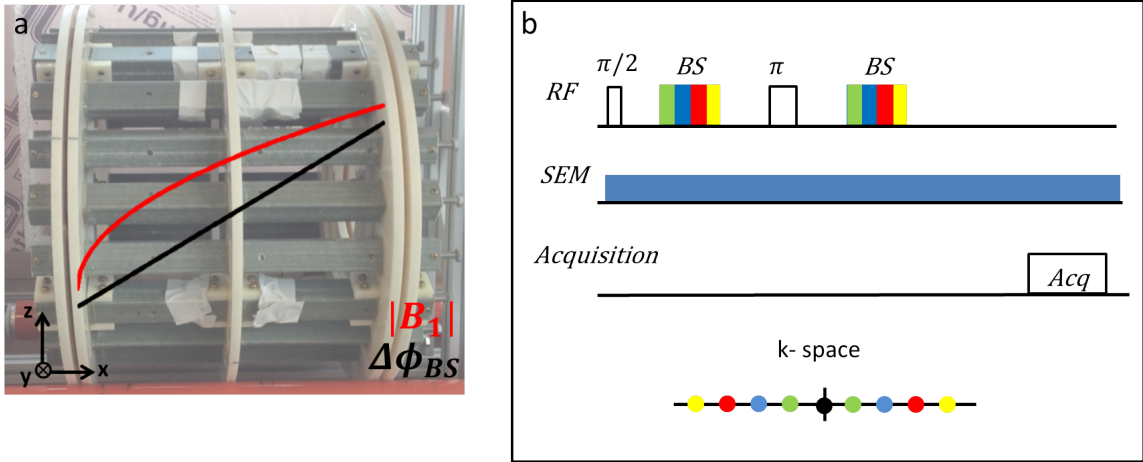


Figure 7-2: (a) The Bloch Siegrert Encoding Technique (BS-SET) is performed using a  $B_1$  excitation field with a spatially varying magnitude along the encoding direction. In our case, the encoding direction is along the axis of the Halbach cylinder ( $x$ ). If  $B_1$  varies with  $\sqrt{x}$  (as shown here), the resulting spatially varying phase of the precessing spins ( $\Delta\phi_{BS}(x)$ ) will be linear with  $x$ . When the spatially varying phase is linear, a true k-space model can be used, otherwise the acquired points could be visualized in a warped or analogous k-space domain. (b) The BS-SET pulse sequence is a modified spin-echo sequence which applies BS pulses of increasing length played either after or before the  $180^\circ$  excitation pulse to traverse the 1D k-space domain.

If we assume that the BS coil produces a  $B_1$  field that is proportional to  $\sqrt{x}$  ( $B_1(x) = \sqrt{G_1 x}$ ), then according to equation 7.4:  $\Delta\phi_{BS}(x) = \frac{\gamma^2 G_1 x \tau}{2\Delta\omega_{RF}}$ . The corresponding k-space point is  $k = \frac{\Delta\phi_{BS}(x)}{2\pi x}$ . When the BS pulses are incremented by  $\Delta t$ ,

the k-space increments are:

$$\Delta k = \frac{\gamma^2 G_1 \Delta t}{4\pi \Delta \omega_{RF}}, \quad (7.5)$$

and the field of view (FOV) is:

$$FOV = \frac{1}{\Delta k} = \frac{4\pi \Delta \omega_{RF}}{\gamma^2 G_1 \Delta t}. \quad (7.6)$$

Our desired FOV for human head imaging in the  $x$  direction is 20 cm. If we assume a BS off-resonance of 200 kHz ( $\omega_{RF} = 1.26 \times 10^6$  ( $\frac{\text{rad}}{\text{s}}$ )), and time increment of  $50\mu\text{s}$  ( $\Delta t = 50\mu\text{s}$ ), then we will need  $G_1 = 2.2 \times 10^{-5}$  ( $\frac{\text{T}^2}{\text{m}}$ ). Therefore, the required BS field is:  $B_1(x) = \sqrt{G_1 x} = 4.7\sqrt{x}$  mT. Because our  $B_0$  field is inhomogeneous, the actual  $\Delta \omega_{RF}$  varies slightly throughout the sample, resulting in variations in the calculated FOV and warping of the resulting “slices”. This warping is minimized by choosing  $\Delta \omega_{RF}$  to be large compared to the Larmor frequency variation in the sample. For the example values given above, a Larmor frequency variation of 50 kHz will result in FOV variation of 4%.

The k-space formalism is convenient because a simple 1D inverse Fourier transform can be used to reconstruct the data along the BS encoding axis. In practice, an arbitrary shape along  $x$  can be used for the  $B_1$  magnitude, and generalized reconstruction methods (like those described in Chapter 5) can be used to reconstruct along  $x$  (as long as the  $B_1$  shape is known).

### 7.1.3 Experiment

We used a similar experimental setup to Ref. [19] for an initial 1D encoding experiment of a small sample. A 1.2 cm diameter, 1 cm long solenoid tuned to 3.29 MHz was used as the on-resonance receiver and transmitter (Rx/Tx) coil. The imaging sample is contained in a 1 cm diameter NMR tube which fits tightly in the Rx/Tx coil. A separate 2 cm diameter, 1 cm long solenoid was used as the Bloch-Siegert (BS) coil. The BS coil was tuned to 3.36 MHz ( $\Delta \omega_{RF} = 70\text{kHz}$ ), and oriented orthogonally to the Rx/Tx coil (see Figure 7-3).

To test the 1D encoding along  $x$ , a sample consisting of two 2 mm diameter

tubes of water was used with the tubes either aligned along the encoding direction or orthogonal to the encoding direction.

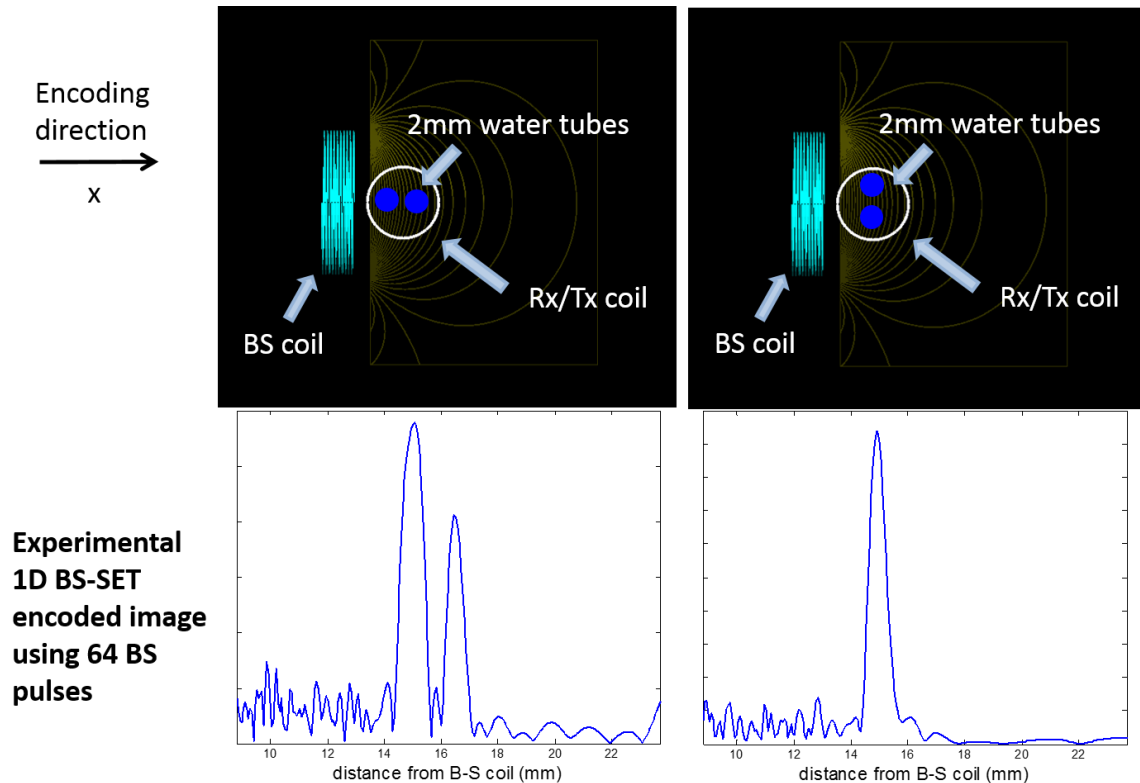


Figure 7-3: A schematic of the BS-SET experiment is shown on the top, and the resulting 1D images are shown on the bottom. The BS coil produces an approximately linear  $|B_1|$  field along the encoding direction,  $x$  (simulated flux lines are shown in yellow), which imparts a spatially varying phase along  $x$  in the sample. The encoding phase allows 1D images to be formed in which the 2 lumps are seen when the 2 water tubes are spaced along  $x$ , and 1 lump is seen when the sample is rotated  $90^\circ$ .

The pulse sequence depicted in Figure 7-2, was used with 32 BS pulse played on each side of the  $180^\circ$  excitation pulse (total of 64 encoding points). The  $B_1$  shape of the simple BS coil is approximately linear in the sample region, which unfortunately results in a non-linear phase distribution. This mean that k-space formalism is not valid, but the analogous k-space points can be reconstructed with a brute force encoding matrix method.

To map the BS  $B_1$  field and calibrate the encoding matrix, a field probe (similar to those described in Section 3.6) attached to a linear translation stage was used. The field probes was translated to a known distance ( $x_{cal}$ ) from the BS coil, and the

pulse sequence described above was played (using the field probe in Rx/Tx mode). This was done at several measured  $x_{cal}$  values, and the analogous k-space points were FFT'd to produce the calibration “projection” data in Figure 7-4a. The correlation of the peak locations in the distorted 1D images to the actual  $x_{cal}$  positions was used to deduce the “phase-shape” from the BS coil, and form an encoding matrix.

The encoding matrix was small for this experiment (64 x 64), so the matrix can easily be stored in memory. The 1D images in Figures 7-5 and 7-4b were reconstructed with the MATLAB LSQR function, which solves systems of linear equations (or finds the least squares solution).

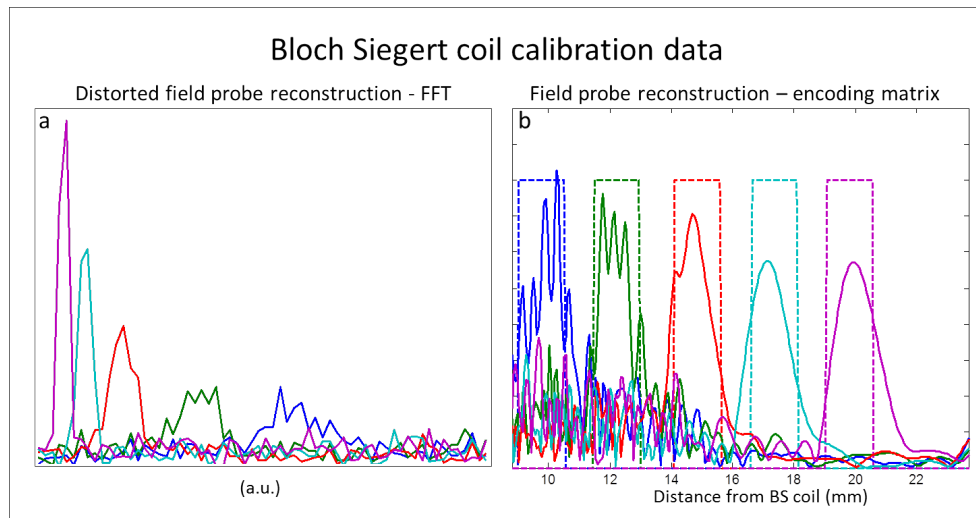


Figure 7-4: The measured field probe calibration data was used to form the encoding matrix and reconstruct the 1D profiles in Figure 7-3. (a) The 1D FTs of the data acquired from 5 field probe locations are shown. The shape and spacing of these “projections” vary because the encoding phase is non-linear (roughly quadratic). The location of the peaks, provides information about the shape of the  $B_1$  phase variation, and allows the estimation of a 1D encoding matrix. (b) When the field probe data is reconstructed with the encoding matrix, the 1D images (solid lines) overlap with the known field probe locations (dotted lines).

#### 7.1.4 Future Direction

We plan to continue this work, and combine Bloch-Siegert encoding ( $x$  direction) and rSEM encoding ( $y - z$  plane) for 3D imaging of larger phantoms. We will attempt to design a BS coil with a  $\sqrt{x}$   $B_1$  magnitude shape, so that efficient Fourier imaging

can be done along the  $x$  direction. Further, we plan to incorporate the Bloch-Siegert pulses into a spin-echo train sequence (Figure 7-5), in which distributed BS pulses of the same length apply accumulative phase. This will allow all of encoding points to be sampled in one TR (similar to the TRASE pulse sequence discussed later). In Figure 7-5, after the first  $180^\circ$  excitation pulse, the center of k-space is acquired (green point). After the second  $180^\circ$  pulse, a BS pulse is applied which causes a spatial phase distribution, so that the acquired echo corresponds to the positive k-space point,  $k = \Delta k$ , (blue dot). The third  $180^\circ$  flips the phase and no BS pulse is applied, so  $k = -\Delta k$  (red dot). The phase is flipped back following the fourth  $180^\circ$  so that  $k = \Delta k$ , but before the echo is acquired another BS pulse is played which causes additional phase to be added, and  $k = 2\Delta k$  (yellow dot). This sequence of applying the BS pulse after every other  $180^\circ$  can be continued to fill the k-space line.

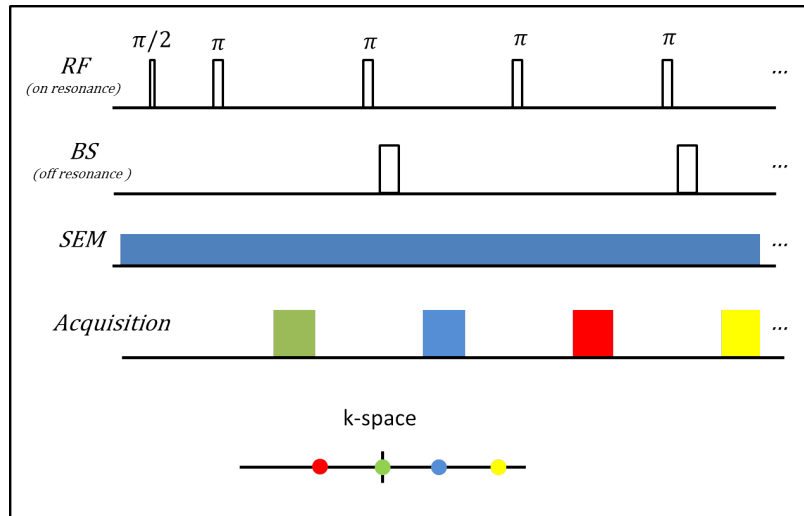


Figure 7-5: A proposed BS-SET spin-echo train sequence is shown. Identical BS pulses are played after every other  $180^\circ$  refocusing pulse. The first BS pulse applies a phase distribution, which corresponds to the first positive k-space point. The following  $180^\circ$  flips the phase corresponding to a negative k-space point. When the phase is flipped back by the following  $180^\circ$ , another BS pulse is played which applies an additive phase, corresponding to an increase in k. This is continued until the 1D k-space is filled.

## 7.2 TRansmit Array Spatial Encoding - TRASE

### 7.2.1 Theory

Another promising possibility for encoding in the 3rd dimension is Transmit Array Spatial Encoding (TRASE), which was introduced by King, Sharp, and Tomanek in 2006 as a  $B_1$  based method for traversing k-space without a phase encoding  $B_0$  gradient [122]. It has since been shown to be an effective method for gradient-free 1D or 2D MR imaging [20], [43]. It is particularly useful for low-field imaging where SAR is not a concern.

Unlike BS-SET, which requires an off-resonance  $B_1$  with a magnitude variation for encoding, TRASE uses a uniform on-resonance  $B_1$  magnitude, but linear  $B_1$  phase variation along the encoding direction (Figure 7-6a). The excitation field is expressed as:

$$B_1 = |B_1|e^{i\phi_{B_1}(x)}, \quad \phi_{B_1}(x) = G_1x = 2\pi k_1x, \quad (7.7)$$

where  $G_1$  is the physical phase gradient (in rad/m) and  $k_1$  is the corresponding k-space point. The TRASE method requires two different switchable  $B_1$  phase ramps to traverse k-space. So that:

$$B_1 = |B_1|e^{i2\pi k_1x} \quad \text{or} \quad B_1 = |B_1|e^{i2\pi k_2x}. \quad (7.8)$$

We will assume that  $k_2 = -k_1$  for simplicity, so that the sign of the spatial  $B_1$  phase ramp  $\phi_{B_1}$  varies with either a positive or negative slope with respect to  $x$ . The encoding is done during the excitation pulses with a set of  $B_1$  coils. This is different than BS-SET where a separate uniform  $B_1$  coil was used for excitation prior to the encoding BS pulses.

Spin-echo trains are used in which the sign of the linear phase variation is switched in between successive refocusing pulses. As the sign of the refocusing pulse is flipped over the course of the echo train, k-space is traversed one echo at a time. The resolution depends on the number of echoes used and the slope of the transmitted  $B_1$  phase ramp across the FOV.

## 7.2.2 Pulse sequence

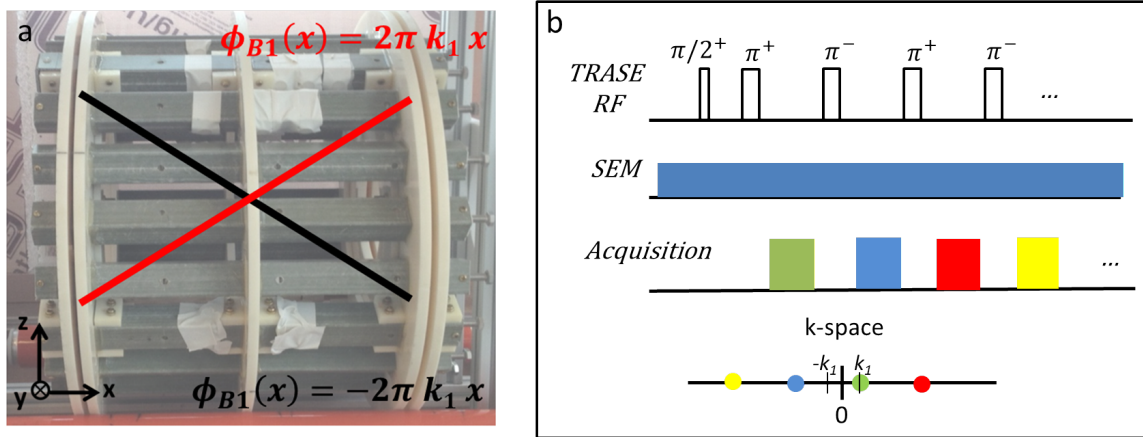


Figure 7-6: (a) TRASE encoding uses an excitation coil (or array of coils) that produces a uniform  $B_1$  magnitude, and linear  $B_1$  phase in the encoding direction. The linear phase variation ( $\phi_{B_1}(x)$ ) must be switchable during the pulse sequence. Most implementations switch between a positive linear phase variation and a negative linear phase variation. (b) The TRASE pulse sequence is based on a spin-echo train, in which the sign of the  $B_1$  phase variation is switched for every  $180^\circ$  refocusing pulse. This causes the accumulation of linear phase variation, and the traversal of k-space.

The basic TRASE sequence is shown in Figure 7-6b. The sign of the TRASE RF pulses specifies whether  $\phi_{B_1}(x) = 2\pi k_1 x$  or  $\phi_{B_1}(x) = -2\pi k_1 x$  is applied during the pulse. When the excitation pulse is played with a phase gradient, the k-space origin is no longer  $k = 0$ . Instead,  $k = k_1$  or  $k = -k_1$  are considered to be the k-space origins for the excitation pulses played with the two phase gradients. For a  $90^\circ$  pulse, the phase variation contained in the  $B_1$  pulse is simply applied or added to the phase of the precessing spins. In other words, the spins are excited to the k-space origin of the coil. When a refocusing pulse is played, the current k-space point is reflected about the transmit coil's k-space origin. TRASE requires the use of spin-echo trains excited with with alternating phase gradients to traverse k-space. In Figure 7-6, the first  $180^\circ$  pulse applies a positive linear phase variation along  $x$ , so that the acquired echo corresponds to the k-space point,  $k = k_1$  (green dot). The second  $180^\circ$  pulse is applied with the negative phase variation. This  $180^\circ$  pulse flips the current k-space point about the associated k-space origin,  $k = -k_1$ , so the resulting k-space point is  $k = -3k_1$  (blue dot). The same happens with the third  $180^\circ$  is played with the

positive phase gradient, the k-space point  $-3k_1$  is flipped about the positive k-space origin  $k_1$ . This results in a an acquired echo which corresponds to a phase twist of  $k = 5k_1$  (red dot). The spin echo train continues with alternative sign refocusing pulses to traverse k-space.

The spacing between the k-space point is:  $\Delta k = 4k_1$ . This means that the FOV in the encoding direction is:  $FOV = \frac{1}{\Delta k} = \frac{1}{4k_1}$ . If an FOV of 20 cm is desired for human head imaging, then we want  $k_1 = \frac{1}{4 \cdot FOV} = 0.0125(\frac{1}{\text{cm}})$  or  $G_1 = 2\pi k_1 = 0.078(\frac{\text{rad}}{\text{cm}})$ . The resolution is determined by the FOV divided by the length of the echo train.

### 7.2.3 TRASE coils

There are several approaches to designing an excitation coil array that produces a uniform amplitude  $B_1$  with a switchable  $\pm$  linearly varying phase [123], [124], [20], [43]. However, none of the previously reported coil designs were well-suited for our geometrical constraints.

We have designed a geometrically suitable TRASE array that consists of two nested cylindrical coils. Coil 1 is a relatively short multi-turn birdcage coil [125]. This coil produces a  $B_1$  field in the  $y$  direction, but falls off with an approximately cosine shape in the  $x$  direction with a spatial frequency of  $2\pi k_1$ . Coil 2 is a maxwell coil composed of oppositely wound 10 turn loops. This coil produces a  $B_1$  field in the  $x$  direction, and has an approximately sinusoidal shape in the  $x$  direction with a spatial frequency of  $2\pi k_1$ . The equations describing the TRASE coils are below:

$$\text{Coil 1 (birdcage): } B_{1y}(x) = |B_{1xy}| \cos(2\pi k_1 x)$$

$$\text{Coil 2 (Maxwell): } B_{1x}(x) = \pm |B_{1xy}| \sin(2\pi k_1 x)$$

$$\text{Combined: } B_1(x) = |B_{1xy}| \cos(2\pi k_1 x) \pm i |B_{1xy}| \sin(2\pi k_1 x) = |B_{1xy}| e^{\pm i(2\pi k_1 x)}$$

When the two coils are nested with an equal  $|B_{1xy}|$  magnitude, and spatial frequency,  $k_1$ , they produce  $B_1(x) = |B_{1xy}| e^{i(2\pi k_1 x)}$ . If the sign of the coil 2 is changed by with the addition of a  $180^\circ$  RF phase shift, then  $B_1 = |B_{1xy}| e^{-i(2\pi k_1 x)}$ . This means

a console controlled  $180^\circ$  phase shifter can be used to switch the sign of the phase gradient during the spin-echo train.

Figure 7-7 shows the Biot-Savart simulated fields of the coils and a photo of the constructed array. The birdcage coil has 12 rungs, a 18 cm diameter, and a 22cm length. The Maxwell coil has 22 cm diameter and a 18 cm length. A 3D printed polycarbonate former is used for the coils, which can be bolted to the magnet. This is necessary because the birdcage coil (coil 1) must be rotate with the magnet because the direction of the  $B_1$  field should be in the  $y$  direction which changes with magnet rotation. In simulation, these coils produce a field of view of  $\approx 20$  cm.

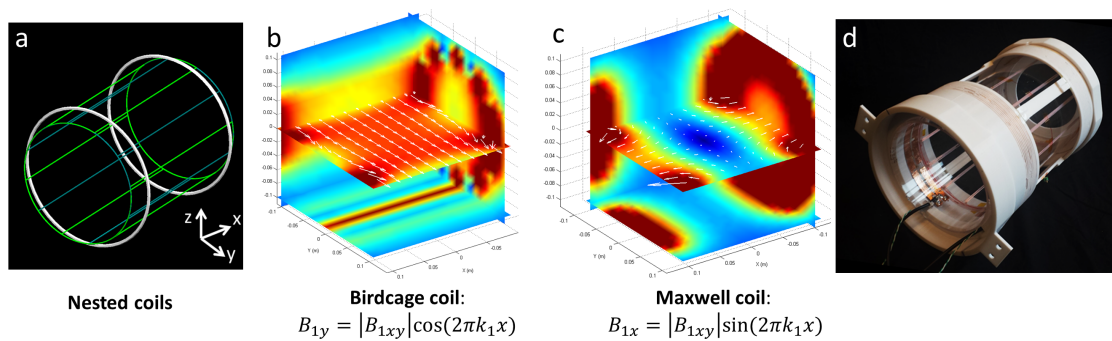


Figure 7-7: The  $B_1$  simulations of the TRASE coils were performed with Biot-Savart software (Ripplon Software Inc.) (a) Drawing of the nested TRASE coils: birdcage coil in green/blue (12 rungs, 18cm diam, 22cm length), Maxwell coil in white (22cm diam, 18cm length). (b) The simulated  $B_1$  field from Maxwell coil is shown. (c) The simulated  $B_1$  field from birdcage coil is shown. (white arrows show vector direction of field) (d) The constructed TRASE coil array is wound on a 3D printed polycarbonate former and acrylic tube. The coil former bolts to the Halbach magnet so that the coils can rotate with the magnet.

## 7.2.4 Future Direction

TRASE imaging experiments are an area of current research. One challenge, is the high level of inductive coupling between the TRASE coils. Coupling causes resonant peak splitting and therefore a poor power match with the amplifier, resulting in power reflections and inefficiency. Additionally, coupling between the coils results in undesirable  $B_1$  field patterns. As geometric decoupling between the maxwell coil and

birdcage does not seem to be sufficient, coil decoupling networks are being developed to solve this problem [126].

### 7.3 Conclusion

The development of the 3rd axis encoding method is the current research focus of this ongoing project. Although 3D images have not been obtained yet, the two described  $B_1$  encoding methods are promising. However, it is possible that these methods will require a high level of peak RF power because of the inefficiency of the coils. For the Bloch-Siegert Spatial Encoding Technique, the analogous  $\Delta k$  term and the minimum obtainable FOV depend on the nutation frequency of the BS coil, which is dependent on the efficiency of the coil and the available RF power. For the Transmit Array Spatial Encoding, in theory, no extra RF power is needed, since the spin-echo train pulse sequence does not contain extra pulses. However, the efficiency of the coil array is questionable. While the Maxwell pair should be relatively efficient when many turns are used, we found that the number of turns are limited in practice by the parasitic capacitance between the windings. The birdcage coil, which traditionally consists of a single turn (or constructed with copper tape), is more of concern because of its low  $B_1$  efficiency. In effort to increase the efficiency, an unusual multi-turn birdcage design was used [125], but again the number of turns was limited by parasitic capacitance. In addition, the multi-turn birdcage is less symmetric and less rigid than a traditional birdcage coil, which is likely contributing to the lack of geometric decoupling between the two TRASE coils.

These are issue that we can overcome in theory with a combination of decoupling networks, high power RF amps, and frequency swept  $B_1$  pulses which may require less peak power. However, if we find the  $B_1$  encoding method to be impractically complex, a traditional  $B_0$  gradient ( $G_x$ ) could be added along the  $x$  direction to allow conventional encoding methods. The foreseen complication with this method is the large gradient amplifier needed to create a linear  $G_x$  fields that is large compared to the Halbach SEM.



# Chapter 8

## Future Directions and Conclusion

### 8.1 Summary of Work

The benefits of neuroimaging with MRI are clear, but the hardware used in conventional scanners is expensive and difficult to site and maintain. Because of these limitations, the basic technology is generally underutilized, and only feasible in high-end healthcare settings. Simplifying the MRI hardware and re-envisioning the image encoding method for a specialized portable brain scanner could impact several applications/markets. The specialized scanner could be used for the following applications: traumatic brain injury imaging in the battle-field or in rural clinics, post-surgery monitoring in ICUs, frequent follow-up imaging in neuro-oncologist offices, hydrocephalus detection and monitoring in the developing world.

The main contributions of this thesis are summarized below:

- A 2D encoding method without gradient coils was introduced. The method is based on traditional MRI projection imaging, but the encoding magnetic field is built into the  $B_0$  magnet and physically rotated to produce projections. This rotating spatial encoding magnetic field (rSEM) method allows arbitrary SEMs to be used for projection imaging, and allow the inhomogeneities of a lightweight magnet to be a benefit rather than a problem. The data sets are referred to as “generalized projections” because unlike traditional projection imaging there is

not necessarily a linear mapping between Larmor frequency and position.

- The rotating  $B_0$  magnet with a built-in SEM was designed and constructed. A lightweight Halbach cylinder design composed of sparsely spaced NdFeB magnet rungs was used. The average  $B_0$  field strength of 77 mT provides adequate SNR for our target applications. The built-in SEM of the shimmed magnet results in a manageable Larmor frequency bandwidth. The encoding ability of the SEM is impressive at the periphery, but problematic in the center. The “encoding hole” in the center is caused by the shallow gradient of the approximately quadrupolar SEM.
- A combination of non-linear SEM methods and inhomogeneous NMR methods were applied to acquire 2D images. This includes the use of multiple receiver coils to prevent aliasing from the non-bijective encoding field. Spin-echo refocusing and broadband excitation pulses were used to cope with the inhomogeneous field from the permanent magnet SEM.
- Although generalized MRI reconstruction methods are abundant in the literature, the encoding matrix calibration of this system is unique. The calibration was accomplished by the careful estimation of the rotated SEMs applied to the object over time. This is complicated by field drift with temperature and the sensitivity of the SEM to external fields. In addition, the estimation of the complex coil sensitivity profiles was unusual because: 1) it was impossible to measure the sensitivities with traditional methods, 2) the sensitivity profiles change as the magnet is rotated.
- 2D image simulations using the rSEM encoding method were done to show spatially varying resolution for various SEM shapes. This process will direct subsequent magnet designs.
- The use of  $B_1$  encoding methods to enable 3D imaging was discussed. The initial work towards the use the Bloch-Siegert Encoding Technique (BS-SET) and Transmit Array Spatial Encoding (TRASE) was shown.

- 2D MRI images of phantoms and fruit were produced using the rSEM encoding method (without the use of gradient coils).

Although significant progress has been made, the long-term goal of this project is to produce a fully functional prototype brain scanner. Current and future work towards accomplishing this goal is described below.

## 8.2 Future Directions

### 8.2.1 3D encoding

Currently, only 2D images of thin samples are possible. The most pressing area of future work is the implementation of 3D imaging. The plans for this were presented in Chapter 7.

### 8.2.2 Halbach Magnet - version 2

We plan to use the 2nd magnet iteration in a prototype scanner for human brain imaging. Experience with the magnet construction process and imaging experiments has provided a plethora of possible magnet improvement ideas, but the basic design changes are as follows:

1. Bore access: In the current design, bore diameter is about 32 cm inside the magnet, but the bore access at the end is limited to 23 cm because of the additional Halbach end rings and extra ABS support material. The bore access size must be increased to allow the RF coils and an average human head to be inserted.
2. SEM shape: For the first magnet design, the SEM was not optimized, and the natural resulting field variation was used for encoding. The impact of SEM shape on image resolution was discussed in Chapter 6, and it was concluded that a significant linear term must be included to prevent an “encoding hole” at the center. Instead of designing the magnet to include the optimal SEM, we will

aim to maximize homogeneity in the initial design stage. We expect that even with careful design and shimming, 2nd and 3rd-order polynomial terms will be significant due to the geometrical constraints. However, we aim to reduce the intrinsic variation as much as possible, and then add in the desired SEM shape with shim magnets.

Unfortunately, increasing the array diameter of the current Halbach magnet rungs results in dramatically decreasing the field strength. If we want to increase the inner diameter,  $r_{in}$ , by 10%, but maintain the same  $B_{ave}$ , the outer diameter,  $r_{out}$ , must also be increased by 10%, but the same density of magnet material must be maintained. In addition, the homogeneity along the cylindrical axis is reduced when the diameter increases with respect to length [72].

It will be necessary to use more magnet material to maintain  $B_{ave}$  and a reasonable homogeneity. This will unfortunately result in at a least 2 times the current magnet weight. The current design plan, is to increase the array radius ( $r$ ) to 20 cm instead of 18 cm, and use 2 layers of  $N = 24$  rungs instead of 1 layer of  $N = 20$  rungs.

To compensate for the fringe field, we plan to increase the length of the magnet rungs above the patient’s head. This will results in an off-center brain location, so a booster Halbach ring will be added to the bottom (neck end) of the array while the top end remains open. In this scheme, the RF coils will be inserted from the top of the magnet array, and only the patient’s head will be inserted from the bottom of the magnet (where the diameter is decreased by the “booster ring”). An example of this design idea is show in Figure 8-1a.

The booster ring may not sufficiently improve the  $x$  homogeneity in the magnet. Therefore, the design will likely include intentional gaps between magnet pieces to smooth out the variation along  $x$ . This idea is similar to the method used by Danieli et al. in [68] and Soltner et al. in [71], in which the homogeneity of the NMR Mandhala was improved by optimizing the spacing of the stack of Halbach rings. This could be extended to include a large gap in the second layer of rungs, turning the 2nd layer into “booster rings”. An example of this design is shown in figure 8-1b. The optimization of the cylinder length ( $l$ ) and the magnet gap positions is ongoing.

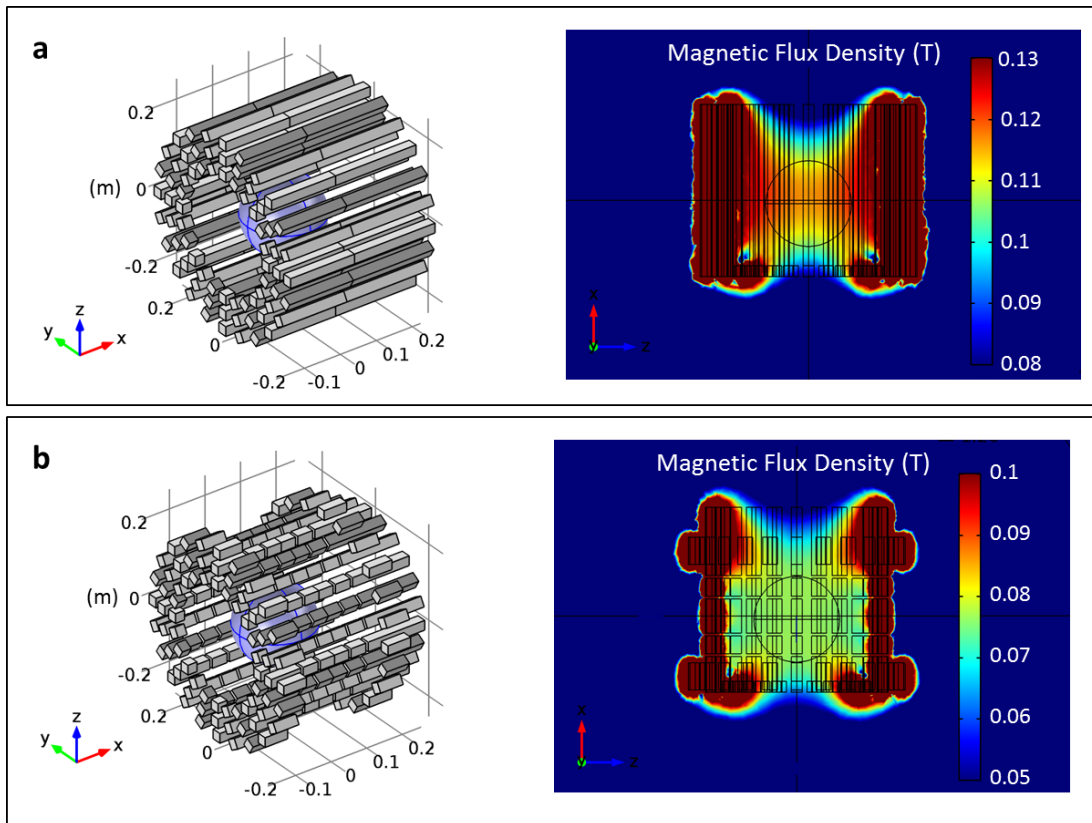


Figure 8-1: Two magnet design simulations are shown with an increased bore size. Both designs include 2 layers of 24 magnet rungs. Layer 1 has a diameter of 40 cm, and layer 2 has a diameter of 44 cm. The length of the rungs is increased to 16" instead of the original 14". A Halbach "booster ring" made up of 24 1x1x1" magnet pieces with a 32 cm diameter is added to the bottom end. The design in (b) includes several gaps in the magnet rungs to increase homogeneity along  $x$ .

### 8.2.3 Patient table design

The next magnet design will be incorporated into a scanner assembly prototype, which includes a separate scanner cart and patient table. The currently proposed design is shown in Figure 8-2. The scanner cart and patient table can independently be moved freely, but connect together with aluminum guides. The scanner cart will hold the magnet, magnet rollers, motor, and additional hardware for holding coils. The patient table will include a support piece for the patient's head which hangs over the end of the table. This piece is necessary for inserting the patient's head into the scanner without moving the patient. This may be an important requirement for post-surgical patients or trauma patients.

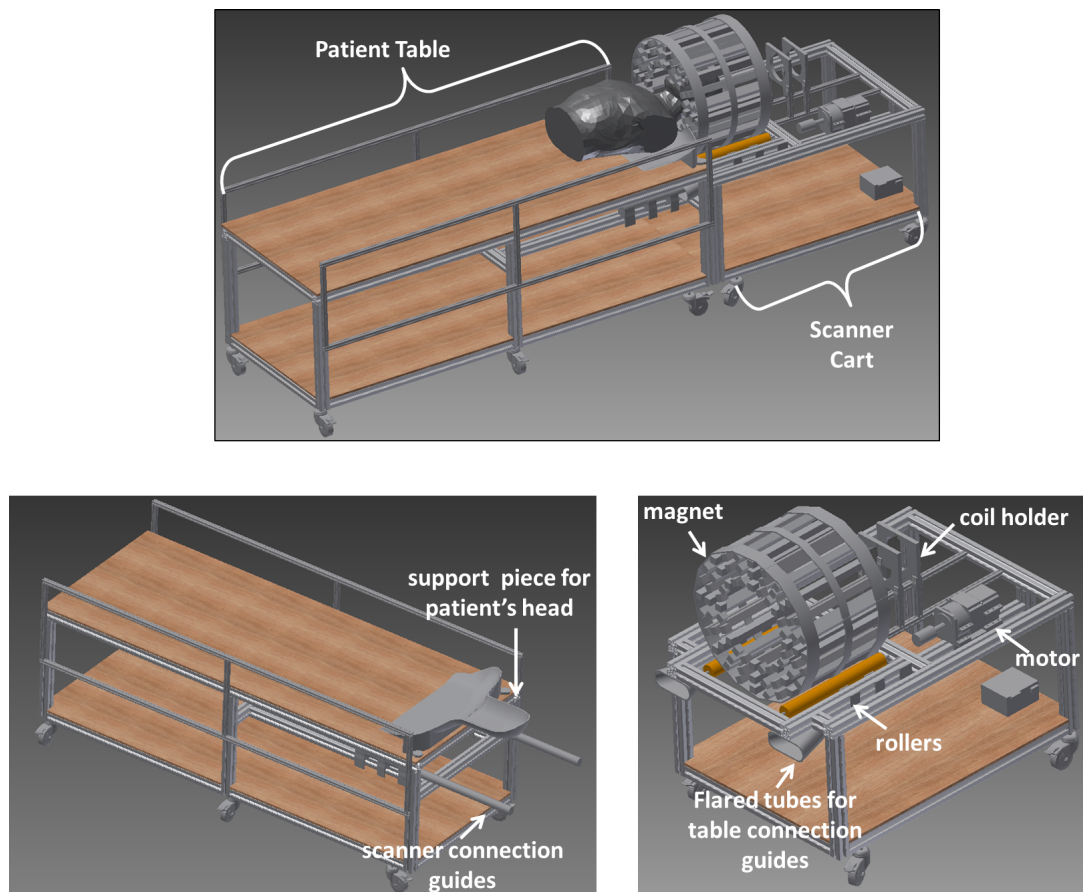


Figure 8-2: A CAD drawing of a prototype scanner assembly with a separate scanner cart and patient table that fit together for human brain imaging.

### 8.2.4 Parallel imaging

Currently, the use of a console with only 1 receiver channel prevents parallel data acquisition from multiple coils. Serially acquiring from 8 surface coils and 1 field-tracking probe requires  $9\times$ 's the acquisition time, resulting in  $> 1$  hr total image acquisition times. The use of parallel imaging is a necessity for in vivo brain imaging with this system, and will require either building a multi-channel FPGA-based console, or purchasing one.

In addition, pre-amplifier decoupling must be implemented to prevent coupling in the coil array. Pre-amplifier decoupling is achieved by inserting a high impedance in the coil loop to decrease current and therefore mutual inductance and coupling. This is done by connecting one of the tuning capacitors through a series inductor to a low-impedance pre-amplifier ( $\approx 1\Omega$ ). This low-impedance effectively shorts the inductor creating a resonant LC circuit, which is tuned to the Larmor frequency. The resonant LC circuit appears as a high-impedance in the coil. Despite this, the coil circuit is still noise-matched at a higher impedance to the pre-amplifier.

A Rx coil array will be built on a helmet former. The array will consist of 16-32 coil elements to achieve maximum coverage of the brain and SNR. Figure 8-3a shows an initial helmet design with 32 surface coils. The coil former helmet is designed to allow the patient to horizontally slide into the coil while remaining stationary on the head-support piece, this is demonstrated in Figure 8-3b.

## 8.3 Conclusion

Using an inhomogeneous magnet for spatial encoding in lieu of gradient coils, we have constructed and demonstrated a lightweight scanner for 2D MR imaging with minimal power requirements. The 2D proof-of concept images from this nearly head-sized imager show the ability of this encoding scheme to produce sufficient spatial resolution and sensitivity for the detection and characterization of many common neurological disorders such as hydrocephalus and traumatic space-occupying hemorrhages. Future work in perfecting the calibration methods is likely to bring experimental image qual-

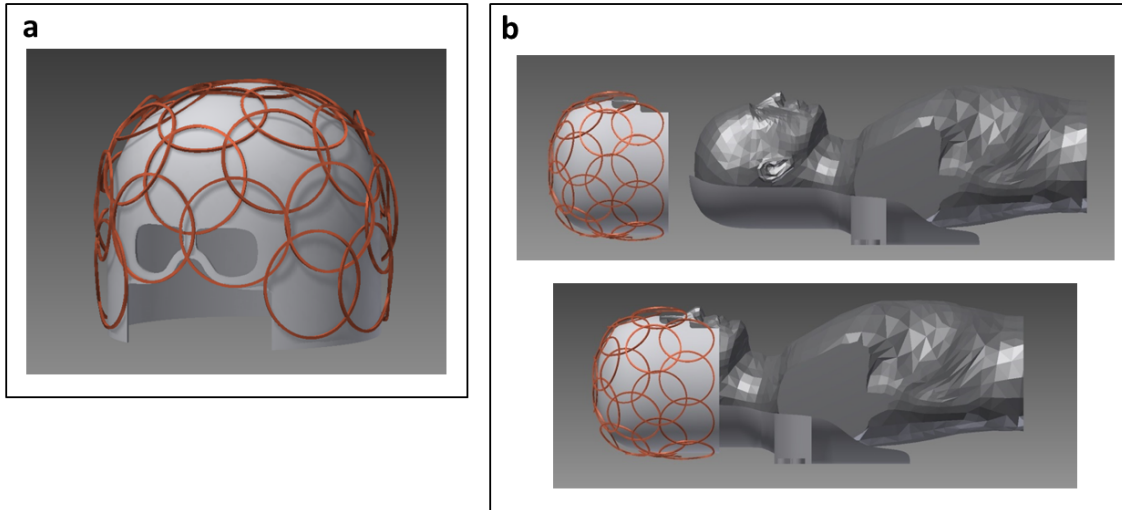


Figure 8-3: (a) Initial design of the plastic helmet former is shown with 32 distributed coil elements. (b) The patient and the head support piece must be able to easily slide into the coil.

ity closer to the theoretical limit, but the resolution of the current system is sufficient for identifying gross pathologies. With the future implementation of true parallel imaging and 3D encoding, this scanner has the potential to enable a truly portable, low-cost brain imaging device.

# Chapter 9

## Implementation of low-cost, instructional tabletop MRI scanners

### 9.1 Introduction

While many courses teach the principles of Magnetic Resonance Imaging, the hardware composing the MRI scanner often seems like a black box because the cost and complexity of clinical scanners prevents a hands-on learning approach. Dedicated instructional MRI scanners are useful for understanding MRI physics, hardware, and data acquisition and processing. Additionally, MRI scanners are interesting tools for teaching general applied engineering topics.

A collaborative effort was made to design and build a set of small low-cost educational MRI scanners with a budget of \$10K per system. While there are some commercially available educational scanners [51], none are available near this price point. Additionally, we intended to create an MRI scanner with an open parts list and library of pulse sequences which could be further improved by motivated students. Unlike the previously described rSEM brain imager, these systems were designed to model traditional MRI scanners and perform Fourier MR imaging.

The goal was to produce 20 fully functional MRI scanners with a 1 cm<sup>3</sup> imaging volume. The scanners were designed to fit on a projector cart so that they could easily be moved around a teaching lab. The scanners have been used in two cycles

of an MIT undergraduate EECS course: “Intro to EECS from a Medical Technology Perspective” by over 200 students, as well as a graduate course focused on MRI data acquisition and reconstruction. The scanners are used to teach basic concepts in data acquisition, computer control of experiments, signal processing, and Fourier analysis. Pulse sequences programming and data processing is done in MATLAB. The scanners are also used to teach basic MRI concepts like free induction decay, flip angle measurement,  $B_0$  shimming, gradient-echo, spin-echo, 1D projections, and 2D/3D Fourier imaging.

### 9.1.1 Overview of Scanner

The scanners were built with a combination of off-the-shelf electronics and in-house developed components. Figure 9-1 shows a photo of one of the 20 complete educational scanners with major components distinguished with arrows.

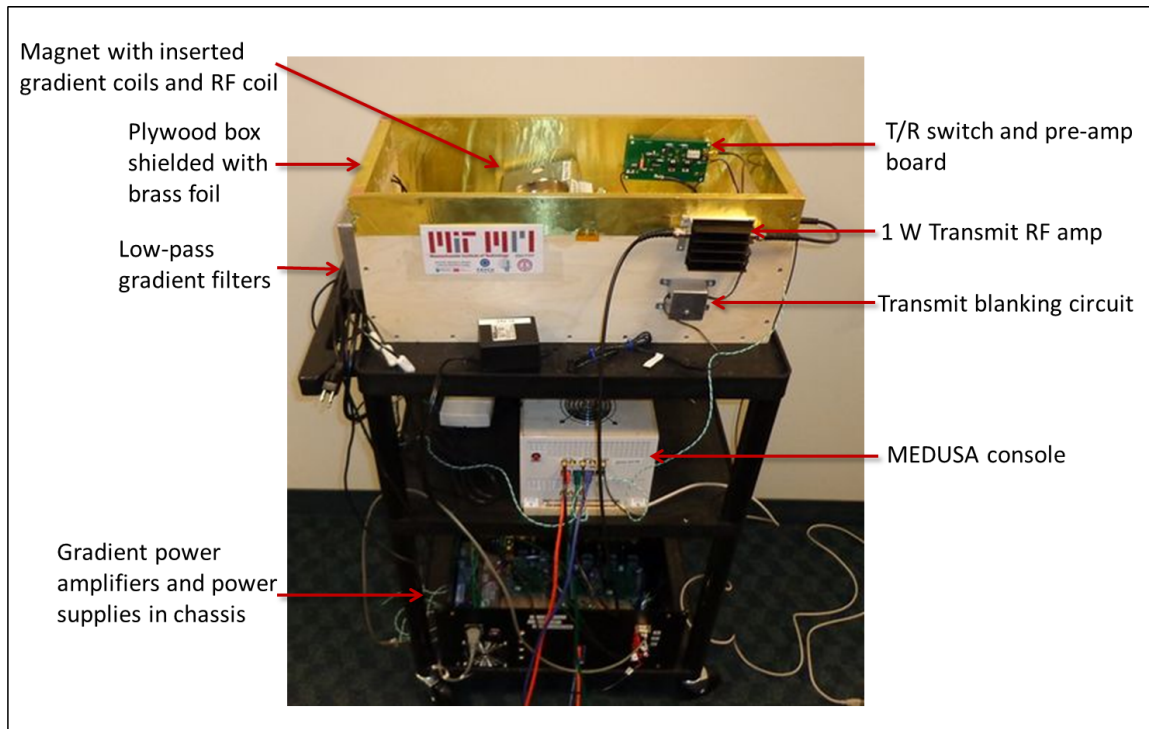


Figure 9-1: The complete instructional MRI scanner is shown on a projector cart.

This scanner is used to do traditional Fourier imaging, so all of the conventional MRI scanner components are included. A permanent magnet is used to create the

0.18 T  $B_0$  field. A MATLAB controlled console is used to produce the RF pulses, acquire the MR signal, and produce gradient waveforms. The gradient waveforms are amplified by gradient power amplifiers (GPAs), and then filtered to remove noise before supplying current to the gradient coils. Linear gradient fields ( $G_x, G_y, G_z$ ) are generated from shielded planar gradient coils incorporated into PCB boards. The excitation pulses from the console are amplified by a 1 W power amplifier, and passed through a transmit/receive (T/R) switch before the RF coil. The solenoidal RF coil, which is used for transmit and receive, is tuned to  $f_0 \approx 8.1$  MHz. The Faraday detected MR signal is amplified by a series of pre-amplifiers, and then passed through the T/R switch to the analog-to-digital converter (ADC) in the console.

Graphical User Interfaces (GUIs) were created for each of the prepared lab exercises for the students. MATLAB was used to program the console, and the acquired data was stored in the work-space. This allowed students to save and analyze data in MATLAB as well. Detailed descriptions of the scanner components and GUIs follow.

## 9.2 Magnet - $B_0$ field

The permanent  $B_0$  magnets shown in Figure 9-2 were produced by the Chinese Academy of Science. The  $B_0$  field is about 0.18 T with 50 ppm homogeneity in the center 1 cm diameter spherical volume (DSV). The magnets are made from two cylindrical NdFeB magnets contained by a high permeability steel yoke. The magnet geometry is sometimes referred to as a yoked two column design [2], “closed C-shaped”, or “H-shaped” [117]. Iron pole pieces are attached to the magnets inside the yoke to improve homogeneity. The gap between the pole pieces is 4 cm wide. The total magnet weight is 13 kg.

## 9.3 Console

The MEDUSA console is low cost and easy to program [127]. It was designed at Stanford University and fabricated by Procyon Engineering. The console includes

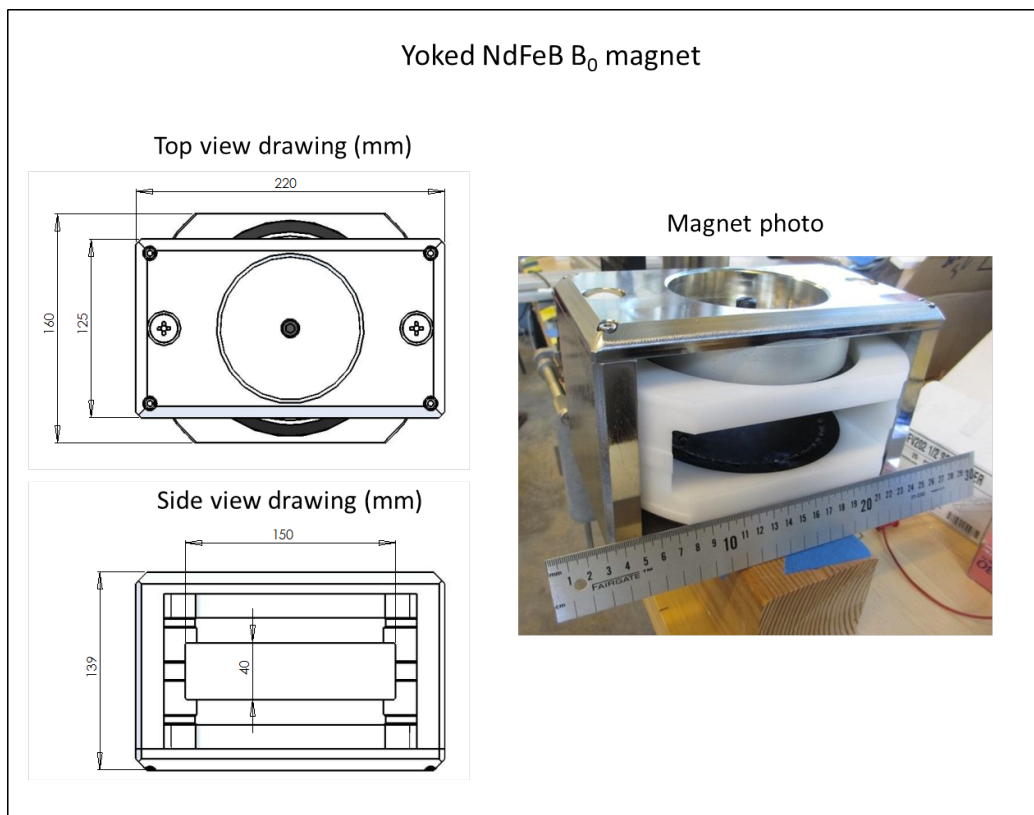


Figure 9-2: The small permanent magnet has a 0.18 T  $B_0$  field, 50 ppm homogeneity in the center 1 cm DSV. A CAD drawing of the top and side view of the magnet are shown on the left, and the photo of the magnet is shown on the right.

a controller board, RF TX/RX board, gradient waveform synthesizer, and digital-to-analog converter (DAC) boards for each gradient axis. The console does direct digital TX and Rx up to 100 MHz, and has a 60 MHz 32-bit ARM processor with 2 MB SRAM. It has four arbitrary waveform gradient outputs, a 16-bit optically isolated digital-to-analog converter, and two gating outputs. Pulse sequences are programmable in MATLAB, and allow for seamless interfacing between data acquisition and data processing. Figure 9-3 shows photos of the MEDUSA console boards, and the 3D printed and plywood housing built in-house. The housing contains all of the MEDUSA boards, except for the gradient DAC boards which were mounted in the gradient power amplifier (GPA) chassis described in section 9.4.1.

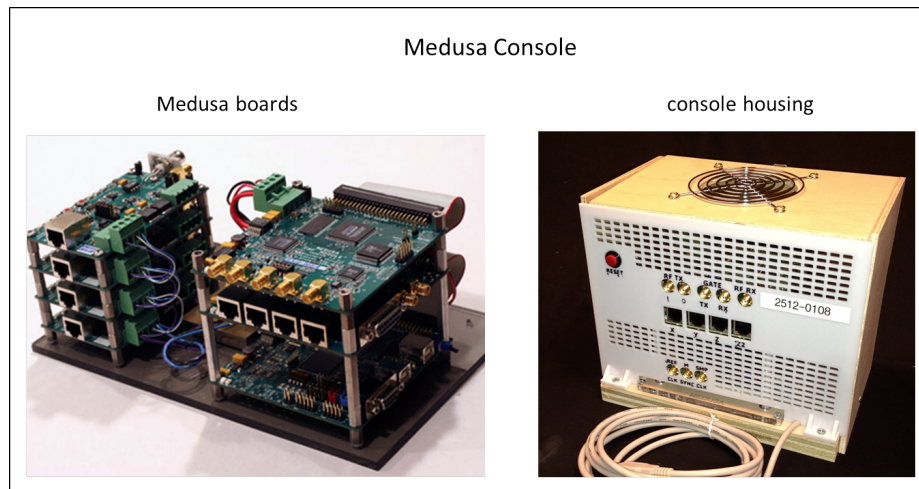


Figure 9-3: The MATLAB controlled Medusa console is used for the scanners. Left: Medusa controller board, gradient D/A converter boards, and RF Tx/Rx board. Right: The home-made console housing was built using plywood pieces, and a plastic 3D printed front panel.

## 9.4 Gradients - $G_x, G_y, G_z$

Traditional Fourier image encoding is done with this scanner using switchable linear gradient fields,  $G_x, G_y, G_z$ . The gradient waveforms are digitally produced by the console. The GPA system (with DACs) convert these digital waveforms to the appropriately amplified analog currents, which drive the electromagnetic gradient coils.

### 9.4.1 Gradient Power Amplifiers

The gradient power amplifier (GPA) is used to convert the gradient waveform from the console to a proportional current which drives the gradient coils, and produces the linear magnetic gradients fields ( $G_x, G_y, G_z$ ). It is similar to a common audio power amplifier except that it must also be able to output DC currents. The educational scanner's GPAs are low-cost, in-house constructed class-AB amplifier circuit based on TI-OPA549 (Texas Instruments, Dallas, TX) high-current operational amplifiers (op amps) in a master-slave configuration<sup>1</sup>. The voltage across a  $0.1 \Omega$  current sense resistor is used in the feedback loop to maintain a true constant current output proportional to the control input voltage. A TI-INA105 precision difference amplifier is used to buffer the current sense resistor voltage from the feedback loop. Figure 9-4 shows the GPA schematic.<sup>2</sup>

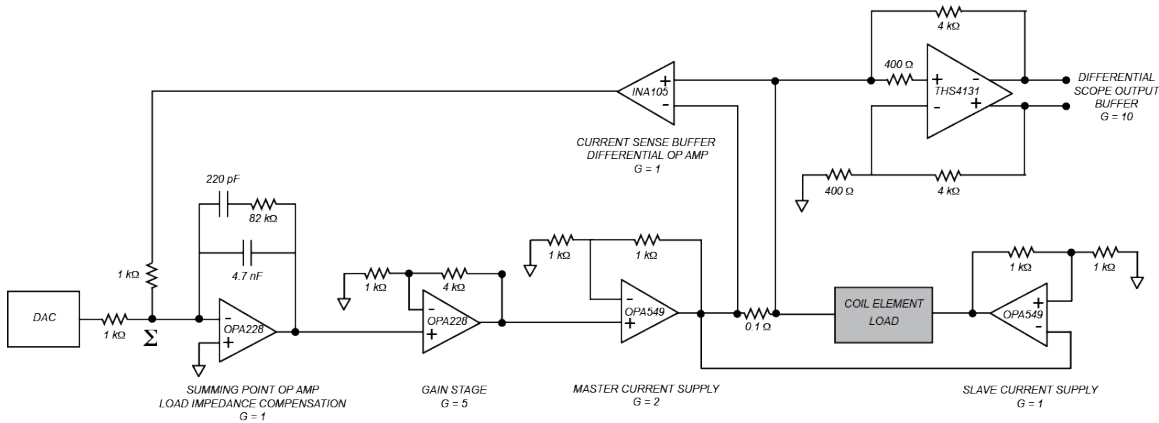


Figure 9-4: Gradient power amplifier (GPA) schematic. A master-slave op-amp configuration is used to drive the gradient coils. The voltage across a  $0.1 \Omega$  current sense resistor is buffered and used in a feedback loop to maintain a constant current output which is proportional to the voltage input from the DAC.

A differential scope output is used to monitor the buffered current sense resistor voltage. A National Instruments DAC board with PC interface is used to display the scope output signal. The GPA boards were fabricated as PCBs, and mounted in an aluminum chassis along with the power  $\pm 15 \text{ V}$  power supplies and Medusa DAC boards.

<sup>1</sup>The GPA circuit was designed by Dr. Thomas Witzel at the MGH Martinos Center

<sup>2</sup>The GPA schematic was provided by Dr. Jason Stockmann at the MGH Martinos Center.

Bench tests show that the current output tracks the input control signal with high fidelity and short achievable rise times. Driving a  $40\ \mu\text{H}$  gradient coil, the GPAs switch from 0 to 3 amps in as little as  $20\ \mu\text{s}$ .

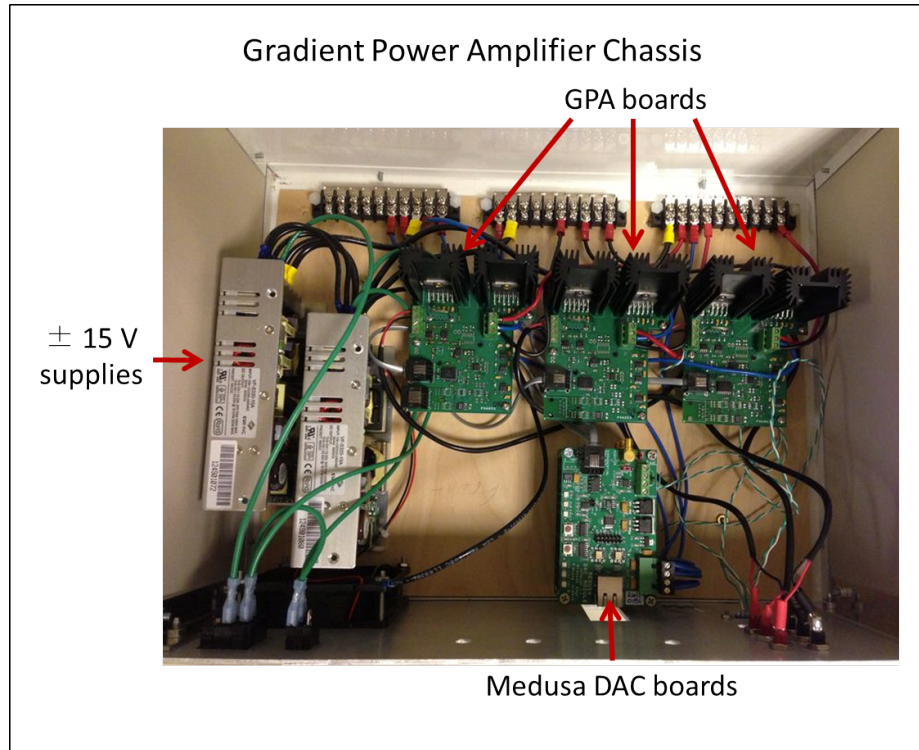


Figure 9-5: The gradient power amplifier (GPA) chassis contains the  $G_x$ ,  $G_y$ , and  $G_z$  amplifier boards (schematic in Fig. 9-4), the 15 V power supplies, and the digital to analog converter boards.

## 9.4.2 Gradient Filters

The analog current outputs from the GPA pass through gradient filters attached to the shielded scanner box. The filters are 6th-order Butterworth lowpass filters with a 2 MHz cutoff frequency, which filters each of the differential gradient coil lines and prevent high frequency RF noise from entering the shielded box. The schematic and board layout are shown in Figure 9-6.

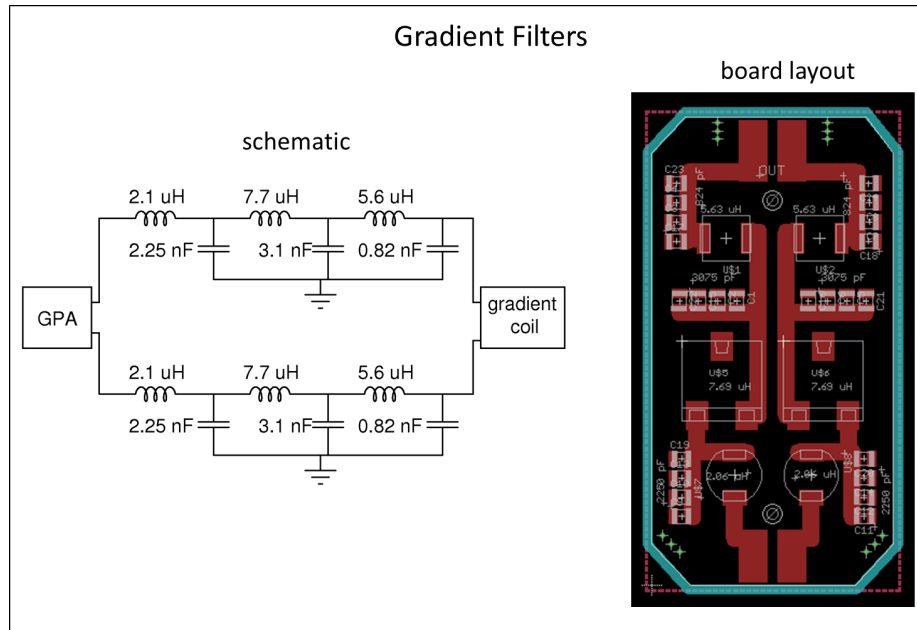


Figure 9-6: The gradient filters are 6th order Butterworth low-pass filters with a 2 MHz cutoff frequency. They prevent the gradient coils from producing spurious high frequency noise.

### 9.4.3 Gradient coils

Air-cooled gradient coils were fabricated as printed circuit boards (PCBs). The gradients were implemented as shielded planar coils, with two primary coils and two shielding coils for the X, Y, Z, and Z2 terms<sup>3</sup>. The current traces for producing the gradient fields were designed by University of Freiburg Medical Physics Group. The traces were incorporated into an 8-layer PCB layout with buried vias and 4 oz/ft<sup>2</sup> copper traces<sup>4</sup>. The copper traces for the X, Y, and Z primary and shielding coils are shown in Figure 9-7. A plastic 3D printed frame was designed to stack and space the PCBs properly in the magnet. The shielding coils were placed  $\pm 2$  cm from isocenter (against the magnet poles), and the primary gradient coils were spaced  $\pm 1$  cm from isocenter. The gradient coil stack with plastic frame is shown in Figure 9-7. The gradient fields produced by the coils per amp are: X: 13.7 mT/m/A, Y: 10.4 mT/m/A, Z: 12.3 mT/m/A.

<sup>3</sup>The Z2 coil was included for  $B_0$  shimming, but has not been utilized yet

<sup>4</sup>This PCB layout was done by Dr. Cris LaPierre at the MGH Martinos Center

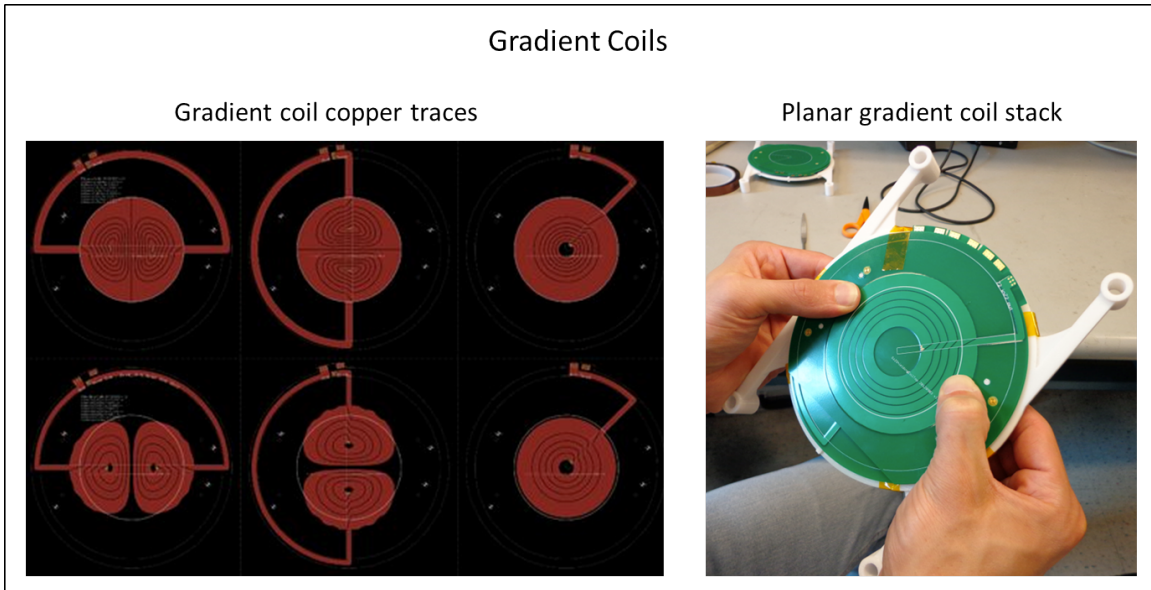


Figure 9-7: The shielded planar gradient coils were fabricated as PCBs. Left: Copper traces for X, Y, and Z gradient coils. Right: Photo of gradient coil stack to be inserted in magnet gap.

## 9.5 RF Subsystems

The RF subsystem is summarized in Figure 9-8.

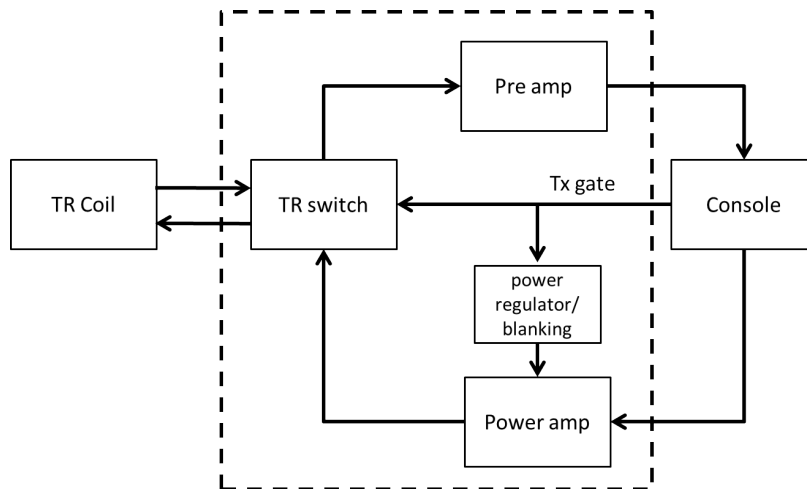


Figure 9-8: Block diagram of RF subsystem.

### 9.5.1 RF coil

A single RF coil is used for both producing excitation magnetic field pulses (transmit) and for Faraday detection of the MR signal (receive). The coil is a 12 mm diameter, 8 turn solenoid tuned to  $f_0 \approx 8.1$  MHz.<sup>5</sup> The imaging phantoms (water filled plastic inserts) and biological samples (mouse brains and hearts) fit into 1 cm diameter NMR tubes, which tightly fit into the solenoid. A plastic rectangular coil and sample holder was 3D printed, and wrapped in copper foil for RF shielding (Figure 9-9). The high filling factor of the coil, and the copper shielding improve the SNR.

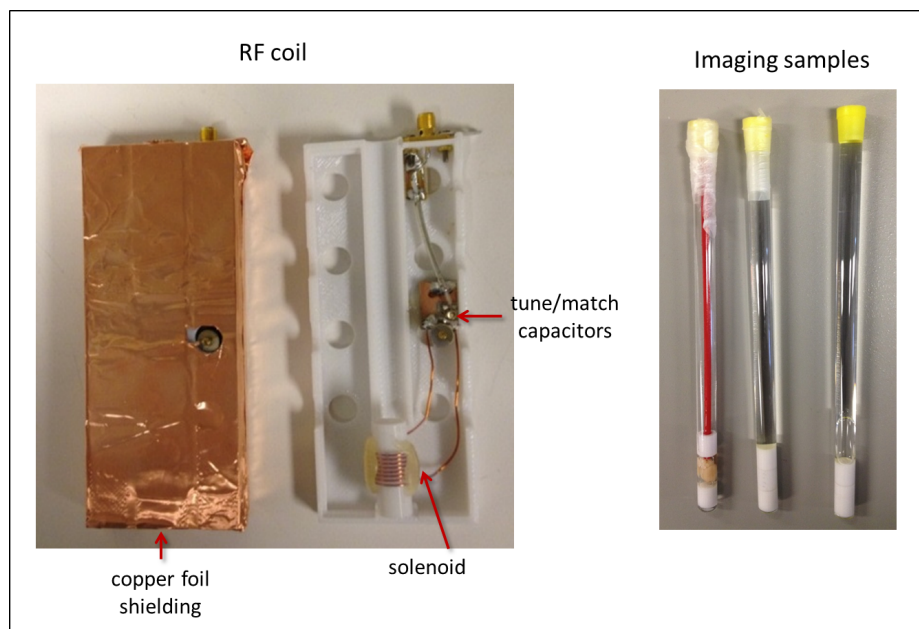


Figure 9-9: Left: The RF transmit/receive coil is a 1.2 cm diameter tuned solenoid. The coil is mounted in an RF shielded box. Right: The imaging samples are contained in 1 cm diam. NMR tubes, which fit snugly in the coil.

### 9.5.2 Transmit pulses

The console produces the RF excitation pulses in the pulse sequence. The RF pulses are amplified by a Mini-Circuits ZHL-3A 29.5 dBm ( $\approx 1$  W) amplifier with 24 dB gain. The console also outputs a gating signal, which is high during the RF pulses

<sup>5</sup>The  $B_0$  field strength varied slightly among the 20 scanners. The coils were individually tuned to match the Larmour frequency of the designated scanners.

(Tx gate). These pulses are used to control the T/R switch (described below) and the power amplifier blanking circuit.

Experimentally, we encountered a streaking artifact which was mitigated by regulating the power supply to the power amplifier. We also found transmit RF was leaking through the T/R switch during the receive portion of the pulse sequence. This caused a DC artifact in the images, which disappeared when the blanking circuit was added. The blanking circuit shown in Figure 9-10, includes a voltage regulator (7824) and a simple switch which connects the supply power to the amplifier when the transmit gating signal is high.<sup>6</sup> The switch consists of a 2N3904 NPN bipolar transistor and a TIP32A PNP bipolar power transistor.

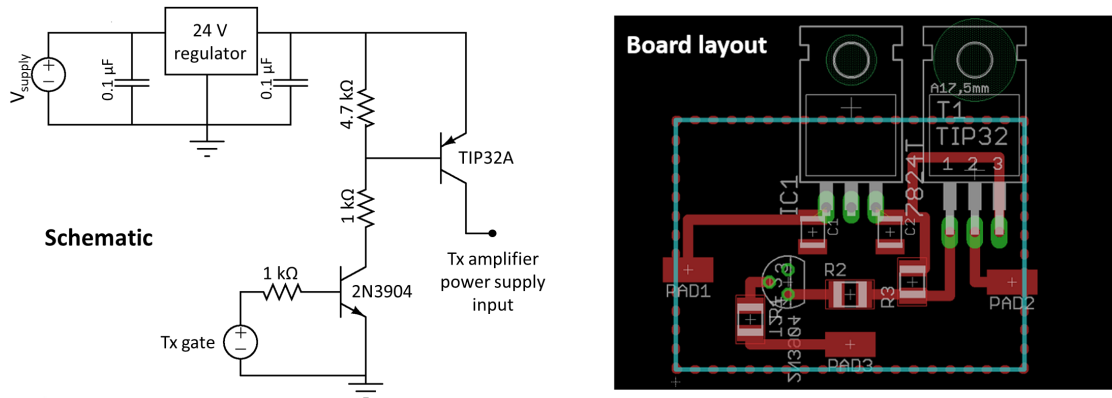


Figure 9-10: The schematic and board layout of a voltage-regulating/blanking circuit is shown. When the Tx gate signal is high (5 V during the transmit pulses), the circuit’s voltage output of 24 V is connected to the power supply input of the Mini-Circuits ZHL-3A amplifier. When the Tx gate signal is low (0 V), the power to the amplifier is “blanked” preventing any RF leak-through during the receive portion of the pulse sequence.

### 9.5.3 T/R switch and Pre-amplifier

The transmit/receive (T/R) switch and receive pre-amplifier are both included in the PCB board shown in Figure 9-11. The T/R switch effectively switches the RF coil to transmit or receive mode by connecting the coil to the “transmitter” (the output

<sup>6</sup>The blanking circuit design was suggested by Dr. Pascal Stang.

of the power amplifier) or to the pre-amplifier which then passes the signal to a low-pass filter and the “receiver” (the console ADC). The T/R switch is a classic design PIN-diode activated quarter-wave design. The PIN-diodes are biased with the Tx gate signal. When the gate signal is high (during a transmit pulse), the PIN diodes look like shorts, which means the series PIN diode directly connects the RF coil to the “transmitter”. The short impedance of the shunt PIN diode is transformed by the lumped-element quarter-wave pi-network, so that the coil “sees” an open circuit in the receiver direction. When the PIN diodes are not biased they appear like open circuits. In this case the RF coil “sees” an open circuit towards the transmitter, and is connected by the pi network to the pre-amplifier.

The pre-amplifier consists of a series of two Mini-Circuits GALI-74+ ICs (monolithic amplifiers) with 2.7dB noise figures and 25 dB of gain each. The signal is then filtered by a Mini-Circuits SCLF-10+ low-pass filter with a 10 MHz cutoff frequency, before passing to the Medusa console receiver.

## 9.6 Graphical User Interfaces (GUIs) and Lab Exercises

The MEDUSA console connects to MATLAB on a PC via a USB port, permitting easy control of tabletop imaging experiments and processing of the output data. Pulse sequence parameters are set within a MATLAB script and the RF and gradient pulse waveforms are described as vectors. MATLAB Graphical User Interfaces (GUIs) are used as “wrappers” around the code scripts in order to permit users to easily change experimental parameters, acquire data, and perform basic data processing in real time.<sup>7</sup>

The introductory experiment is the classic NMR “one pulse” sequence in which a single RF pulse is played and the resulting free induction decay is acquired (Figure 9-12).  $B_0$  shimming is performed by adjusting slider controls for the X, Y, and Z shim currents in order to maximize the length of the FID and minimize the spectral width.

---

<sup>7</sup>The GUIs were programmed by Dr. Jason Stockmann at the MGH Martinos Center

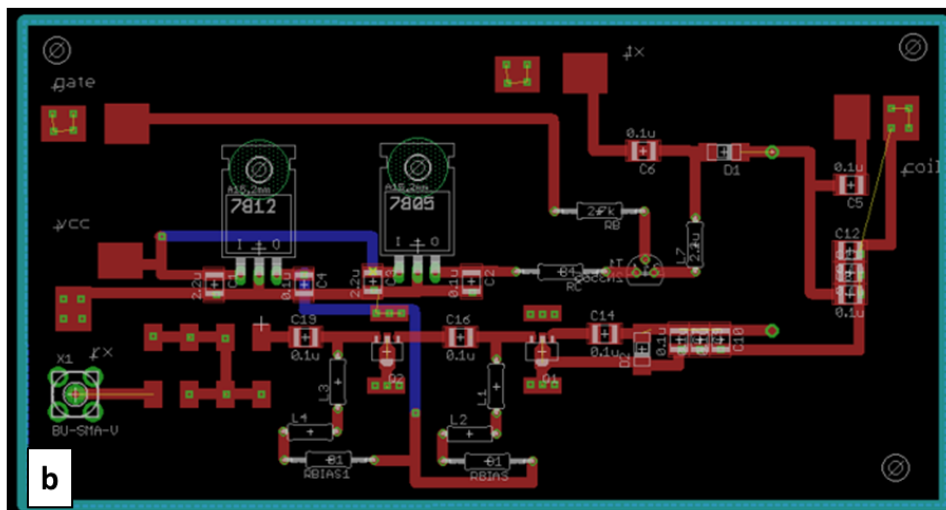
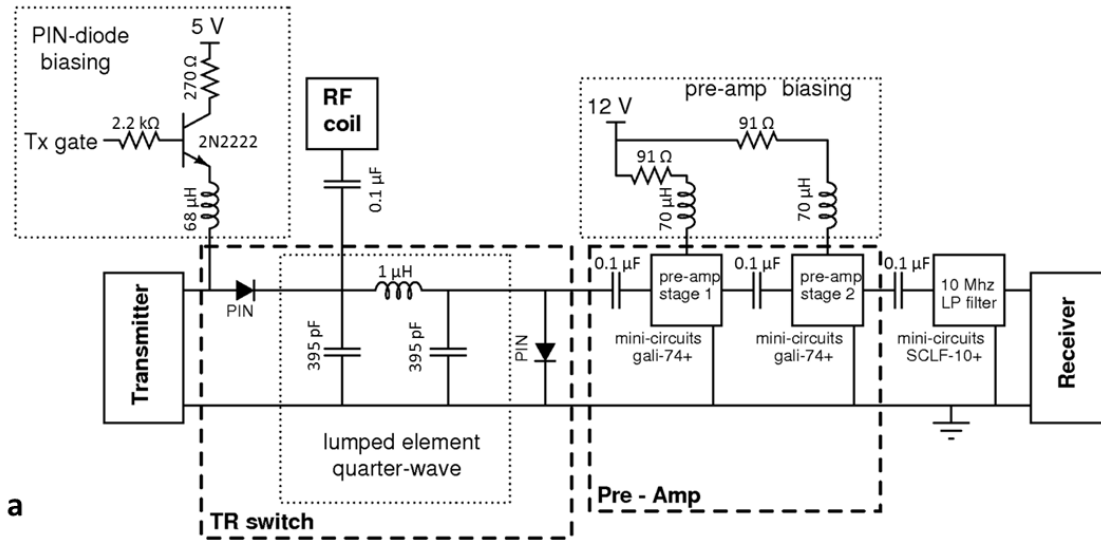


Figure 9-11: The schematic (a) and board layout (b) of the combined T/R switch and pre-amplifier circuit are shown. The T/R switch is the classic PIN-diode -  $\lambda/4$  design, but the  $\lambda/4$  transmission line is replaced with a lumped element pi-network because of the long wavelength of the operating frequency. The pre-amplifier is composed of 2 cascaded Mini-Circuits monolithic low-noise amplifiers. The output of the pre-amplifier is filtered with a Mini-Circuits low-pass filter.

Users can also perform a flip angle calibration to determine the transmit power levels corresponding to  $90^\circ$  excitations and  $180^\circ$  refocusing pulses. The GUI includes a simple SNR metric based on the ratio of the spectral peak amplitude to the spectral noise floor. Data can be saved for further offline processing.

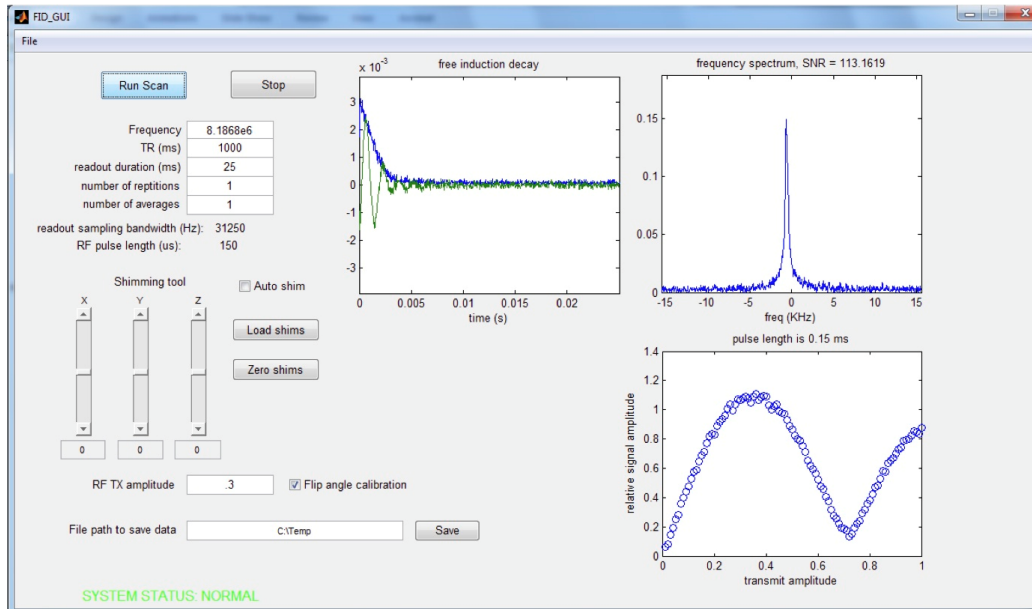


Figure 9-12: The free induction decay (FID) GUI allows users to display data in the time and frequency domain. The GUI displays the data in the time and frequency domain and includes tools for  $B_0$  shimming (left) and flip angle calibration (bottom right).

Building on the concepts illustrated in the FID GUI, the spin echo GUI (Figure 9-13) shows how spin evolution followed by a  $180^\circ$  pulse leads to refocusing. The echo-time (TE) can be varied to show how T2 decay changes the strength of the acquired echo peak. Users can apply the shim settings obtained in the FID GUI to observe how improving the shim broadens the echo and narrows the spectral line.

Users can then turn on gradient fields along a desired direction (X, Y, or Z) during the spin echo sequence. In the presence of the gradient field, the spectral peak broadens considerably, forming a one-dimensional projection of the object (Fig. 9-14). By rotating the object and obtaining a set of projections, users can infer the 2D structure of the object and create an image via backprojection. Further, if the gradient strength is provided to the user (Hz/cm), then by comparing the spectral

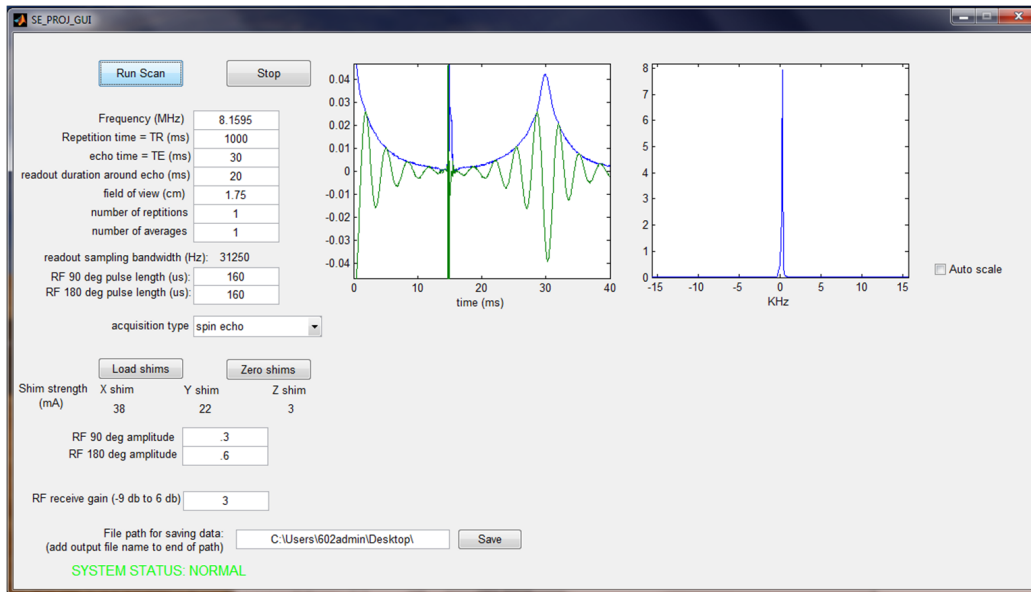


Figure 9-13: Spin echo GUI showing the FID leading up to the refocusing pulse as well as the spin echo following the pulse. The spectral line (right) is narrow for the well-shimmed sample shown.

width of the projection to the receiver sampling bandwidth, the user can calculate the width of the object in millimeters.

The spin echo GUI in projection mode is used for a popular lab exercise in which the student is given a “mystery phantom” that contains an unknown arrangement of 2 mm water filled capillary tubes. The student turns on one of the gradient fields, and physically rotates the sample inside the RF coil while viewing the projections. Similar to the original Lauterbur MRI experiment [1], the projections are then used to deduce the capillary arrangement.

Building on the concept of projection imaging, users then progress to imaging in 2D and 3D using spin echo pulse sequences. The sequence can be played in either single-echo mode (one acquired readout per TR) or in RARE echo train mode (Fig. 9-15). In the echo train, the readout gradient is repeatedly refocused by the 180° RF pulses. After each RF pulse, the amplitude of the in-plane phase encoding gradient is incremented, spanning the desired k-space region by the end of the train. After each readout, the phase encoding gradient is refocused to prevent errors in the magnetization history from accumulating during the echo train.

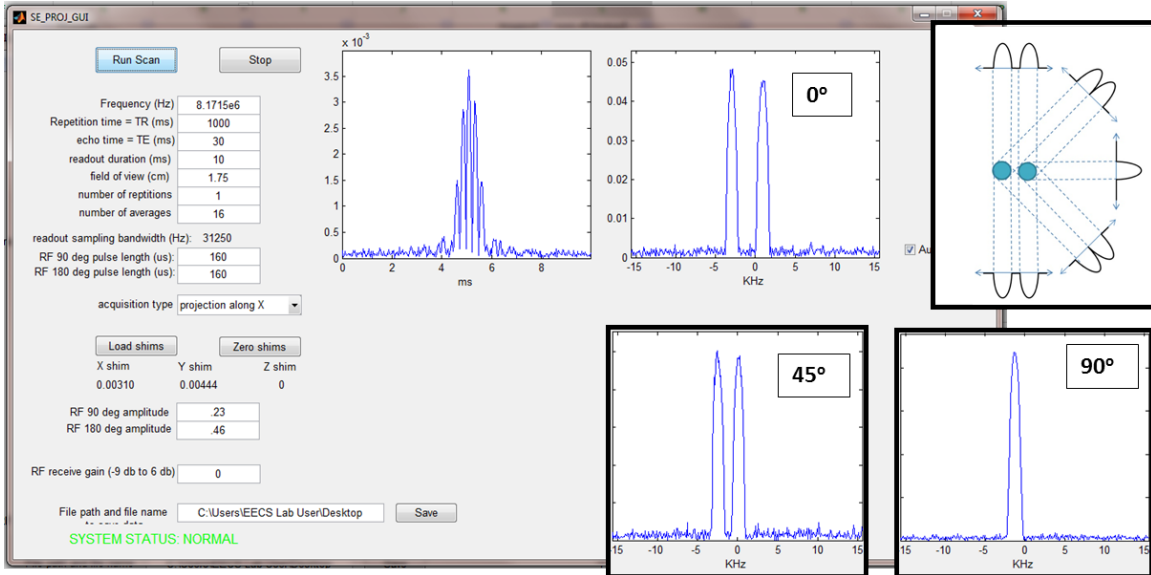


Figure 9-14: The spin echo GUI can be used in projection imaging mode to explore the structure of an object. Projections are shown of a rotated 2 tube phantom with the x-gradient on. A cartoon of projection reconstruction is also shown.

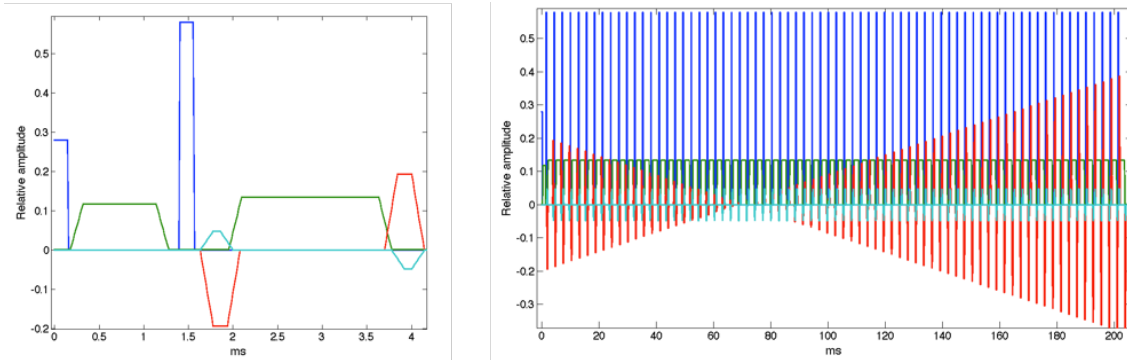


Figure 9-15: 3D spin echo pulse sequence shown for a single TR (left) and the full RARE echo train (72 readouts). RF pulses are shown in blue, readout gradient lobes in green, in-plane phase encoding lobes in red, and slice phase encoding lobes in cyan.

The imaging GUI shown in Figure 9-16 allows users to set the FOV, number of slices, number of averages, and the TR. Raw k-space data are displayed in real time. In echo train mode, an entire 2D k-space matrix is acquired during every TR, permitting very efficient imaging. For 3D datasets, the amplitude of the slice phase encode gradient is incremented in between TRs. After the entire acquisition is finished, Fourier transformed images are displayed. A representative 2D image as well as two 3D images are shown in Figure 9-17 along with acquisition parameters.

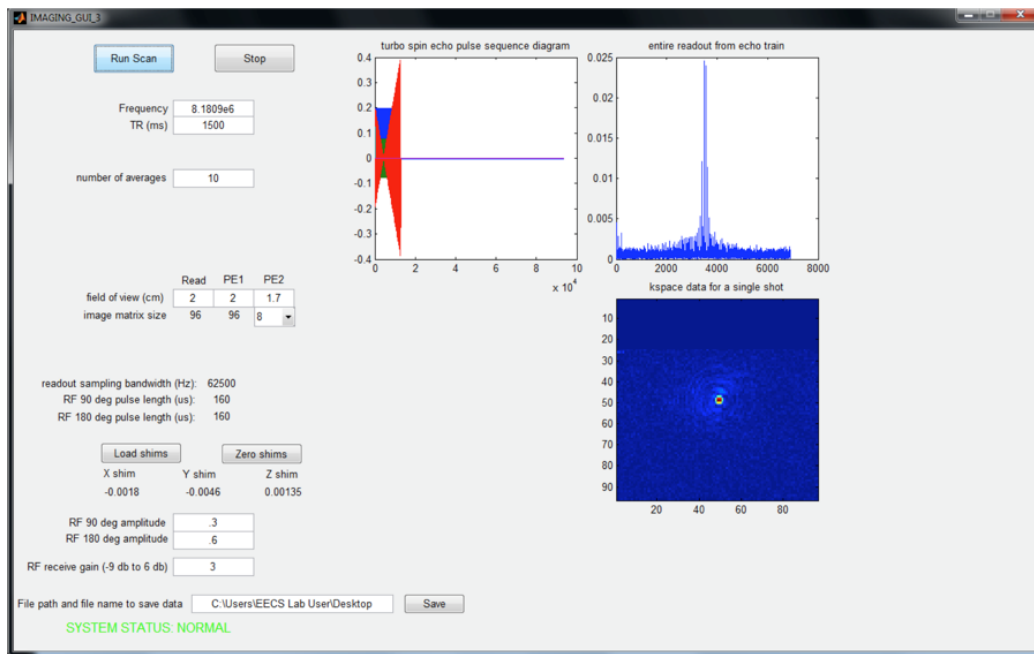


Figure 9-16: The imaging GUI allows users to choose the FOV along all three dimensions as well as the number of slices. Raw k-space data from each acquired echo train are displayed in real time.

## 9.7 Alternative Magnet Design

A dipolar Halbach magnet design was also considered for the system. The magnet array has a 6" diameter, and is composed of eight 8" x 1" x 1" N42 NdFeB magnet rungs. The simulated field is shown in Figure 9-18a. The simulated field had a homogeneity of 462 ppm in a 1 cm cube in the center. When the Z2 and X2-Y2 field components were removed from the field (which could theoretical be done with

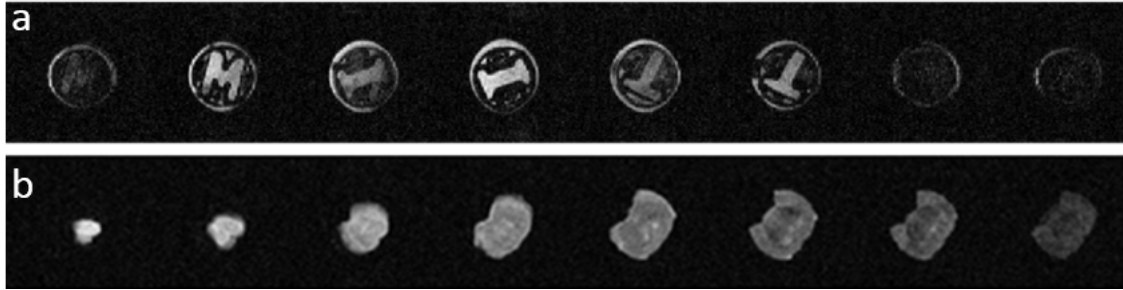


Figure 9-17: 3D images acquired with the instructional scanner are shown. In each case, a train of 72 echoes is zero-padded in the phase encode direction to form a 96 x 96 in-plane image matrix. (a) 3D-printed “M-I-T” phantom image (3D RARE sequence, FOV = 2 cm, image matrix = 96 x 96 x 9, 6/8 partial Fourier, BW = 62 kHz, NA=1). (b) Mouse brain (3D RARE sequence, FOV = 1.75 cm, image matrix = 96 x 96 x 9, 6/8 partial Fourier, BW = 62 kHz, NA=32).

shimming), a simulated homogeneity of 70 ppm was achieved.

The mechanical holder for the magnet rungs is a single polycarbonate 3D printed structure. The 8” magnet rungs are composed of two 4”x1”x1” bar magnets epoxied together. The constructed magnet is shown in Figure 9-18c. The resulting magnetic field in the center is 0.179 T (7.62 MHz Larmor frequency). This magnet was successfully tested in the scanner, but better performance was achieved with the CAS magnet described in section 9.2 due to higher  $B_0$  strength and homogeneity.

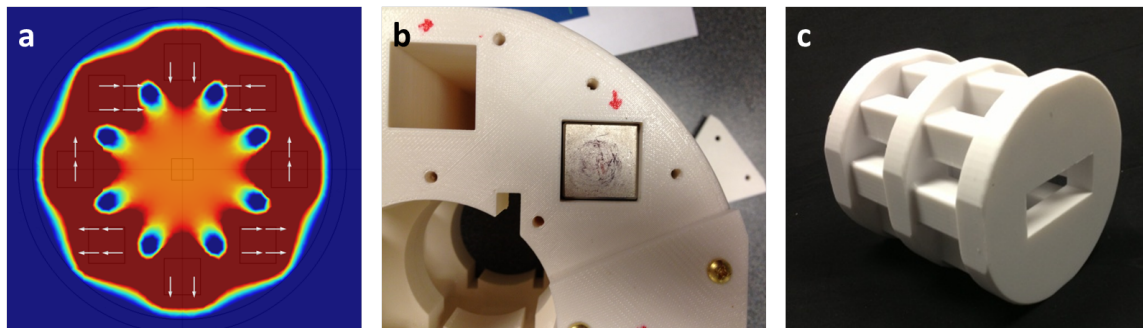


Figure 9-18: Simulated  $k = 2$  Halbach magnet with 6” diameter and eight 8x1x1” magnet rungs. (b) Magnet rung population (c) Constructed Halbach magnet for classroom MRI use.

# Bibliography

- [1] P. C. Lauterbur. Image formation by induced local interactions: Examples employing nuclear magnetic resonance. *Nature*, 242(5394):190–191, March 1973.
- [2] X Jiang, G Shen, Y Lai, and J Tian. Development of an open 0.3t NdFeB MRI magnet. *IEEE Trans. Appl. Supercond.*, 14(2):1621–1623, June 2004.
- [3] Fred A. Jr Mettler, Bruce R. Thomadsen, Mythreyi Bhargavan, Debbie B. Gilley, Joel E. Gray, Jill A. Lipoti, John McCrohan, Terry T. Yoshizumi, and Mahadevappa Mahesh. Medical radiation exposure in the u.s. in 2006: preliminary results. *Health Physics November 2008*, 95(5):502–507, 2008.
- [4] FA Mettler, W Huda, TT Yoshizumi, and M Mahesh. Effective doses in radiology and diagnostic nuclear medicine: a catalog. *Radiology*, 248(1):254–263, July 2008.
- [5] T Mashberg. CT scan to go. *MIT Technology Review*, December 2005.
- [6] A Park. Too many scans? use of CT scans triples, study finds. *Time*, June 2012.
- [7] DJ Brenner and H Hricak. Radiation exposure from medical imaging: Time to regulate? *JAMA*, 304(2):208–209, July 2010.
- [8] LS Medina, KE Applegate, and CC Blackmore. *Evidence-based imaging in pediatrics : optimizing imaging in pediatric patient care*. New York : Springer, c2010., 2010.
- [9] MS Pearce, JA Salotti, MP Little, K McHugh, C Lee, KP Kim, NL Howe, CM Ronckers, P Rajaraman, AW Craft, L Parker, and A Berrington de Gonzalez. Radiation exposure from CT scans in childhood and subsequent risk of leukaemia and brain tumours: a retrospective cohort study. *The Lancet*, 380(9840):499–505, August 2012.
- [10] FI Snell and MJ Halter. A signature wound of war: mild traumatic brain injury. *J Psychosoc Nurs Ment Health Serv*, 48(2):22–28, February 2010.
- [11] Karen A. Tong, Udochukwu E. Oyoyo, Barbara A. Holshouser, Stephen Ashwal, and L. Santiago Medina. Evidence-based neuroimaging for traumatic brain injury in children. In L. Santiago Medina, Kimberly E. Applegate, and

- C. Craig Blackmore, editors, *Evidence-Based Imaging in Pediatrics*, pages 85–102. Springer New York, January 2010.
- [12] B Lee and A Newberg. Neuroimaging in traumatic brain imaging. *NeuroRX*, 2(2):372–383, April 2005.
- [13] RG Gonzalez, WA Copen, PW Schaefer, MH Lev, SR Pomerantz, O Rapalino, JW Chen, GJ Hunter, JM Romero, BR Buchbinder, Mykol Larvie, Joshua Adam Hirsch, and Rajiv Gupta. The massachusetts general hospital acute stroke imaging algorithm: an experience and evidence based approach. *J NeuroIntervent Surg*, 5:7–12, May 2013.
- [14] Chris Zacko and Peter LeRoux. Perioperative neurosurgical critical care. In *Neurocritical Care Society Practice Update*, Philadelphia, PA, October 2013.
- [15] Clarissa Zimmerman, James Blau, Matthew S Rosen, and Lawrence L Wald. Design and construction of a halbach array magnet for portable brain MRI. in *Proc. of the ISMRM, Melbourne, Australia, 2012*, page 2575, 2012.
- [16] Clarissa Zimmerman Cooley, Jason P Stockmann, Brandon D Armstrong, Matthew S Rosen, and Lawrence L Wald. A lightweight, portable MRI brain scanner based on a rotating halbach magnet. in *Proc. of the ISMRM, Salt Lake City, USA, 2013*, page 137, 2013.
- [17] Clarissa Zimmerman Cooley, Jason P. Stockmann, Brandon D. Armstrong, Mathieu Sarracanie, Michael H. Lev, Matthew S. Rosen, and Lawrence L. Wald. Two-dimensional imaging in a lightweight portable MRI scanner without gradient coils. *Magn. Reson. Med.*, March 2014.
- [18] Clarissa Zimmerman Cooley, Jason P Stockmann, Brandon D Armstrong, Mathieu Sarracanie, Matthew S Rosen, and Lawrence L Wald. Spatial resolution in rotating spatial encoding magnetic field MRI (rSEM-MRI). in *Proc. of the ISMRM, Milan, 2014*, page 0033, 2014.
- [19] Ralf Kartäusch, Toni Driessle, Thomas Kampf, Thomas Christian Basse-Lüsebrink, Uvo Christoph Hoelscher, Peter Michael Jakob, Florian Fidler, and Xavier Helluy. Spatial phase encoding exploiting the bloch-siegert shift effect. *Magn. Reson. Mater. Phy.*, pages 1–9, November 2013.
- [20] Jonathan C Sharp and Scott B King. MRI using radiofrequency magnetic field phase gradients. *Magn. Reson. Med.*, 63(1):151–161, 2010.
- [21] Clarissa Zimmerman Cooley, Jason P Stockmann, Cris LaPierre, Thomas Witzel, Jia Feng, Maxim Zaitsev, Pascal Stang, Greig Scott, Yang Wenhui, Wang Zheng, and Lawrence L Wald. Implementation of low-cost, instructional tabletop MRI scanners. in *Proc. of the ISMRM, Milan, IT, 2014*, page 4819, 2014.

- [22] Donald B. Twieg. The k-trajectory formulation of the NMR imaging process with applications in analysis and synthesis of imaging methods. *Medical Physics*, 10(5):610–621, September 1983.
- [23] Jasper A Jackson, Lowell J Burnett, and J.Frank Harmon. Remote (inside-out) NMR. III. detection of nuclear magnetic resonance in a remotely produced region of homogeneous magnetic field. *J. Magn. Reson.*, 41:411–421, 1980.
- [24] M. Sagawa, S. Fujimura, N. Togawa, H. Yamamoto, and Y. Matsuura. New material for permanent magnets on a base of nd and fe (invited). *J. Appl. Phys.*, 55:2083–2087, 1984.
- [25] R.L Kleinberg, A Sezginer, D.D Griffin, and M Fukuhara. Novel NMR apparatus for investigating an external sample. *J. Magn. Reson.*, 97(3):466–485, 1992.
- [26] Federico Casanova, Juan Perlo, and Bernhard Blümich. *Single-Sided NMR*. Springer, January 2011.
- [27] R. Savelsberg G. Eidmann. The NMR MOUSE, a mobile universal surface explorer. *J Magn Reson Series A*, 122:104–109, 1996.
- [28] M Todica, R Fechete, and B Blümich. Selective NMR excitation in strongly inhomogeneous magnetic fields. *J. Magn. Reson.*, 164(2):220–227, 2003.
- [29] J Perlo, F Casanova, and B Blümich. 3D imaging with a single-sided sensor: an open tomograph. *J. Magn. Reson.*, 166(2):228–235, 2004.
- [30] Maxime Van Landeghem, Ernesto Danieli, Juan Perlo, Bernhard Blümich, and Federico Casanova. Low-gradient single-sided NMR sensor for one-shot profiling of human skin. *J. Magn. Reson.*, 215:74–84, 2012.
- [31] Katsumi Kose and Tomoyuki Haishi. High resolution NMR imaging using a high field yokeless permanent magnet. *Magn. Reson. Med. Sci.*, 10:159–167, 2011.
- [32] Takeshi Kimura, Yuto Geya, Yasuhiko Terada, Katsumi Kose, Tomoyuki Haishi, Hiroshi Gemma, and Yoshihiko Sekozawa. Development of a mobile magnetic resonance imaging system for outdoor tree measurements. *Rev Sci Instrum*, 82:053704, 2011.
- [33] Christian Senft, Volker Seifert, Elvis Hermann, Kea Franz, and Thomas Gasser. Usefulness of intraoperative ultra low-field magnetic resonance imaging in glioma surgery. *Neurosurgery*, 63:257–267, October 2008.
- [34] Christopher Nimsky, Atsushi Fujita, Oliver Ganslandt, Boris von Keller, and Rudolf Fahlbusch. Volumetric assessment of glioma removal by intraoperative high-field magnetic resonance imaging. *Neurosurgery*, 55(2):358–371, August 2004.

- [35] Medtronic for healthcare professionals: PoleStar surgical MRI system (website), August 2014.
- [36] Stanley B. Cohen, Hollis Potter, Atul Deodhar, Paul Emery, Philip Conaghan, and Mikkel Ostergaard. Extremity magnetic resonance imaging in rheumatoid arthritis: Updated literature review. *Arthritis Care Res*, 63(5):660–665, May 2011.
- [37] Takeshi Suzuki, Satoshi Ito, Shinya Handa, Katsumi Kose, Yoshikazu Okamoto, Manabu Minami, Makoto Sugihara, Masanobu Horikoshi, Hiroto Tsuboi, Taichi Hayashi, Daisuke Goto, Isao Matsumoto, and Takayuki Sumida. New low-field extremity MRI, compactScan: comparison with whole-body 1.5T conventional MRI. *Modern Rheumatology / The Japan Rheumatism Association*, 20(4):331–336, August 2010.
- [38] GE Healthcare: Optima MR430s 1.5T (website), August 2014.
- [39] Z H Cho, S T Chung, J Y Chung, S H Park, J S Kim, C H Moon, and I K Hong. A new silent magnetic resonance imaging using a rotating DC gradient. *Magn. Reson. Med.*, 39(2):317–321, 1998.
- [40] Kelvin J. Layton, Daniel Gallichan, Frederik Testud, Chris A. Cocosco, Anna M. Welz, Christoph Barmet, Klaas P. Pruessmann, Jürgen Hennig, and Maxim Zaitsev. Single shot trajectory design for region-specific imaging using linear and nonlinear magnetic encoding fields. *Magn. Reson. Med.*, October 2012.
- [41] Jürgen Hennig, Anna Masako Welz, Gerrit Schultz, Jan Korvink, Zhenyu Liu, Oliver Speck, and Maxim Zaitsev. Parallel imaging in non-bijective, curvilinear magnetic field gradients: a concept study. *Magn. Reson. Mater. Phy.*, 21(1-2):5–14, 2008.
- [42] Jason P Stockmann, Gigi Galiana, Leo Tam, Christoph Juchem, Terence W Nixon, and R Todd Constable. In vivo o-space imaging with a dedicated 12 cm Z2 insert coil on a human 3T scanner using phase map calibration. *Magn. Reson. Med.*, 69(2):444–455, 2013.
- [43] Jonathan C. Sharp, Scott B. King, Qunli Deng, Vyacheslav Volotovskyy, and Boguslaw Tomanek. High-resolution MRI encoding using radiofrequency phase gradients. *NMR Biomed.*, 26(11):1602–1607, November 2013.
- [44] CS Windt, H Soltner, D van Dusschoten, and P Blumler. A portable halbach magnet that can be opened and closed without force: The NMR-CUFF. *J. Magn. Reson.*, 208(1):27–33, January 2011.
- [45] Bernhard Blümich. The incredible shrinking scanner. *Scientific American*, 299(5):92–98, 2008.

- [46] Peter Campbell. *Permanent magnet materials and their application*. Cambridge University Press, Cambridge [England] ; New York, 1994.
- [47] T. Miyamoto, H. Sakurai, H. Takabayashi, and M. Aoki. A development of a permanent magnet assembly for MRI devices using Nd-Fe-B material. *IEEE Trans. Magn.*, 25(5):3907–3909, September 1989.
- [48] Robert Turner. Gradient coil design: A review of methods. *Magn. Reson. Imaging*, 11(7):903–920, 1993.
- [49] Manlio G. Abele. *Structures of Permanent Magnets*. Wiley, October 1993.
- [50] S.M. Wright, M.P. McDougall, and J.C. Bosshard. A desktop imaging system for teaching MR engineering. In *Proc. IEEE EMBC, 2010*, pages 6653–6656, August 2010.
- [51] Pure devices: Magnetic resonance in science GmbH (website), 2013.
- [52] Jordan Kirsch and Robert Newman. MIT junior lab - pulsed NMR lab manual, 2012.
- [53] Markus Billeter, Alan Sahakian, Bugrahan Yalvac, and Grace Nijm. A laboratory demonstration of spatial encoding in MRI. In *Proceedings of the 2006 American Society for Engineering Education Annual Conference & Exposition*.
- [54] Steven M. Wright, David G. Brown, Jay R. Porter, David C. Spence, Emilio Esparza, David C. Cole, and F. Russell Huson. A desktop magnetic resonance imaging system. *Magn. Reson. Mater. Phys.*, 13(3):177–185, October 2001.
- [55] Emilio Esparza-Coss and David M. Cole. A low cost MRI permanent magnet prototype. In *AIP Conference Proceedings*, volume 440, pages 119–129. AIP Publishing, August 1998.
- [56] J.C. Mallinson. One-sided fluxes - a magnetic curiosity? *IEEE Trans. Magn.*, 9(4):678–682, December 1973.
- [57] K. Halbach. Design of permanent multipole magnets with oriented rare earth cobalt material. *Nuclear Instrum. Methods*, 169(1):1–10, 1980.
- [58] Klaus Halbach. Physical and optical properties of rare earth cobalt magnets. *Nucl. Instrum. Methods.*, 187(1):109–117, August 1981.
- [59] Klaus Halbach. Application of permanent magnets in accelerators and electron storage rings (invited). *J. Appl. Phys.*, 57(8):3605–3608, April 1985.
- [60] H. A. Leupold, E. Potenziani Ii, and M. G. Abele. Applications of yokeless flux confinement. *J. Appl. Phys.*, 64(10):5994–5996, November 1988.
- [61] F. Bertora, A. Trequattrini, M. G. Abele, and P. Pan. Experimental evaluation of a yokeless permanent magnet. *J. Appl. Phys.*, 67(9):5950–5952, May 1990.

- [62] Tohru Shirai, Tomoyuki Haishi, Shin Utsuzawa, Yoshimasa Matsuda, and Katsumi Kose. Development of a compact mouse MRI using a yokeless permanent magnet. *Magn. Reson. Med. Sci.*, 4(3):137–143, 2005.
- [63] V. N. Samofalov, D. P. Belozorov, and A. G. Ravlik. Optimization of systems of permanent magnets. *Phys. Metals Metallogr.*, 102(5):494–505, November 2006.
- [64] Chun Li and M. Devine. Efficiency of permanent magnet assemblies for MRI devices. *IEEE Trans. Magn.*, 41(10):3835–3837, October 2005.
- [65] M. Kumada, E.I Antokhin, Y. Iwashita, M. Aoki, and E. Sugiyama. Super strong permanent dipole magnet. *IEEE Trans. App. Supercon.*, 14(2):1287–1289, June 2004.
- [66] Eiichi Fukushima. Radiofrequency coils for NMR: A peripatetic history of their twists and turns. In *eMagRes*. John Wiley & Sons, Ltd, 2007.
- [67] Giorgio Moresi and Richard Magin. Miniature permanent magnet for table-top NMR. *Concepts Magn. Reson.*, 19B(1):35–43, January 2003.
- [68] Ernesto Danieli, Jörg Mauler, Juan Perlo, Bernhard Blümich, and Federico Casanova. Mobile sensor for high resolution NMR spectroscopy and imaging. *J. Magn. Reson.*, 198(1):80–87, May 2009.
- [69] B. P. Hills, K. M. Wright, and D. G. Gillies. A low-field, low-cost halbach magnet array for open-access NMR. *J. Magn. Reson.*, 175(2):336–339, August 2005.
- [70] H. Raich and P. Blümli. Design and construction of a dipolar halbach array with a homogeneous field from identical bar magnets: NMR mandhalas. *Concept Magn. Reson. Part B*, 23B(1):16–25, 2004.
- [71] H. Soltner and P. Blümli. Dipolar halbach magnet stacks made from identically shaped permanent magnets for magnetic resonance. *Concepts Magn. Reson.*, 36A(4):211–222, July 2010.
- [72] Bo Zhang and G.P. Hatch. Field analysis and comparison of several permanent magnet dipole structures. *IEEE Trans. Magn.*, 45(10):4395–4398, October 2009.
- [73] P. Wroblewski, J. Szyszko, and W.T. Smolik. Mandhala magnet for ultra low-field MRI. In *Proc. IEEE IST, 2011*, pages 248–252, 2011.
- [74] J.E. Lenz. A review of magnetic sensors. *Proceedings of the IEEE*, 78(6):973–989, June 1990.
- [75] Nicola De Zanche, Christoph Barmet, Jurek A Nordmeyer-Massner, and Klaas P Pruessmann. NMR probes for measuring magnetic fields and field dynamics in MR systems. *Magn. Reson. Med.*, 60(1):176–186, 2008.

- [76] Christoph Barmet, Nicola De Zanche, and Klaas P. Pruessmann. Spatiotemporal magnetic field monitoring for MR. *Magn. Reson. Med.*, 60(1):187–197, July 2008.
- [77] M. Sagawa, S. Fujimura, H. Yamamoto, Y. Matsuura, and K. Hiraga. Permanent magnet materials based on the rare earth-iron-boron tetragonal compounds. *IEEE Trans. Magn.*, 20(5):1584–1589, September 1984.
- [78] Gerrit Schultz, Daniel Gallichan, Marco Reisert, Jürgen Hennig, and Maxim Zaitsev. MR image reconstruction from generalized projections. *Magn. Reson. Med.*, 2013.
- [79] Mark A. Brown and Richard C. Semelka. *MRI: Basic Principles and Applications*. Wiley, May 1999.
- [80] Robert L. Kleinberg and Jasper A. Jackson. An introduction to the history of NMR well logging. *Concepts Magn. Reson.*, 13(6):340–342, January 2001.
- [81] Bernhard Blümich, Federico Casanova, and Stephan Appelt. NMR at low magnetic fields. *Chemical Physics Letters*, 477(4-6):231–240, August 2009.
- [82] Chapter 14 - basic pulse sequences. In Matt A. Bernstein, Kevin F. King, and Xiaohong Joe Zhou, editors, *Handbook of MRI Pulse Sequences*, pages 579–647. Academic Press, Burlington, 2004.
- [83] Troy W. Borneman, Martin D. Hürlimann, and David G. Cory. Application of optimal control to CPMG refocusing pulse design. *J. Magn. Reson.*, 207(2):220–233, December 2010.
- [84] Malcolm H. Levitt. Composite pulses. In *eMagRes*. John Wiley & Sons, Ltd, 2007.
- [85] Van D. M. Koroleva, Soumyajit Mandal, Yi-Qiao Song, and Martin D. Hürlimann. Broadband CPMG sequence with short composite refocusing pulses. *J. Magn. Reson.*, 230:64–75, May 2013.
- [86] Dietmar Kunz. Frequency-modulated radiofrequency pulses in spin-echo and stimulated-echo experiments. *Magn. Reson. Med.*, 4(2):129–136, February 1987.
- [87] Jang-Yeon Park and Michael Garwood. Spin-echo MRI using  $\pi/2$  and  $\pi$  hyperbolic secant pulses. *Magn. Reson. Med.*, 61(1):175–187, January 2009.
- [88] Leah B. Casabianca, Daniel Mohr, Soumyajit Mandal, Yi-Qiao Song, and Lucio Frydman. Chirped CPMG for well-logging NMR applications. *J. Magn. Reson.*, 242:197–202, May 2014.
- [89] Klaas P. Pruessmann, Markus Weiger, Markus B. Scheidegger, and Peter Boesiger. SENSE: Sensitivity encoding for fast MRI. *Magn. Reson. Med.*, 42(5):952–962, November 1999.

- [90] Mark A. Griswold, Peter M. Jakob, Robin M. Heidemann, Mathias Nittka, Vladimir Jellus, Jianmin Wang, Berthold Kiefer, and Axel Haase. Generalized autocalibrating partially parallel acquisitions (GRAPPA). *Magn. Reson. Med.*, 47(6):1202–1210, June 2002.
- [91] Anagha Deshmane, Vikas Gulani, Mark A. Griswold, and Nicole Seiberlich. Parallel MR imaging. *J Magn Reson Imaging*, 36(1):55–72, July 2012.
- [92] Gerrit Schultz, Peter Ullmann, Heinrich Lehr, Anna M. Welz, Jürgen Hennig, and Maxim Zaitsev. Reconstruction of MRI data encoded with arbitrarily shaped, curvilinear, nonbijective magnetic fields. *Magn. Reson. Med.*, 64(5):1390 – 1403, 2010.
- [93] Gerrit Schultz, Hans Weber, Daniel Gallichan, Walter R T Witschey, Anna M Welz, Chris A Cocosco, Jürgen Hennig, and Maxim Zaitsev. Radial imaging with multipolar magnetic encoding fields. *IEEE Trans. Med. Imaging*, 30(12):2134–2145, 2011.
- [94] Daniel Gallichan, Chris A Cocosco, Andrew Dewdney, Gerrit Schultz, Anna Welz, Jürgen Hennig, and Maxim Zaitsev. Simultaneously driven linear and nonlinear spatial encoding fields in MRI. *Magn. Reson. Med.*, 65(3):702–714, March 2011.
- [95] Jason P Stockmann, Pelin Aksit Ciris, Gigi Galiana, Leo Tam, and R Todd Constable. O-space imaging: Highly efficient parallel imaging using second-order nonlinear fields as encoding gradients with no phase encoding. *Magn. Reson. Med.*, 64(2):447–456, 2010.
- [96] P. B. Roemer, W. A. Edelstein, C. E. Hayes, S. P. Souza, and O. M. Mueller. The NMR phased array. *Magn. Reson. Med.*, 16(2):192–225, 1990.
- [97] G C Wiggins, C Triantafyllou, A Potthast, A Reykowski, M Nittka, and L L Wald. 32-channel 3 tesla receive-only phased-array head coil with soccer-ball element geometry. *Magn. Reson. Med.*, 56(1):216–223, July 2006.
- [98] Eiichi Fukushima and Stephen B. W. Roeder. *Experimental Pulse NMR: A Nuts and Bolts Approach*. Westview Press, January 1993.
- [99] Boris Keil and Lawrence L. Wald. Massively parallel MRI detector arrays. *J. Magn. Reson.*, 229:75–89, April 2013.
- [100] Adnan Trakic, Ewald Weber, Bing Keong Li, Hua Wang, Feng Liu, Craig Engstrom, and Stuart Crozier. Electromechanical design and construction of a rotating radio-frequency coil system for applications in magnetic resonance. *IEEE Trans. Biomed. Eng.*, 59(4):1068–1075, April 2012.
- [101] Mingyan Li, Jin Jin, A. Trakic, Feng Liu, E. Weber, Yu Li, and S. Crozier. High acceleration with a rotating radiofrequency coil array (RRFCA) in parallel

- magnetic resonance imaging (MRI). In *Proc. IEEE EMBC, 2012*, pages 1098–1101, 2012.
- [102] Adnan Trakic, Ewald Weber, Mingyan Li, Jin Jin, Feng Liu, and Stuart Crozier. B1 gradient encoding with the rotating RF coil. in *Proc. of the ISMRM, Salt Lake City, USA, 2013*, page 3701, 2013.
- [103] Michael A. Ohliger and Daniel K. Sodickson. An introduction to coil array design for parallel MRI. *NMR Biomed*, 19(3):300–315, May 2006.
- [104] W.A Edelman, C.J Hardy, and O.M Mueller. Electronic decoupling of surface-coil receivers for NMR imaging and spectroscopy. *J. Magn. Reson.*, 67(1):156–161, 1986.
- [105] Gerrit Schultz. *Magnetic resonance imaging with nonlinear gradient fields: signal encoding and image reconstruction*. Wiesbaden : Springer Spektrum, c2013., 2013.
- [106] Magnus Hestenes and Eduard Stiefel. Methods of conjugate gradients for solving linear systems. *Journal of Research of the National Bureau of Standards*, 49(6):409–436, 1952.
- [107] R Gordon, R Bender, and G T Herman. Algebraic reconstruction techniques (ART) for three-dimensional electron microscopy and x-ray photography. *J. Theor. Biol.*, 29(3):471–481, 1970.
- [108] Klaas P. Pruessmann, Markus Weiger, Peter Börnert, and Peter Boesiger. Advances in sensitivity encoding with arbitrary k-space trajectories. *Magn. Reson. Med.*, 46(4):638–651, October 2001.
- [109] B.P. Sutton, D.C. Noll, and J.A Fessler. Fast, iterative image reconstruction for MRI in the presence of field inhomogeneities. *IEEE Trans. Med. Imaging*, 22(2):178–188, February 2003.
- [110] Kai Tobias Block, Martin Uecker, and Jens Frahm. Undersampled radial MRI with multiple coils. iterative image reconstruction using a total variation constraint. *Magn. Reson. Med.*, 57(6):1086–1098, 2007.
- [111] Jorge Nocedal and Stephen J. Wright. *Numerical optimization*. Springer series in operations research and financial engineering. New York : Springer, c2006., 2006.
- [112] Florian Knoll, Gerrit Schultz, Kristian Bredies, Daniel Gallichan, Maxim Zaitsev, Jürgen Hennig, and Rudolf Stollberger. Reconstruction of undersampled radial PatLoc imaging using total generalized variation. *Magn. Reson. Med.*, 70(1):40–52, 2013.

- [113] S Kaczmarz. Angenäherte auflösung von systemen linearer gleichungen. *Bulletin International de l'Academie Polonaise des Sciences et des Lettres*, 35:355–357, 1937.
- [114] Jason P Stockmann and R Todd Constable. Kaczmarz iterative reconstruction for arbitrary hybrid encoding functions. *in Proc. of the ISMRM, Honolulu, HI, 2009*, page 2857, 2009.
- [115] Yair Censor. Sequential and parallel projection algorithms for feasibility and optimization. In *Proc. SPIE, 2001*, volume 4553, pages 1–9, 2001.
- [116] E Danieli, J Perlo, B Blümich, and F Casanova. Highly stable and finely tuned magnetic fields generated by permanent magnet assemblies. *Phys. Rev. Lett.*, 110(18):180801, 2013.
- [117] Donald W. McRobbie, Elizabeth A. Moore, Martin J. Graves, and Martin R. Prince. *MRI from Picture to Proton*. Cambridge University Press, September 2006.
- [118] Daniel Gallichan, Chris A Cocosco, Gerrit Schultz, Hans Weber, Anna M Welz, Jürgen Hennig, and Maxim Zaitsev. Practical considerations for in vivo MRI with higher dimensional spatial encoding. *Magn. Reson. Mater. Phys.*, 25(6):419–431, December 2012.
- [119] F. Bloch and A. Siegert. Magnetic resonance for nonrotating fields. *Phys. Rev.*, 57(6):522–527, March 1940.
- [120] Norman F. Ramsey. Resonance transitions induced by perturbations at two or more different frequencies. *Phys. Rev.*, 100(4):1191–1194, November 1955.
- [121] Laura I. Sacolick, Florian Wiesinger, Ileana Hancu, and Mika W. Vogel. B1 mapping by bloch-siegert shift. *Magn. Reson. Med.*, 63(5):1315–1322, May 2010.
- [122] Scott B King, D Yin, S Thingvold, Jonathan C Sharp, and Boguslaw Tomanek. Transmit array spatial encoding (TRASE): A new data acquisition method in MRI. *in Proc. of the ISMRM, Seattle, Washington, USA, 2006*, page 2628, 2006.
- [123] Scott B King, P Latta, Vyacheslav Volotovskyy, Jonathan C Sharp, and Boguslaw Tomanek. Phase encoding without gradients using TRASE-FSE MRI. *in Proc. of the ISMRM, Berlin, Germany, 2005*, page 680, 2007.
- [124] Qunli Deng, Scott B. King, Vyacheslav Volotovskyy, Boguslaw Tomanek, and Jonathan C. Sharp. B1 transmit phase gradient coil for single-axis TRASE RF encoding. *Magn. Reson. Imaging*, 31(6):891–899, July 2013.

- [125] Henny M. Borsboom, Tatjana Claasen-Vujcic, Harry J. G. Gaykema, and Toon Mehlkopf. Low-frequency quadrature mode birdcage resonator. *Magn. Reson. Mater. Phy.*, 5(1):33–37, March 1997.
- [126] Zohaib Mahmood, Bastien Guerin, Boris Keil, Elfar Adalsteinsson, Lawrence L. Wald, and Luca Daniel. Design of a robust decoupling matrix for high field parallel transmit arrays. *in Proc. of the ISMRM, Milan, IT, 2014*, page 0033, 2014.
- [127] Pascal P Stang, Steven M Conolly, Juan M Santos, John M Pauly, and Greig C Scott. Medusa: a scalable MR console using USB. *IEEE Trans. Med. Imaging*, 31(2):370–379, February 2012.